

# Synthesis, Characterization and Catalysis of Nanostructured Vanadia Model Catalysts for Partial Oxidation of Propane

von

Rita Herbert

Dipl.-Ing. für Verfahrenstechnik

aus Berlin

der Fakultät II - Mathematik und Naturwissenschaften

der Technischen Universität Berlin

zur Erlangung des akademischen Grades

Doktor der Ingenieurwissenschaften

Dr.-Ing.

genehmigte Dissertation

Promotionsausschuss:

Vorsitzender: Prof. Lerch

Gutachter: Prof. Schlögl

Gutachter: Prof. Schomäcker

Tag der wissenschaftlichen Aussprache: 06.02.2009

Berlin 2009

D83



*Es ist keine Schande, nichts zu wissen, wohl aber, nichts lernen zu wollen.*

Sokrates (469-399 v.Chr.)



## Zusammenfassung

Nanostrukturierte Vanadiumoxidmodellkatalysatoren, geträgert auf Siliziumdioxid, wurden sowohl mit einem mehrstufigen Verfahren als auch mit herkömmlicher Imprägnierung (*incipient wetness impregnation*) synthetisiert, charakterisiert und in der oxidativen Dehydrierung von Propan getestet. Als Siliziumdioxidträgermaterial wurde zum einen mesoporöses SBA-15 und zum anderen Aerosil 300 eingesetzt. Das mehrstufige Syntheseverfahren beinhaltet eine Funktionalisierung der SiO<sub>2</sub>-Oberfläche und einen Ionenaustausch mit Decavanadationen. Ein Ziel war es die Unterschiede zwischen den beiden Trägermaterialien und den Synthesemethoden hinsichtlich der Vanadiumstruktur und dem katalytischen Verhaltens zu untersuchen und einen Zusammenhang herauszuarbeiten.

Um möglichst vergleichbare hochdisperse Vanadiumoxidspezies zu erhalten, wurde eine Vanadiumdichte von 0,7 V-atome/nm<sup>2</sup> eingestellt. Die Proben wurden mit Stickstoff-Adsorption-Desorption, Kleinwinkel XRD, TEM, XPS, Raman- und UV-vis Spektroskopie charakterisiert. Die Reaktivität wurde zusätzlich mit TPR untersucht.

Dabei konnte gezeigt werden, dass die mehrstufige Synthesemethode einen Stabilisierungseffekt auf das mesoporöse Material hat. Nach mechanischer, thermischer und hydrothermischer Belastung zeigte das Material nach der Oberflächenfunktionalisierung durch diese Methode eine höhere Stabilität als das reine SBA-15. Während das reine SBA-15 schon 75 MPa mechanischen Druckbehandlung einen deutlichen Rückgang der BET-Oberfläche aufweist, ändern sich die Proben, die mit dem mehrstufigen Verfahren hergestellt wurden, bis zu einem Druck von 376 MPa nur geringfügig. Nach einer mechanischen Druckbehandlung von 752 MPa lässt sich bei reinem SBA-15 keine mesoporöse Struktur mehr erkennen, bei den Proben des mehrstufigen Verfahrens sind dahingegen noch Strukturen sichtbar. Die imprägnierten Proben zeigen die gleichen Stabilitätseigenschaften wie das reine SBA-15. Diese erhöhte Stabilität hat einen positiven Einfluss auf die Testreaktion. Die mit 752 MPa gepresste mehrstufig hergestellte Probe zeigt in der ODH von Propan eine höhere Selektivität zu Propen, als die

---

imprägnierte Probe. Das ist auf die Erreichbarkeit der aktiven Zentren zurückzuführen, von denen in der imprägnierten Probe ein größerer Anteil nicht erreichbar ist.

Beim Vergleich der verschieden präparierten Proben auf den unterschiedlichen Trägermaterialien kann eine Erhöhung des Polymerisierungsgrades in folgender Reihenfolge beobachtet werden:  $V_xO_y/SBA-15$  mehrstufig  $\rightarrow V_xO_y/SBA-15$  imprägniert  $\rightarrow V_xO_y/A300$  mehrstufig  $\rightarrow V_xO_y/A300$  imprägniert. Dabei zeigen die spektroskopischen Daten einen deutlichen Einfluss der unterschiedlichen Trägermaterialien auf den Polymerisationsgrad, während die TPR Ergebnisse klare Unterschiede zwischen den Synthesemethoden aufweisen. Diese Unterschiede haben jedoch keinen signifikanten Einfluss in der oxidativen Dehydrierung (ODH) von Propan bzgl. der Selektivitäten (bei gleichen Umsätzen). Das führt zu der Annahme, dass die Zusammensetzung der Gasphase einen starken Einfluss auf die Reaktivität des Vanadiumoxids hat.

Ein weiteres Thema dieser Arbeit waren erste Untersuchungen zu einem SBA-15 - Titansystem, das als Trägermaterial für Vanadiumoxid dienen kann. Dafür wurden verschiedene Beladungen von Titanoxid auf SBA-15 aufgebracht und charakterisiert. Zusätzlich wurde eine Probe Ti/SBA-15 mit Vanadium hergestellt, spektroskopisch untersucht und in der oxidativen Dehydrierung von Propan getestet. Die Ergebnisse hier zeigen bezüglich Umsatz und Selektivität ein ähnliches Verhalten wie Vanadium auf reinem SBA-15 bei 450 °C aber ein deutlich anderes Verhalten bei 500 °C. Bei der V-Ti/SBA-15 Probe ist bei einer Reaktionstemperatur von 500 °C ein deutlicher Anstieg des Propanumsatzes zu beobachten.

## Abstract

Nanostructured vanadia model catalysts supported by silica were synthesized in a multi-step procedure as well as through incipient wetness impregnation. Afterwards, the samples were characterized and tested in the oxidative dehydrogenation (ODH) of propane. Silica supports used were mesoporous SBA-15 and Aerosil 300. The multi-step synthesis includes a surface functionalization and an ion exchange with decavanadate ions. One aim of this study was the investigation of the influence between two support materials and between different synthesis method concerning the vanadia structure and to find a correlation to their catalytic behavior.

Therefore, highly dispersed vanadia species with a similar vanadium density of 0.7 V atoms/nm<sup>2</sup> were prepared. The samples were thoroughly characterized by nitrogen adsorption-desorption, small-angle XRD, TEM, XPS, Raman- and UV-vis spectroscopy. Furthermore, reactivity was tested with TPR besides catalytic test.

It could be shown that the multi-step procedure has a stabilizing effect on the mesoporous material. After mechanical, thermal and hydrothermal treatment, the sample treated with surface functionalization shows a higher stability than blank SBA-15. The blank SBA-15 shows a significant decrease of the BET surface area already at a mechanical treatment already at 75 MPa, whereas a significant change of the surface area in the multi-step samples appears not until at 376 MPa. After pressure treatment at 752 MPa no mesoporous structure can be observed anymore for blank SBA-15, but for the multi-step sample it is in parts still observable. The impregnated samples show the same behavior as blank SBA-15. The enhanced stability has a positive influence on reaction behavior. The multi-step sample pressed at 752 MPa shows in the ODH of propane a higher selectivity towards propene than the impregnated sample treated in the same way. This can be explained by accessibility of active sites within the samples. In the impregnated sample are more active sites blocked than in the multi-step sample, due to the complete loss of mesoporous structure.

When comparing both support materials and the different synthesis methods, an in-

---

crease of the degree of polymerization can be observed in the following order:  $V_xO_y$ /SBA-15 multi-step  $\rightarrow V_xO_y$ /SBA-15 impregnated  $\rightarrow V_xO_y$ /A300 multi-step  $\rightarrow V_xO_y$ /A300 impregnated. It can be said that the spectroscopic data show a more distinct influence on the degree of polymerization of the support materials, whereas TPR data show clear differences among the synthesis methods. In the oxidative dehydrogenation of propane, no differences could be observed concerning the selectivities at similar conversions. This leads to the assumption that the reactivity is highly influence by the composition of the gas phase.

Another issue in this study was first investigations on an SBA-15/titanium system, which can be applied as a support material for vanadia. For this purpose, several loadings of titania were impregnated on SBA-15 and characterized. Additionally, a Ti/SBA-15 sample with vanadium was synthesized, spectroscopically characterized and tested in the oxidative dehydrogenation of propane. The results show for conversion and selectivity a similar behavior at a reaction temperature of 450 °C as vanadium on blank SBA-15, but clear differences at a reaction temperature of 500 °C. For V-Ti/SBA-15 at a reaction temperature of 500 °C a significant increase of conversion of propane can be observed.



# Contents

<b>1</b>	<b>Introduction and aim of study</b>	<b>1</b>
1.1	Vanadia in partial oxidation reactions . . . . .	2
1.2	Nanostructured materials as model catalysts . . . . .	4
1.2.1	Surface structure of amorphous silica . . . . .	5
1.2.2	Structure of supported vanadia . . . . .	7
1.3	Selective oxidation of propane . . . . .	11
<b>2</b>	<b>Experimental set-ups and basic principles</b>	<b>13</b>
2.1	Nitrogen adsorption-desorption . . . . .	13
2.1.1	BET surface area . . . . .	14
2.1.2	Pore size analysis . . . . .	16
2.2	X-ray diffraction . . . . .	20
2.3	X-ray photoelectron spectroscopy . . . . .	22
2.4	Electron microscopy . . . . .	26
2.4.1	Transmission electron microscopy . . . . .	27
2.4.2	Scanning electron microscopy . . . . .	28
2.5	UV-vis spectroscopy . . . . .	28
2.6	Raman spectroscopy . . . . .	30
2.7	Temperature programmed reduction and oxidation . . . . .	33
2.8	Catalytic tests . . . . .	34
<b>3</b>	<b>Synthesis of silica-supported vanadia catalysts</b>	<b>37</b>

3.1	Synthesis of SBA-15 . . . . .	37
3.2	Multi-step procedure with functionalization and ion exchange . . . . .	40
3.3	Incipient wetness impregnation . . . . .	42
<b>4</b>	<b>Characterization of silica-supported vanadia catalysts</b>	<b>45</b>
4.1	Physical characterization of silica supports . . . . .	45
4.1.1	SBA-15 . . . . .	45
4.1.2	Aerosil 300 . . . . .	50
4.2	Mechanical, thermal, and hydrothermal stability . . . . .	50
4.2.1	Mechanical stability . . . . .	51
4.2.2	Thermal stability . . . . .	60
4.2.3	Hydrothermal stability . . . . .	63
4.2.4	Conclusion . . . . .	65
4.3	Comparison of silica supports and synthesis methods . . . . .	65
4.3.1	Physical characterization . . . . .	66
4.3.2	Spectroscopic characterization . . . . .	68
4.3.3	Conclusion . . . . .	73
<b>5</b>	<b>Reactivity of silica-supported vanadia catalysts</b>	<b>75</b>
5.1	Catalytic tests after mechanical treatment . . . . .	75
5.2	Reactivity of different silica supports and synthesis methods . . . . .	77
5.2.1	Temperature programmed reduction and oxidation . . . . .	77
5.2.2	Catalytic tests . . . . .	81
5.2.3	Conclusion and outlook . . . . .	85
<b>6</b>	<b>Characterization and catalytic tests of V/Ti-supported SBA-15 catalysts</b>	<b>89</b>
6.1	Characterization of Ti-supported SBA-15 with different loadings . . . . .	90
6.2	Characterization and catalytic tests of V/Ti-supported SBA-15 . . . . .	95
<b>7</b>	<b>Conclusion and outlook</b>	<b>103</b>

<b>List of Figures</b>	<b>109</b>
<b>List of Tables</b>	<b>115</b>
<b>A Appendix</b>	<b>131</b>
A.1 Curriculum Vitae . . . . .	132
A.2 Publication . . . . .	133



## List of symbols

### Latin letters

$a$	[Å]	unit cell parameter
$A$	[m <sup>2</sup> ]	surface area
$A^{eff}$	[m <sup>2</sup> ]	effective area per molecule
$c$	[-]	concentration
$C$	[-]	constant
$d$	[m]	distance between two lattice planes
$E$	[J]	energy
$F$	[KMU]	Kubelka-Munk function
$h$	[eV s]	Planck constant (4.1357)
$l$	[-]	orbital momentum
$m$	[kg]	mass
$n$	[-]	order of reflection (integer)
$\dot{n}$	[mol/s]	flow rate of the amount of substance
$n^s$	[-]	quantity of absorbed gas
$p$	[Pa]	pressure
$p_0$	[Pa]	pressure of the adsorbate at adsorption temperature
$r$	[m]	radius
$r_k$	[Å]	Kelvin radius
$R$	[J/mol K]	universal gas constant (8.314472)
$\tilde{R}$	[%]	reflectance
$\mathfrak{R}$	[-]	constant
$s$	[-]	spin momentum
$S$	[-]	selectivity
$t$	[Å]	statistical thickness of the adsorbed film
$T$	[K]	temperature

## List of symbols

---

$V$	[m <sup>3</sup> ]	volume
$\bar{V}$	[m <sup>3</sup> /mol]	molar volume of the condensed liquid
$w$	[Å]	wall thickness
$X$	[-]	conversion

## Greek letters

$\gamma$	[N/m]	surface tension
$\lambda$	[m]	wavelength
$\nu$	[Hz]	frequency
$\Phi$	[J]	work function
$\Theta$	[°]	angle in Bragg's Law
$\tau$	[s]	residence time

## Indices

$B$	binding
$cl$	core level
$gas$	gas
$i$	reaction component
$K$	kinetic
$liq$	liquid
$m$	monolayer
$M$	molecule
$mod$	modified
$sample$	sample

<i>p</i>	pore
<i>ph</i>	photon
<i>ref</i>	reference
<i>vib</i>	vibration

**Abbreviation**

APTMS	3-aminopropyltrimethoxysilane
BET	method of determination of the specific surface area (Brunauer, Emmet, Teller)
BJH	method of determination of pore size distribution (Barrett, Joyner, Halenda)
CT	charge transfer
DFT	density functional theory
EDX	energy-dispersed X-ray spectroscopy
EO	ethylene oxide
Et	ethylene
FWHM	full width at half maximum
EXAFS	extended X-ray absorption fine structure
H <sup>+</sup> X <sup>-</sup>	acid media
I <sup>-</sup>	cationic inorganic solution
I <sup>+</sup>	anionic inorganic solution
IR	infrared
IUPAC	International Union of Pure Applied Chemistry
NEXAFS	near edge X-ray absorption fine structure
NLDFT	non local density functional theory
MCM	mobile composition of matter

*List of symbols*

---

ODH	oxidative dehydrogenation
PO	propylene oxide
R	organic moiety
S <sup>-</sup>	cationic Surfactant
S <sup>+</sup>	anionic Surfactant
SBA	Santa Barbara
SEM	scanning electron microscopy
TEOS	tetraethoxysilane
TEM	transmission electron microscopy
TPD	temperature programmed desorption
TPO	temperature programmed oxidation
TPR	temperature programmed reduction
UV	ultraviolet
vis	visible
XAFS	X-ray absorption fine structure
XPS	X-ray photoelectron spectroscopy
XRD	X-ray diffraction



# 1 Introduction and aim of study

The definition of catalyst is given by the IUPAC (International Union of Pure and Applied Chemistry)<sup>[72]</sup>: "A substance that increases the rate of a reaction without modifying the overall standard Gibbs energy change in the reaction; the process is called catalysis. The catalyst is both a reactant and product of the reaction. [...] Catalysis can be classified as homogeneous catalysis, in which only one phase is involved, and heterogeneous catalysis, in which the reaction occurs at or near an interface between phases. Catalysis brought about by one of the products of a reaction is called autocatalysis. Catalysis brought about by a group on a reactant molecule itself is called intramolecular catalysis."

The term catalysis was coined by Berzelius in 1836. Already in the early 1800s, scientists like Berzelius, Davy and Faraday searched for catalysts. The beginning of industrial catalyst technology was about 1875 with large-scale production of sulfuric acid on platinum catalysts. In the years 1935 and 1940, catalytic cracking was a significant development for petroleum industry, and in 1950, catalytic naphtha reforming led to dehydrogenation and isomerization processes.<sup>[10]</sup> In the following years research was going on. One of the main fields for catalyst investigation is the field of selective oxidation processes.

Understanding the catalytic processes on an atomic scale is still a matter of research. In 2007 the Nobel Prize for chemistry was awarded to Gerhard Ertl for his contribution to the understanding of chemical processes on solid surfaces. He and his coworkers answered the question how hydrogen is organized on metals like palladium, platinum and nickel and he clarified the molecular mechanism of the catalytic reaction in the

Haber-Bosch process.<sup>[101]</sup> This shows that the aim in catalytic research is to find a correlation between the catalytic performance and their chemical and physical properties such as molecule structure and oxidation state. Since these properties can change during the reaction, it is necessary to characterize the catalyst before and after it. A much better way seems to be *in situ* spectroscopy. This means spectroscopic investigation during the reaction.

One way to explore the structure of active catalysts is to use model systems. The subject of this study is an investigation of silica-supported vanadia model catalysts and their use for partial oxidation of propane. The following section gives a short introduction to vanadia in partial oxidation reaction, nanostructured materials as model catalysts, the surface structure of silica and vanadium, as well as some basics about the selective oxidation of propane. In the following chapters, the effects of synthesis methods and two different silica supports are described, as well as their catalytic results in the oxidative dehydrogenation (ODH) of propane. Furthermore, first results of a combination of titanium and vanadium supported by silica SBA-15 are reported.

## 1.1 Vanadia in partial oxidation reactions

Oxidation processes can be divided into two industrially used processes: partial oxidation and total oxidation. Partial oxidation is required if the desired product, mostly bulk organic materials, is not the most stable one with regard to thermodynamics. The products of partial or selective oxidation are essential in the production of a wide range of materials like artificial fibers and plastics. The products of total oxidation (for hydrocarbons, CO<sub>2</sub>, and water) are thermodynamically most stable. Total oxidation can be applied for energy conversion and pollution abatement.<sup>[49]</sup>

Vanadium is an essential element for multitude catalysts used for selective oxidation reactions. Table 1.1 shows some industrial processes bases on vanadium oxides. Research is going on for vanadium containing multicomponent bulk materials as well as for supported vanadia catalysts, especially for the partial oxidation of alkanes. The

Table 1.1: Selected industrial catalytic processes using vanadium oxides<sup>[100]</sup>

Industrial process	Catalyst material
Oxidation of SO <sub>2</sub> to SO <sub>3</sub> in the production of sulfuric acid	V <sub>2</sub> O <sub>5</sub>
Oxidation of benzene to maleic anhydride	V <sub>2</sub> O <sub>5</sub>
Oxidation of naphthalene to phthalic anhydride	V-Mo oxides
Oxidation of butene to phthalic anhydride	V-P oxides
Oxidation of o-xylene to phthalic anhydride	V-Ti oxides
Selective reduction of NO <sub>x</sub> with NH <sub>3</sub>	V <sub>2</sub> O <sub>5</sub> /WO <sub>3</sub> /TiO <sub>2</sub>

most well-known example of bulk catalysts are VPO catalysts used in the production of maleic anhydride from n-butane.<sup>[22]</sup> Further investigations were done for V-Mg-O, which are reported to be among the most active and selective catalysts in the oxidative dehydrogenation (ODH) of propane<sup>[24] [83] [34]</sup> and *n*-butane<sup>[57] [23]</sup>. Another class of bulk vanadium mixed oxides are MoVTeNb oxides, which display a high catalytic performance for the oxidation of propane to acrylic acid<sup>[63] [75]</sup>.

From the group of supported vanadia catalysts, alumina, silica, titania and zirconia are typically used as support materials. Recently, investigations with supported vanadia were done for partial oxidation of methane<sup>[12] [30]</sup>, methanol<sup>[17]</sup>, ethanol<sup>[59]</sup>, ethylbenzene<sup>[58]</sup> and ODH of propane<sup>[62] [25] [76] [64] [65]</sup>.

With regard to an extended investigation on the structure of vanadia on support materials and their correlation to catalytic activity, there are still elementary aspects which are not completely understood. Focusing on silica support materials, several suggestions for the vanadia structure can be seen in recent literature<sup>[70] [8] [42]</sup> (see Figure 1.4) and are still a matter of discussion.

## 1.2 Nanostructured materials as model catalysts

For understanding the role of active sites in catalysis models, catalysts which give access to the catalyst structure and dispersion and have full catalytic abilities are a desired tool.

Nanostructured materials fulfill these requirements. They can be defined as materials whose structural elements, meaning clusters, crystallites or molecules, have dimensions in the range of 1 to 100 nm. Following this definition mesoporous materials with pore sizes between 2 and 50 nm<sup>[66]</sup> belong to this class of materials. One of the characteristics of these materials is the high surface area that provides the space to create isolated active centers. Due to the increasing complexity of agglomerates in structure and consequently in spectroscopic analysis, isolated sites, not only meaning single-centered sites, but also multi-centered sites (such as oligomeric species) are essential for model catalysts. Another important point for supported model catalysts is the structural homogeneity of the support material. This allows to concentrate only on the active site, providing a nearly identical environment for anchoring to the support. Ordered mesoporous materials seem to be suited for support materials as model catalysts. The first synthesis of an ordered mesoporous material was described in a patent in 1969 but did not attract much attention. Not until 1992, when a group of scientists of Mobil discovered mesoporous silica MCM-41, -48, and -50 materials, the research for this kind of materials started.<sup>[92]</sup>

SBA-15<sup>1</sup>, another mesoporous silica material, was discovered in 1998. SBA-15 can be described as a molecular sieve with uniform hexagonal channels, a narrow pore size distribution and a high surface area (about 800 m<sup>2</sup>). The pore width is tunable in a range of 5 - 30 nm, depending on the synthesis routine. All these properties make it a preferable support material for model catalysts. Furthermore, the thickness of the amorphous framework walls (3.1-6.4 nm) provides considerable hydrothermal stability exceeding that of the thinner walled MCM-41 material.<sup>[20]</sup> In addition to that, we

---

<sup>1</sup>SBA - short for Santa Barbara, the place where it was developed

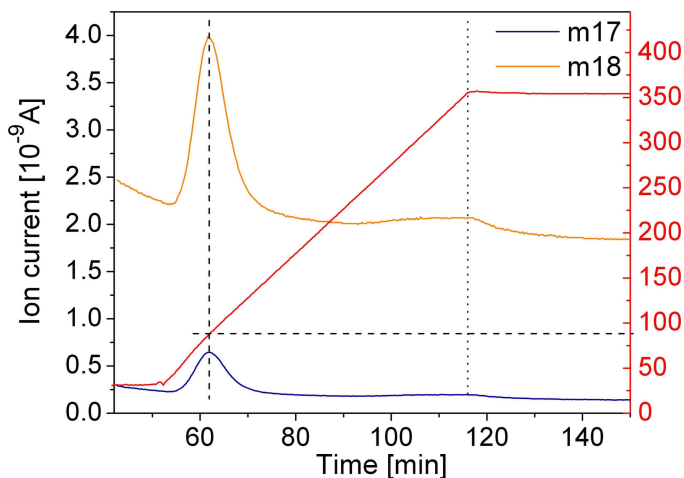


Figure 1.1: Dehydration process of silica SBA-15 observed by mass spectroscopy

discovered an increasing stability concerning mechanical, thermal and hydrothermal properties by a post-synthesis surface modification using alkoxysilanes.

Another advantage of the material is the great number of silanols on the pore walls of SBA-15, on which a large number of catalytic active centers can be incorporated.<sup>[67] [93] [2]</sup>

However, the role of the support in supported vanadia catalysts is still not completely clarified. In literature strong influences of the support material on catalytic performance have been reported.<sup>[75] [56]</sup> The origin of this behavior may either be attributed to intrinsic support properties or to differences in the vanadia structure(s) present on the different support materials, or even to a combination of both effects.

### 1.2.1 Surface structure of amorphous silica

The huge group of amorphous silica materials consists of an almost infinite variety of forms, ranging from dense, hard, impervious mineral opal to extremely light, porous synthetic products. Furthermore, it can be subdivided concerning the particle size, ranging from large, solid masses to submicroscopic particles, and additionally, concerning the degree of hydration, from almost anhydrous  $\text{SiO}_2$  to soft gelatinous masses containing 100 parts of water per part of silica.<sup>[52]</sup> In general, the surface of amorphous silica gel and powders consists of a layer of silanol groups ( $\text{SiOH}$ ), where water

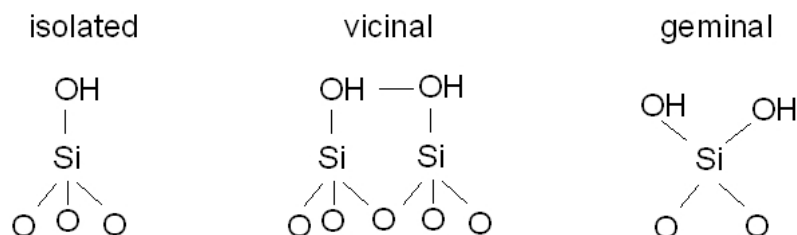


Figure 1.2: Scheme of several forms of silanol groups

is physically adsorbed to a degree which depends on the relative humidity. Most of the physically adsorbed water is removed by drying in air at 150 to 200 °C, leaving only the water which is chemically combined as silanol groups.<sup>[52]</sup> But the water in the very fine pores is held very tenaciously. Thermogravimetric measurements combined with mass spectroscopy for our SBA-15 showed two water peaks. The first one appears at 90 °C, and the second one at 350 °C (see Figure 1.1).

Silica particles can be regarded as polymers of silicic acid, consisting of interlinked  $\text{SiO}_4$  tetrahedra, which are surface terminated by either siloxane groups ( $\equiv \text{Si}-\text{O}-\text{Si} \equiv$ ) or by silanol groups ( $\equiv \text{Si}-\text{OH}$ ). There are different forms of silanol groups (isolated or free silanols, geminal silanols, vicinal or bridged silanols; see Figure 1.2). Especially with regard to the existence of geminal hydroxyl groups, there is an ongoing discussion in literature.<sup>[94]</sup> Since the surface structure of amorphous silica is highly disordered, one cannot expect a regular arrangement of hydroxyl groups; the surface may be covered with all three forms in different ratios.

Based on theoretical calculations and a variety of experimental data, the overall number of silanols can be considered as a physiochemical constant (fully hydroxylated: 4.6 OH/nm<sup>2</sup>; at 400 °C in vacuum: approximately 2.3 OH/nm<sup>2</sup>) and is independent of the silica type.<sup>[94]</sup>

Due to the fact that all silanol types exhibit different reactivities, their distribution is important. Additionally, morphology has an effect on the dehydroxylation and, therefore, on the number and ratio of silanol groups. For example, pore size and particle size play an important role in the spacing of the bridged silanols and hence in the

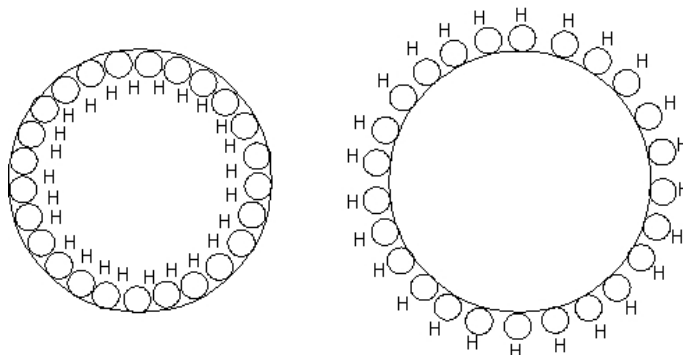


Figure 1.3: Effect of small pore radii and small particle sizes on the hydroxyl spacing<sup>[94]</sup>

strength of hydrogen bonding. Small pores with negative radii of curvature cause a decrease in the intersilanol distance and thus a strengthening of the hydrogen bonding. On the other hand, small particles exhibit positive radii of curvature, resulting in an increase of the intersilanol distance and thus having a destabilizing effect on the bridged silanols (see Figure 1.3).<sup>[94]</sup>

## 1.2.2 Structure of supported vanadia

In literature, the structure of dehydrated vanadia supported by silica is still a matter of discussion with regard to loadings below the formation of crystalline  $V_2O_5$ . Depending on the type of preparation, the maximum amount of this dispersed vanadium oxide species corresponds to 0.5-2.3  $V/nm^2$ .<sup>[45][33][100]</sup> In the following spectroscopic methods that have been employed to reveal the surface structure of vanadia include vibrational spectroscopy such as Raman and IR spectroscopy, UV-vis spectroscopy, NMR and EXAFS.

Hanke et al.<sup>[39]</sup> proposed that the vanadium oxide surface phase consists of vanadia chains with vanadium in tetrahedral coordination, and at higher loadings, of a layered structure based on linked chains with vanadium in both tetrahedral and pyramidal coordination. In addition, especially at higher loadings, it was suggested that another surface phase may be present which contains vanadium in octahedral coordination

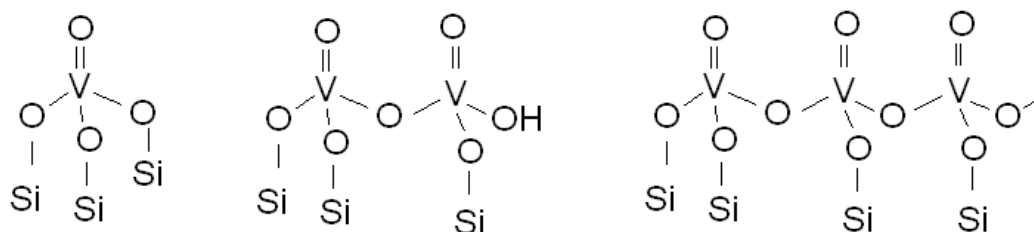


Figure 1.4: Structural motifs of surface vanadium oxide species proposed in literature

but is different from  $V_2O_5$ . This phase transforms into the tetrahedral structure at higher temperatures. Later on, Jonson et al.<sup>[55]</sup> described the structure of dispersed vanadia species as three-legged  $(SiO)_3V=O$  units at low loadings and as chains (or aggregates) of oxygen-bridged vanadium at higher loadings. They excluded the presence of hydroxyl groups in these chains due to results of IR spectroscopy. Similar interpretations, precisely  $(SiO)_3V=O$  type monomers, have been proposed by Oyama et al.<sup>[77]</sup> Surface vanadia species consisting of monomers/polymers with  $VO_4$  coordination geometry as well as ribbons with square pyramidal coordination geometry have been proposed by Schraml-Marth et al.<sup>[84]</sup> Das et al.<sup>[29]</sup> concluded from their studies that only isolated  $VO_4$  species with three legs anchored to the surface were present on silica surface, even at loadings as high as 10 wt%  $V_2O_5$ . The presence of dimeric and oligomeric  $VO_4$  structures at low loadings and the presence of 2D patches of pentacoordinated vanadium at higher loadings have been reported by Arena et al.<sup>[4]</sup> Recently, it has been proposed that at low loadings, silica SBA-15 supported vanadia consists of monomeric species, whereas at higher loadings, polymeric species are present as well.<sup>[30] [64] [58]</sup>

To sum up, one can say that it is now generally accepted that vanadium is present in a distorted tetrahedral coordination with one short vanadyl bond. However, the question whether monomeric species, dimeric/polymeric species or a mixture of both types of species exist is still not fully answered (see Figure 1.4).

Recently, in cooperation with other research groups, we were able to add some important observations to the surface structure of dispersed vanadia supported by SBA-15.



One aspect is the change of hydrated to dehydrated vanadia, which we investigated in combined XPS and Raman study.<sup>[47][46]</sup> Dehydration leads to a depolymerization of the surface vanadia species, accompanied by a change in vanadium coordination. The hydrated state consists of layers of polymerized vanadia with vanadium in pseudo-octahedral coordination and water molecules coordinated to about every second vanadium. After dehydration, these layers transform into small aggregates of polymerized  $\text{VO}_4$  units (dimers and/or oligomers) with tetrahedrally coordinated vanadium. Additionally, the cluster size of most of the surface vanadia species decreases significantly, which leads to an increase of dispersion, as can be seen schematically in Figure 1.5.

Furthermore, the state of vanadium ions in dispersed  $\text{V}_x\text{O}_y/\text{SBA-15}$  was studied with FTIR spectroscopy using CO and NO as probe molecules.<sup>[97]</sup> In this study two types of  $\text{V}^{3+}$  or  $\text{V}^{4+}$  were detected, indicating vanadium sites of different electrophilicity. These ions possess two effective coordinative vacancies. As a result, they can adsorb either two NO molecules to form the respective  $\text{V}^{3+}(\text{NO})_2$  and  $\text{V}^{4+}(\text{NO})_2$  dinitrosyls, or they can adsorb one CO and one NO molecule to form mixed carbonyl-nitrosyls. The introduction of  $\text{O}_2$  to the  $\text{V}_x\text{O}_y/\text{SBA-15-NO}$  system leads to reoxidation of the  $\text{V}^{3+}$  and  $\text{V}^{4+}$  ions to  $\text{V}^{5+}$  and formation of bridged and bidentate surface nitrates. This is an important result, as the formation of bridged nitrates implies the presence of associated vanadium oxide surface species (dimers, polymers).

These results are confirmed by *in situ* X-ray absorption spectroscopy (XAS).<sup>[99]</sup> The spectra of hydrated and dehydrated  $\text{V}_x\text{O}_y/\text{SBA-15}$  were recorded and compared to those of vanadium oxide references. Subsequently, the structures of those references that appeared to be similar to that of  $\text{V}_x\text{O}_y/\text{SBA-15}$  served as model structures for theoretical X-ray absorption fine structure (XAFS) calculations. A valuable agreement between theoretical and experimental XAFS function of hydrated  $\text{V}_x\text{O}_y/\text{SBA-15}$  was obtained assuming a layered  $\text{V}_2\text{O}_5$  like structure, as shown in Figure 1.6. The local structure of dehydrated  $\text{V}_x\text{O}_y/\text{SBA-15}$  is described best by a model structure consisting of an ordered arrangement of neighboring  $\text{V}_2\text{O}_7$  units with tetrahedrally coordinated vanadium centers (see Figure 1.7). The characteristic arrangement of  $\text{V}_2\text{O}_7$

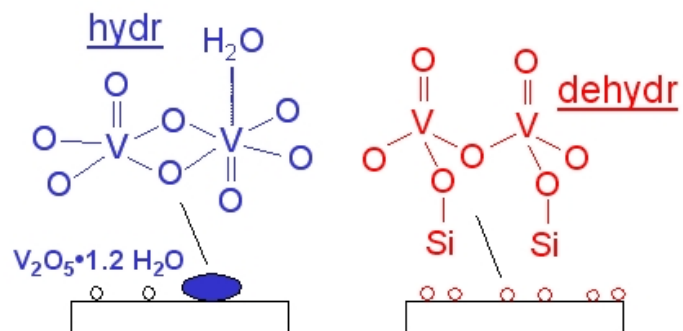


Figure 1.5: Correlation of structure and dispersion for silica SBA-15 supported vanadia<sup>[44]</sup>

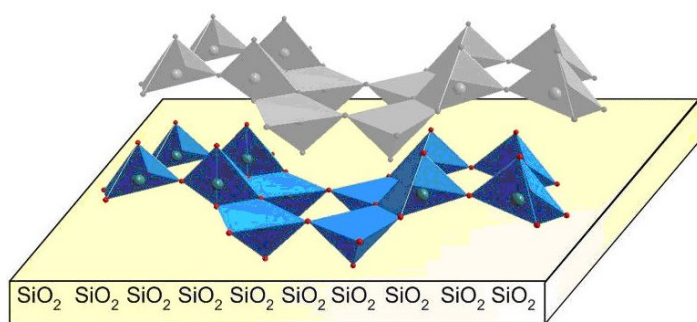


Figure 1.6: Schematic structural representation of hydrated  $\text{V}_x\text{O}_y/\text{SBA-15}$ <sup>[99]</sup>

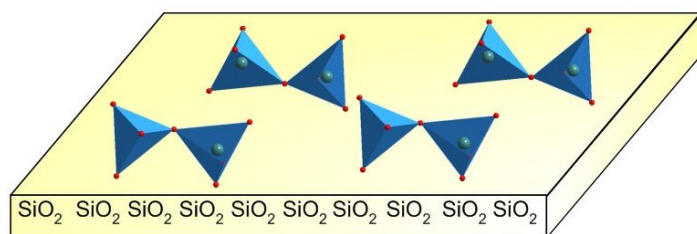


Figure 1.7: Schematic structural representation of dehydrated  $\text{V}_x\text{O}_y/\text{SBA-15}$ <sup>[99]</sup>

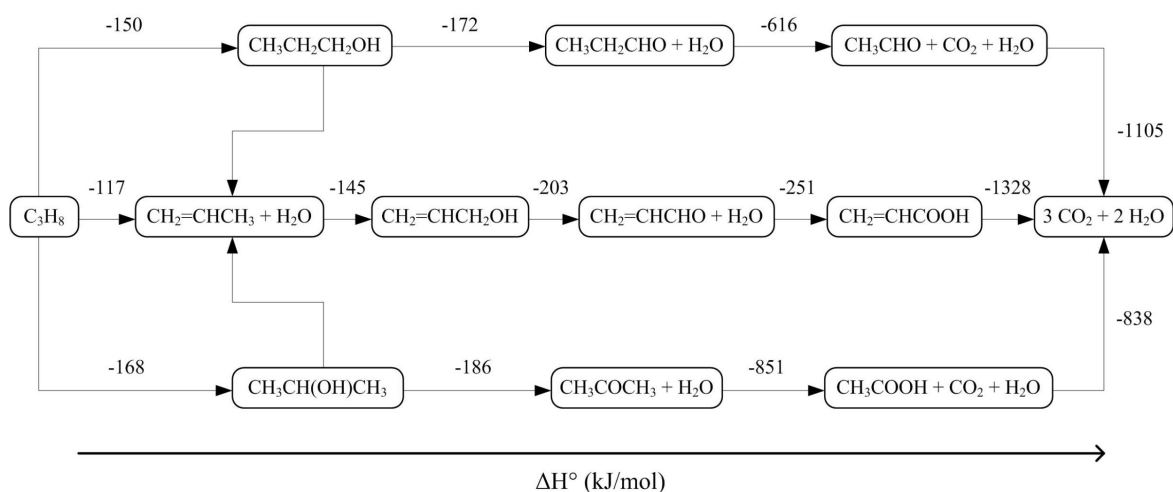


Figure 1.8: Propane oxidation pathways and calculated standard reaction enthalpies [63]

units persisted under reaction conditions.

Moreover, a very similar behavior in IR spectroscopy and XAS of 2.7 wt% V/SBA-15 and 10.8 wt% V/SBA-15 strongly suggests that only minor changes occur in the vanadia structure even up to vanadium loadings, at which the onset of  $V_2O_5$  crystal formation has been observed.

### 1.3 Selective oxidation of propane

The interest in converting low alkanes to various highly desirable petrochemicals or feedstocks for more valuable chemical has dramatically increased in the last decades [63]. Conversion processes include oxidative dehydrogenation, ammoxidation and selective oxidation.

With regard to the  $C_3$  chemistry, propene is industrially used in order to obtain a variety of polymers and intermediates such as polypropylene, acrylonitrile, propylene oxide, cumene/phenol, oxo alcohols, acrylic acid, isopropyl alcohol and oligomers. These derivatives appear in plastics, surface coating materials, synthetic rubbers and synthetic fibre-forming polymers. Another useful way to arrive at these products would be by an oxidation of propane.

Figure 1.8 shows the oxidation pathways and calculated standard reaction enthalpies of propane<sup>[63]</sup>. One possibility would be the oxidative dehydrogenation of propane to propene which can be further oxidized to the desired products in a second step. A much more economic way, however, would be the direct selective oxidation of propane to acrylic acid, for example. Because of the much higher C-H bond strength (about 363 kJ/mol), compared to the C-C bond (about 246 kJ/mol)<sup>[50]</sup>, it is not possible to only use thermal energy for the dehydrogenation. Therefore, a catalyst is used to minimize the C-C bond rupture.

The proposed mechanism of selective oxidation at metal oxide surfaces is the Mars-van-Krevelen mechanism. This mechanism describes a redox-catalytic reaction by participation of lattice oxygen which is replaced by molecular oxygen from the gas phase.<sup>[71] [13]</sup> This means that the oxidation of adsorbed hydrocarbons proceeds through lattice oxygen and results in reduced metal sites. The regeneration of the lattice oxygen vacancies occurs via reoxidation with molecular oxygen of the gas feed. The incorporation of oxygen of the gas feed does not necessarily take place at the same site where the lattice oxygen has been removed before. It can also take place at several other vacancies or as an interstitial atom; the oxygen ions are then transported through the solid. Those oxygen species which activate the hydrocarbons and form water as a by-product of the oxidative dehydrogenation, directly originate from the catalyst and can dissociate to nucleophilic  $O^{2-}$  or electrophilic  $O^-$ ,  $O_2^{2-}$ ,  $O_2^-$  depending on the solid and temperature. The oxygen species adsorbed at the catalyst surface is crucial for the following reaction pathways.<sup>[95] [60] [96] [88]</sup> Total oxidation (CO and CO<sub>2</sub> as products) occurs when electrophilic oxygen take part in the reaction. Selective oxidation products like propene - in the case of propane dehydrogenation - are favored when nucleophilic oxygen participates in the reaction.

## 2 Experimental set-ups and basic principles

### 2.1 Nitrogen adsorption-desorption

The standard method for determining the specific surface area of porous materials is the adsorption of nitrogen at 77 K. The sorption behavior depends on the pore size. The *International Union of Pure Applied Chemistry* (IUPAC) gives the following definition:

Micropores:	inner diameter < 2 nm
Mesopores:	inner diameter 2...50 nm
Macropores:	inner diameter > 50 nm

The size of macropores makes adsorption equal to adsorption on flat surfaces. In micropores, the sorption behavior is mainly determined by the interactions between fluid molecules and pore walls. In addition to the fluid-wall interaction, in mesopores there exists an interaction of the fluid molecules in the middle of the pore. This interaction may cause capillary condensation.

Figure 2.1 shows the different isotherms which can occur during the adsorption-desorption process as classified by the IUPAC in 1985.<sup>[66]</sup> Type I is obtained when adsorption is limited to only a few molecular layers. Type II shows the isotherm for nonporous or macroporous materials with unrestricted monolayer-multilayer adsorption. Inflection point B indicates the change of monolayer coverage to multilayer

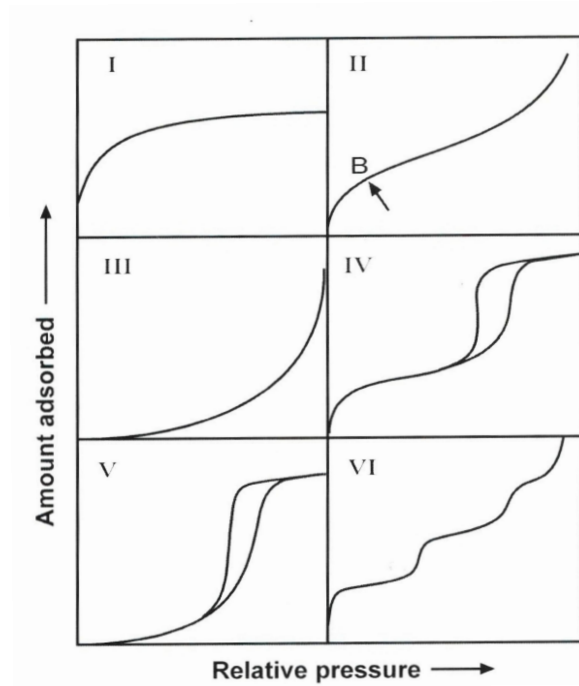


Figure 2.1: IUPAC classification of sorption isotherms<sup>[66]</sup>

coverage. The convex shape of type III implies a relatively weak interaction between adsorbate and adsorbent. This type is not very common. Type IV isotherms are typical of mesoporous materials. The hysteresis loop is due to pore condensation. The lower part of this isotherm shows the same behavior as type II. Type V is a combination of type IV and type III, and type VI is a special case that represents step-by-step adsorption of multilayers.

Using the knowledge about the shape of the isotherm, we can interpret the properties of the system.

### 2.1.1 BET surface area

Different models of calculating the surface area can be applied to the adsorption isotherm. The isotherm model of Brunauer, Emmet and Teller (BET)<sup>[18]</sup> is widely used for this purpose; in order to calculate the surface area using this method, the equation for the free surface is given by<sup>[3]</sup>

$$n^s = \frac{n_m^s C p}{(p_0 - p) \left[ 1 + (C - 1) \frac{p}{p_0} \right]} \quad (2.1)$$

with  $n^s$  being the quantity of gas adsorbed at an equilibrium pressure  $p$ ,  
 $p_0$  being the vapour pressure of the adsorbate in the condensed state at the adsorption temperature,  
 $n_m^s$  being the value of  $n^s$  at a monolayer coverage and  
 $C$  being a constant related to the heat of adsorption into the first layer ( $\Delta H_1$ ) and the heat of condensation of the adsorbate ( $\Delta H_c$ ):

$$C = \mathfrak{R}^{(\Delta H_c - \Delta H_1)RT} \quad (2.2)$$

In equation (2.2),  $\mathfrak{R}$  is another constant and gives the approximate ratio between, on the one hand, the partition function of the internal degrees of freedom for a molecule in the first adsorbed layer, and on the other hand, the partition function of the corresponding quantity for a molecule in the condensed phase.

For plotting the results, a linearized form of equation (2.1) is preferred:

$$\frac{p}{n^s(p_0 - p)} = \frac{(C - 1)p}{n_m^s C p_0} + \frac{1}{n_m^s C} \quad (2.3)$$

Using equation (2.3), the term  $\frac{p}{n^s(p_0 - p)}$  can be plotted against the relative pressure  $\frac{p}{p_0}$ . One can obtain the value of  $n_m^s$  the slope which equals  $\frac{(C-1)}{C n_m^s}$  and the intercept which equals  $\frac{1}{n_m^s C}$ . This shows that the constant  $C$  determines the shape of the isotherm.

Finally the surface area  $A$  of the adsorbent is given by

$$A = A_m^{eff} n_m^s \quad (2.4)$$

where  $A_m^{eff}$  is the effective area per molecule in the monolayer and  $n_m^s$  is expressed in units of adsorbent molecules for a monolayer.

In calculations of the BET surface area, the standard value used for the cross-sectional area of nitrogen is  $16.2 \text{ \AA}^2$ . This gives correct results for carbon surfaces, but not for silica. Nitrogen adsorption on a hydroxylated silica surface requires a cross-sectional area of  $13.5 \text{ \AA}^2$ .<sup>[66]</sup> This means that with the standard BET evaluation, the surface area of our SBA-15 materials would be about 20% larger than it actually is. Hence, the following BET surface area values were all corrected to  $13.5 \text{ \AA}^2$  for silica.

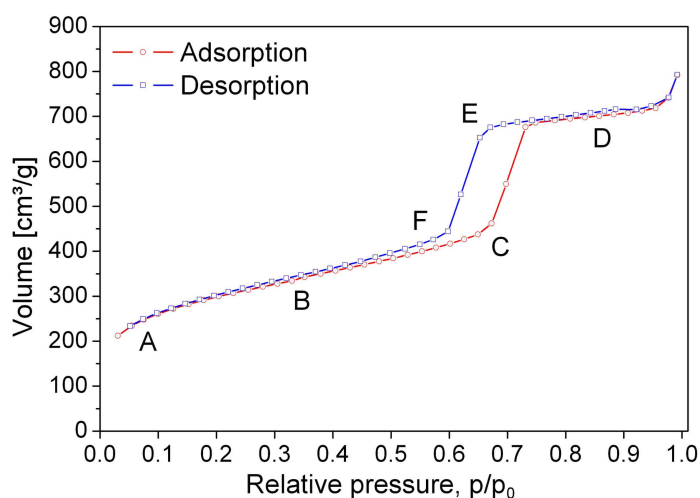


Figure 2.2: Nitrogen adsorption-desorption isotherm of well-ordered mesoporous silica SBA-15

### 2.1.2 Pore size analysis

Pore size can be estimated by using the nitrogen adsorption-desorption isotherm. There are several methods available for micro- and mesopores. But only a few of them, e.g. the BJH method (named after Barrett, Joyner and Halenda<sup>[9]</sup>), can be used for both pore categories. The reason for this is the fact that the different pore size ranges differ with regard to their sorption properties.

Micropores are filled continually because of pore condensation which is a liquid-gas phase transfer of first order.

The mechanism of filling the mesopores can be explained by means of Figure 2.2. In section (A), the formation of a mono-molecular layer is initiated and continued by multi-molecular layers in section (B). When a critical film thickness is achieved (point C), capillary condensation starts. This process is indicated by the sudden increase of the adsorption isotherm. The following plateau in section (D) originates from completely filled pores with a hemispherical boundary layer. When the desorption starts, the boundary layer is curved to the inside of the pores with the effect of the evaporation taking place at lower pressures than the condensation. In section (F) the desorption happens again in multi- and later in mono-molecular layers. As a result of this mechanism, a hysteresis loop appears.

The shape of this hysteresis loop contains information about the pore design. Fig-



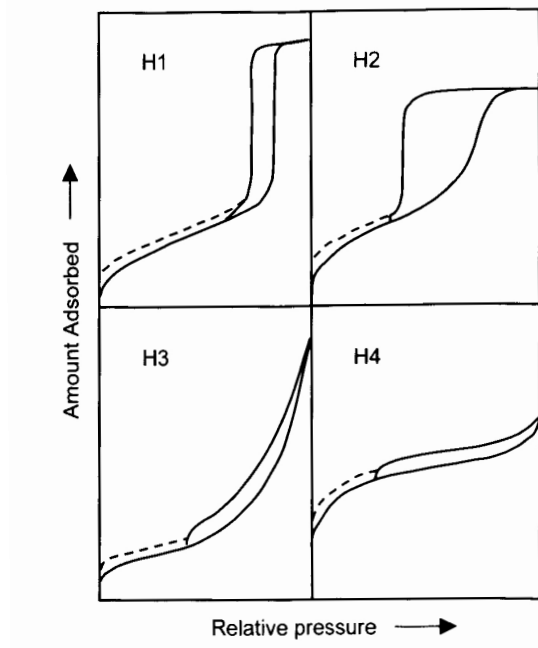


Figure 2.3: IUPAC classification of hysteresis loops in sorption isotherms<sup>[66]</sup>

Figure 2.3 shows the classification according to the IUPAC. H1 represents well-defined cylindrical pores or close agglomerates of uniform spheres. H2 indicates some disorder in the pore structure, which means that pore size distribution and shape are not well-defined. Isotherms of the H3 shape do not display an adsorption plateau. This is typical of agglomerates of flat particles which result in the occurrence of slit pores. H4 stands for slit pores with a large number of micropores.

### Pore size determination for mesopores

The basic equation for pore size distribution is generally the Kelvin Equation<sup>[66]</sup>, which gives the correlation between vapor pressure equilibrium and the curved surface belonging to it:

$$\ln(p/p_0) = \frac{-2\gamma\bar{V}}{rRT} \quad (2.5)$$

with  $\gamma$  - surface tension  
 $\bar{V}$  - molar volume of the condensed liquid  
 $r$  - pore radius  
 $R$  - gas constant

$T$  - temperature

$p/p_0$  - relative pressure

The most common model for pore size analysis is the BJH method. This model assumes cylindrical pores and is based on numeric calculation methods.<sup>[9]</sup> However, thorough investigation has shown that classical methods using macroscopic thermodynamic assumptions underestimate the pore size, whereas microscopic methods, e.g. Non Local Density Function Theory (NLDFT), allow a rather accurate pore size analysis of the whole range of micro- and mesopores.<sup>[66]</sup> The DFT approach is based on the intermolecular potential of fluid-fluid and fluid-solid interactions and allows the construction of adsorption isotherms in model pores.<sup>[79]</sup>

The question whether the adsorption or the desorption branch should be used for pore size analysis is answered by the model used. During the process of adsorption, the system is metastable due to spontaneous condensation. During the process of desorption, a phase transition equilibrium is dominant. This means that methods which are based on this equilibrium, e.g. BJH, have to be applied to the desorption branch. The DFT method is normally also used for the desorption branch, but there exists a special NLDFT spinodal condensation method which can be used for the adsorption branch.<sup>[79]</sup>

The average pore size can be estimated by using the total pore volume and the surface area. The total pore volume  $V_p$  is defined as the liquid volume  $\Delta V_{liq}$  at a pressure  $p/p_0$  after pore condensation is finished, usually at  $p/p_0 = 0.95$ . The volume of liquid at this relative pressure corresponds to the measured adsorbed gas volume  $\Delta V_{gas}$ . The most direct way to convert  $\Delta V_{gas}$  to  $\Delta V_{liq}$  is to calculate the moles of gas and multiply them by the liquid molar volume. For nitrogen at standard temperature and pressure, the equation is formulated as follows:<sup>[66]</sup>

$$\Delta V_{liq} = \frac{\Delta V_{gas}}{22.4 \cdot 10^3} \cdot 34.6 = \Delta V_{gas} (1.54 \cdot 10^{-3}) \text{ cm}^3 \quad . \quad (2.6)$$

The adsorption-desorption isotherm (40 points each branch) was measured on a Quantachrome Autosorb 1 after pretreatment for 8 h at 80 °C and  $2.6 \cdot 10^{-2}$  mbar. Data

analysis was done by the corresponding software using multi-point BET analysis, average pore volume ( $p/p_0 = 0.95$ ) and for the pore size distribution the DFT method ( $dV(w)$ ). As presetting for the DFT pore size analysis *data reduction parameters* were chosen as following: *nitrogen* as adsorbate, *oxygen (zeolite)* as adsorbent and  *$N_2$  at 77 K on silica (NLDFT equilibrium model)* in order to calculate the pore size distribution of the desorption branch.

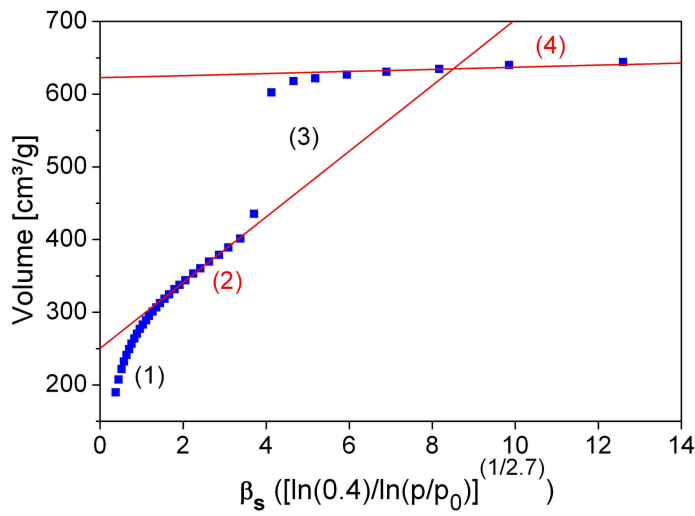


Figure 2.4:  $\beta_s$ -plot of well-ordered mesoporous silica SBA-15

### Pore size determination for micropores

There are several methods for calculating the pore size as well as the volume of micropores. One of them is the  $\alpha_s$ -method developed by Gregg and Sing<sup>[37]</sup>. The volume of micropores can be derived from a standard adsorption plot using an appropriate nonporous reference material. In this standard adsorption plot the adsorbed volume of the sample is plotted against

$$\alpha_s = \frac{v_{ads}(p/p_0)}{v_{ads}(0.4)} \quad (2.7)$$

of the reference material.

In order to simplify this procedure  $\alpha_s$  can be replaced by  $\beta_s$ . Instead of using  $v_{ads}$  the

statistical thickness of the adsorbed gas layer determined from the Frenkel-Halsey-Hill (FHH) theory<sup>[37]</sup> is applied. According to FHH theory,  $\ln(p/p_0) = \alpha t^{-2.7}$ , so  $\beta_s = [\ln(0.4)/\ln(p/p_0)]^{(1/2.7)}$  can be used as a substitute for  $\alpha_s$  over the relative pressure range of 0.05 - 0.995.

The  $\beta_s$  plots for mesoporous SBA-15 have four distinct regions (see Figure 2.4): (1) a curved, low pressure adsorption region due to adsorption in micropores; (2) a linear region due to multilayer adsorption in mesopores and on the external surface of the material; (3) a steep region due to capillary condensation in the mesopores; (4) a linear region due to multilayer adsorption on the external surface of the material. A linear fit to region (2) has the form  $v_{ads} = m_{nonmicro}\beta_s + v_{micro}$  and a linear fit to region (4) has the form  $v_{ads} = m_{ext}\beta_s + v_{meso+micro}$ <sup>[69]</sup>. That means that from both intercepts the fraction of micropore and mesopore volume can be estimated.

## 2.2 X-ray diffraction

Because of their wavelength in the Ångström range, X-rays are able to penetrate solids and can give information about the bulk phase, particle size, and the kinetics of bulk transformations of long-range ordered materials. In catalyst characterization it is mainly used to identify the crystallographic phases.

X-ray diffraction (XRD) is the elastic scattering of X-ray photons by atoms in a periodic lattice causing constructive interference. The photon scattering follows the Bragg relation, which is given by

$$n\lambda = 2d \sin \Theta; \quad n = 1, 2, \dots \quad (2.8)$$

with  $\lambda$  being the wavelength of the X-rays,

$d$  being the distance between two lattice planes,

$\Theta$  being the angle between the incoming X-rays and the normal to the reflecting lattice plane and

$n$  being the integer naming the order of the reflection.<sup>[74]</sup>

In Bragg's law the lattice spacings can be calculated by measuring at the angles of  $2\theta$ . Different crystal structures and compounds possess characteristic lattice spacings. For the investigations of powdered samples a stationary X-ray source and a movable detector are used in order to deal with the various orientations of the particles. The detector scans the intensity of the diffracted radiation as a function of the angle  $2\theta$  between the incoming and the diffracted beams.

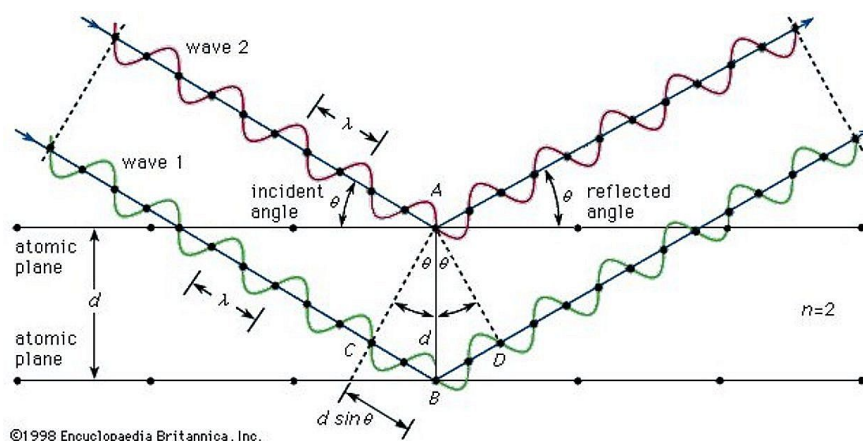


Figure 2.5: Bragg diffraction

## Small-angle XRD

For highly-ordered mesoporous samples, XRD peaks can be found at values of  $2\theta$  between nearly zero and 10. In this case, the X-rays are diffracted not at the atomic lattice but at the pores of the material. From values measured at  $2\theta$  the spacing between the centers of the pores (unit cell parameter  $a$ ) can be estimated (see Figure 2.6).

The X-ray diffraction measurements were performed on a STOE STADI P transmission diffractometer equipped with a primary focusing Ge monochromator (Cu K 1 radiation) and scintillation counter. In order to improve the accuracy of the  $2\theta$  scale in small angle XRD, a measurement mode with two symmetric scans (negative and positive  $2\theta$ ) was chosen. Small amounts of powdered sample were sandwiched be-

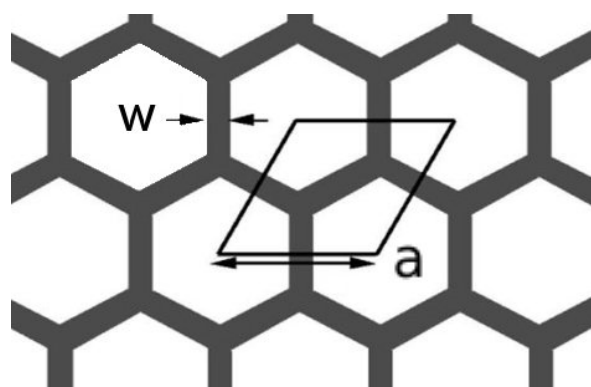


Figure 2.6: Geometry of hexagonal pores<sup>[31]</sup>

tween two layers of polyacetate film and fixed with a small amount of X-ray amorphous grease. This sandwich was clamped into a sample holder ring.

## 2.3 X-ray photoelectron spectroscopy

X-Ray photoelectron spectroscopy (XPS) is based on the photoelectric effect, in which electrons are emitted when light of a sufficiently small wavelength irradiates a sample. This means that a photon of the energy  $h\nu$  is absorbed by an atom, and in order to release  $h\nu$ , a core electron with binding energy  $E_B$  is ejected with a kinetic energy  $E_K$ . Including  $\phi$ , the work function of the spectrometer, the kinetic energy of the photoelectron can be described as<sup>[16]</sup>

$$E_K = h\nu - E_B - \phi \quad . \quad (2.9)$$

The binding energy of a photoelectron does not exactly equal the energy of the orbital from which it is released. Its energy value includes information about the state of the atom before photo-ionization (initial state) and about the core-ionized atom left behind (final state).

The nomenclature of photoelectron peaks is assigned to the orbital momentum  $l$  and spin momentum  $s$  of its origin. The orbital momentum  $l = 0, 1, 2, 3, \dots$  corresponds to s, p, d, f,.. and the spins take values  $s = \pm 1/2$ . Thus, each level with  $l \geq 1$  has two sublevels with an energy difference, the so called spin-orbit splitting.

Due to the fact that a set of binding energies is characteristic of an element, XPS

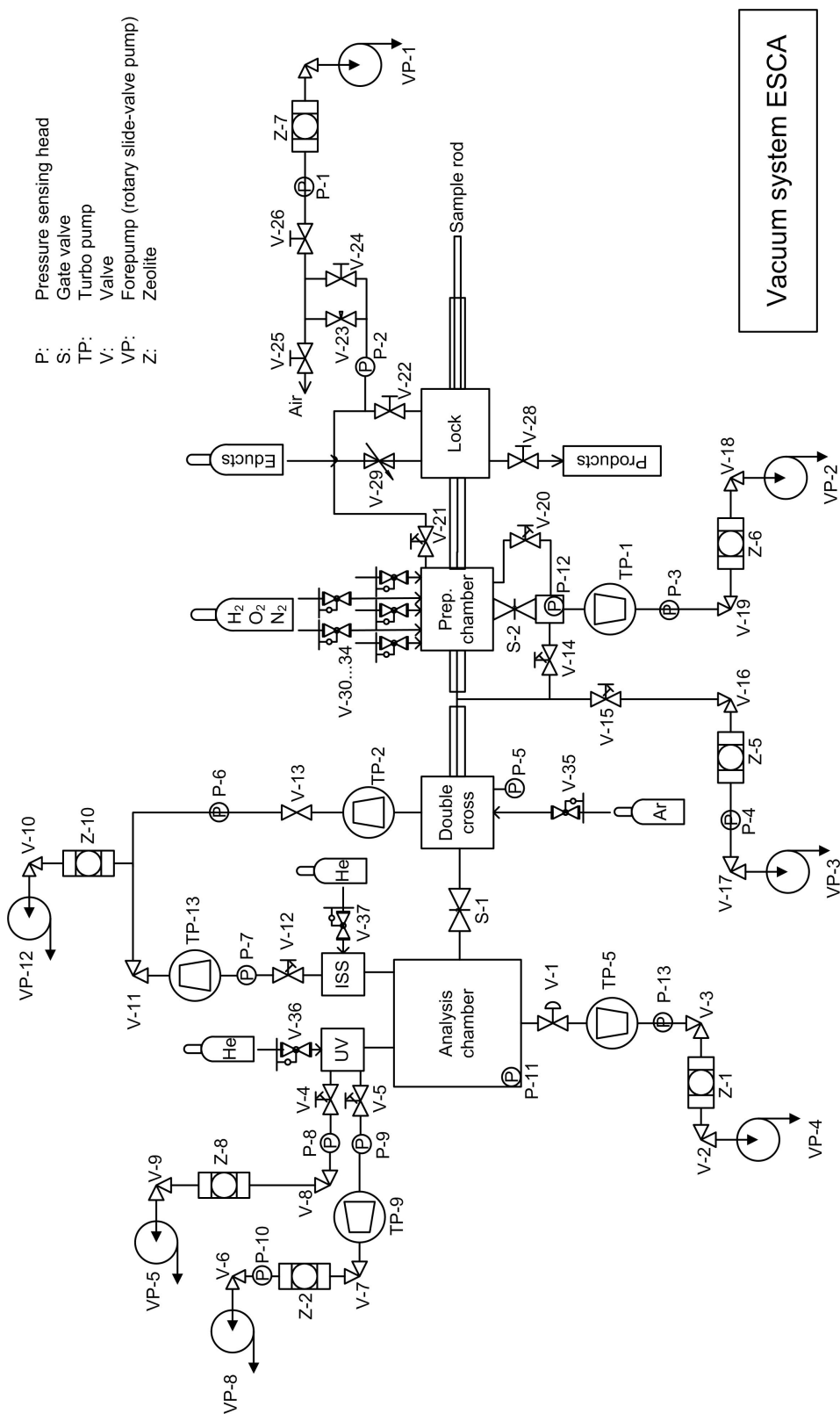


Figure 2.7: Vacuum system ESCA

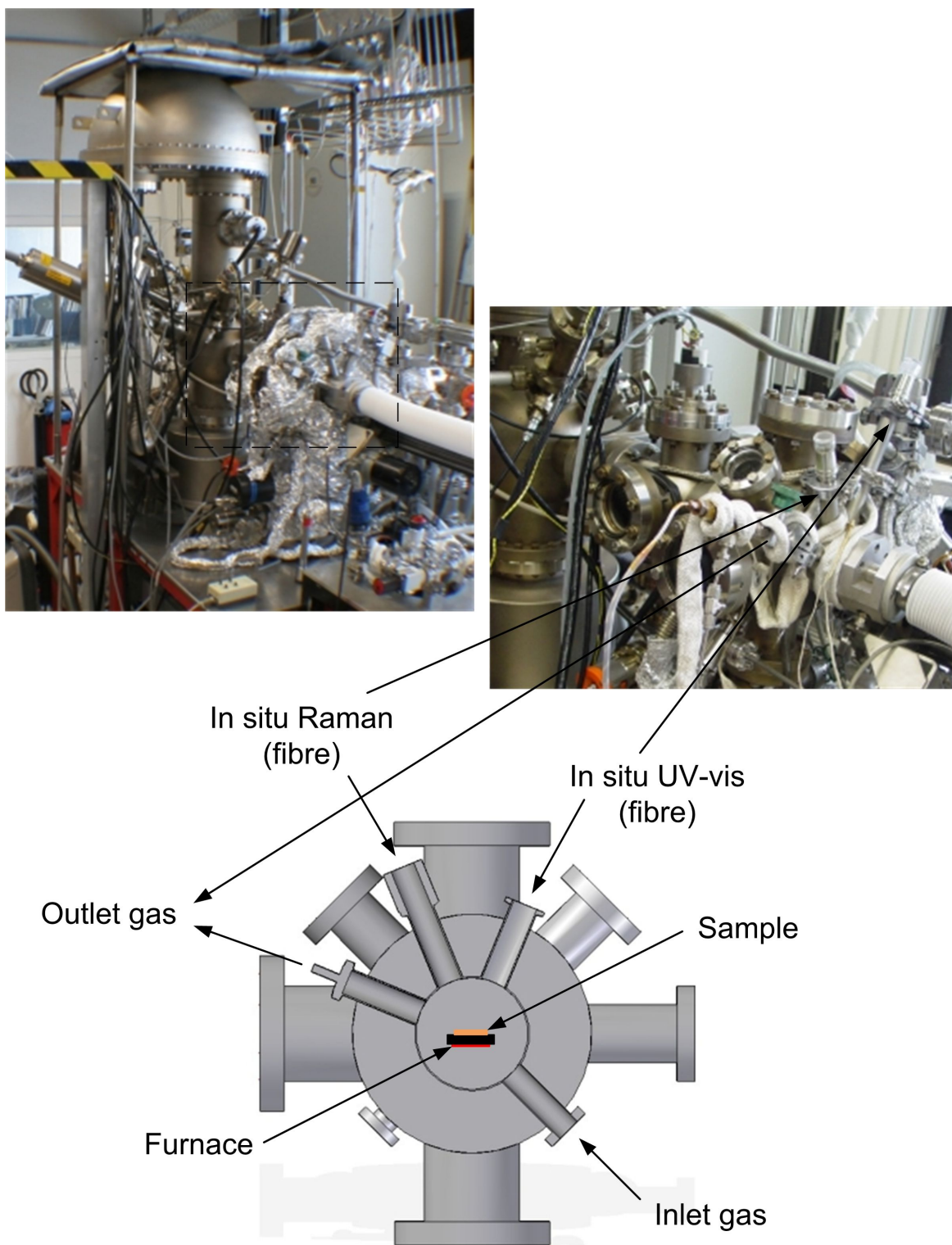


Figure 2.8: ESCA set-up for combined Raman spectroscopy, XPS and DRUV-vis spectroscopy



can be used to analyze the composition of samples.<sup>[74]</sup> Furthermore, the spectrum contains chemical information, because the energy levels of core electrons are related to the chemical state of the atom. XPS is a surface sensitive method. The penetration depth of the photons is about 1-10  $\mu\text{m}$ <sup>[73]</sup>, but the information depth depends on the mean free path of the photoelectrons. For electrons with kinetic energies in the range of 15-1000 eV, the mean free path is limited to 1-2 nm<sup>[74]</sup>, which determines the sampling depth. In the case of mesoporous SBA-15 information from inside the pores can be obtained due to random orientation of the particles in a powder sample.

The concentration of an element in a sample can be estimated by the relative intensities of the core-level peaks. For this application, the atomic photo-emission cross-sections were calculated by Scofield<sup>[16]</sup>.

The full width at half maximum (FWHM) of the core level peak can be used for analyzing a sample with XPS, too. This value is a convolution of the natural or inherent width  $FWHM_{cl}$  of the core level, the width  $FWHM_{ph}$  of the photon source (X-ray line) and the analyser resolution  $FWHM_a$  following (assuming Gaussian line shape for each one) the Equation<sup>[16]</sup>

$$FWHM = (FWHM_{cl}^2 + FWHM_{ph}^2 + FWHM_a^2)^{1/2} \quad (2.10)$$

Apart from the peaks arising directly from the sample, there are several additional features in XP spectra. X-ray satellites can occur if a non monochromatic X-ray source is used. In this case, there appear lower intensity lines next to the main feature, which can be subtracted by using a routine provided by different XPS analysis programs.

Furthermore, electrically insulating samples may be charged. For conductive samples, the lost photoelectrons are refilled by a current from the sample holder and by a flow of Auger electrons and secondary electrons from the source window. If this is not the case, the sample is positively charged, which is visually represented as a shift of the whole spectrum to higher binding energies. If the sample is charged inhomogeneously, peaks tend to become broader (differential charging).

The measurements were done on a modified LHS/SPECS EA200 MCD system equipped

with a MgK $\alpha$  source (1253.6 eV, 168 W). This modified set up is shown in Figure 2.7 and 2.8. The scheme of the vacuum systems shows four chambers which have to be evacuated. When a sample was inserted, it was slowly evacuated in the lock to  $2.5 \cdot 10^{-2}$  mbar (P-1) and transferred to the preparation chamber. When the pressure in this chamber reached  $5 \cdot 10^{-8}$  mbar (P-12), the sample was transferred further on to the double cross ( $1 \cdot 10^{-7}$  mbar (P-5)). The sealing between the preparation chamber and the double cross was differentially pumped ( $6 \cdot 10^{-2}$  mbar (P-4)). The double cross and the analysis chamber were separated by a gate valve which was only opened during measurements. The pressure in the analysis chamber was  $1 \cdot 10^{-10}$  mbar (P-11) during separation from the the double cross and  $1 \cdot 10^{-9}$  mbar during the measurement.

The gate of the vacuum system of the ESCA set up was modified in order to use it under flow conditions. Supplementary, there are two flanges provided where a Raman fiber and a UV-vis fiber can be inserted.<sup>[43]</sup> The powder samples were placed on a stainless steel sample holder with a 0.6 mm deep rectangular well of 12 mm x 8 mm. This area was completely covered. The sample could be heated via a furnace directly beneath the sample holder. For typical XPS measurements, the sample was pretreated under a flow (50 ml/s) of 20% O<sub>2</sub> in N<sub>2</sub> at 350 °C for 30 min before it was evacuated and transferred to the analysis chamber. The spectrum of each sample was recorded over a time period of 40 min.

The data were analyzed by using software called SciPlot 3.9n. The standard procedure consists of satellite subtraction and Shirley background subtraction. The binding energy was corrected by using 103.6 eV as reference binding energy of the Si2p<sup>[73]</sup> and by the shifting the whole spectrum. The spectra were normalized to the area of the Si2p peak.

## 2.4 Electron microscopy

Electron Microscopy allows an identification of size and shape of support particles. Further information about the composition and structure can be obtained by evaluat-

ing the interactions between the primary electron beam and the sample.

Figure 2.9 shows the main processes that can occur when electrons of energy between 100 and 400 keV hit the sample. When colliding with atoms, the electrons can simply

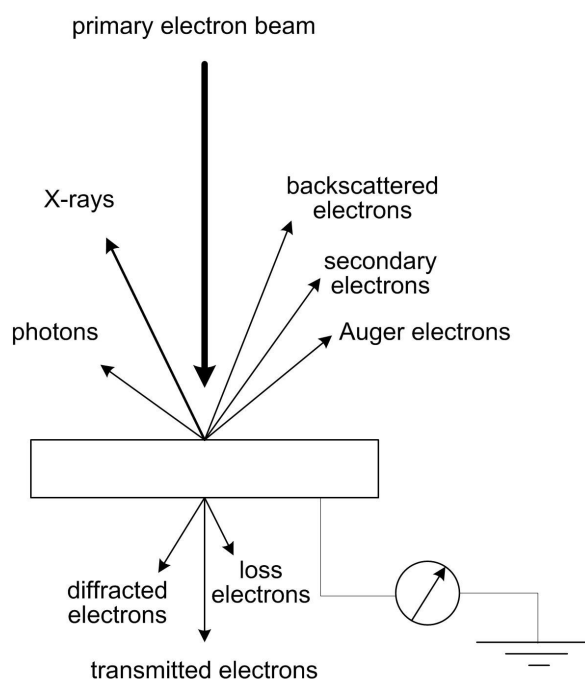


Figure 2.9: Interaction between primary electrons and the sample in electron microscopy <sup>[74]</sup>

be scattered back or they can collide inelastically and transfer their energy to secondary electrons. Other electrons pass through the sample with or without suffering energy loss or can be diffracted by particles. Auger electrons and X-rays are formed during relaxation processes of core-ionized atoms. Photons in the range from UV to infrared are mainly caused by recombination of electron-hole pairs in the sample.

### 2.4.1 Transmission electron microscopy

Images from transmission electron microscopy (TEM) result from transmitted and diffracted electrons. Primary electrons hit the sample in parallel rays, producing two-dimensional images because of the different density and thickness of the sample. The magnified image resulting from these transmitted electrons is a so-called bright-field

image. The diffracted electrons produce a dark-field image. The resolution is typically about 0.2 nm.<sup>[10]</sup>

TEM pictures were obtained on a Philips CM 200 LaB6 at an acceleration voltage of 200 kV.

### **2.4.2 Scanning electron microscopy**

In scanning electron microscopy (SEM), the yield of either secondary electrons or backscattered electrons is determined as a function of the location of the precisely focused primary electron beam which is scanning the surface. The image results from the different energies of the electrons. Secondary electrons, whose energy usually is relatively low, emerge from the sample surface and appear darker than the backscattered electrons. The latter emerge from deeper regions of the sample, and their brightness depends on the weight of the elements from which the electrons emerge (higher weight means higher brightness). The resolution is typically about 5 nm.<sup>[10]</sup>

SEM pictures were obtained on a Hitachi S4800 at an acceleration voltage of 1.5 kV.

## **2.5 UV-vis spectroscopy**

UV-vis spectroscopy is based on the absorption of energy in the ultraviolet (UV) and the visible range of electromagnetic radiation (50 000 ...13 000 cm<sup>-1</sup>). The absorption induces an excitation of an electron from a lower to a higher atomic or molecular energy level.

In covalent inorganic and organic molecules, both the excitation of a non-bonding electron towards the status of an anti-bonding molecular  $\pi$  orbital ( $n-\pi^*$  electronic transition) as well as the excitation from a bonding into an anti-bonding  $\pi$  orbital ( $\pi-\pi^*$  electronic transition) can be observed. Another type of electron transferring processes in UV-vis is the charge transfer (CT) excitation. During this process, a large fraction of an electronic density is transferred from one region of a molecular en-

tity to another.  $d-d$  transitions are observable when degenerate  $d$  orbitals of transition metal ions are split. The way in which energy levels split is influenced by the number of  $d$  electrons, by the effective charge of the involved ion and by the distribution and charge of the surrounding anions.

Transitions within one ion occur usually in the visible part of the spectrum, whereas charge transfer transitions between atoms occur in the UV range. The UV-vis spectrum can give information about the oxidation state and the environmental symmetry of transition metal ions, e.g. tetrahedrally or octahedrally coordinated ions and the degree of polymerization.

Powders are measured in reflectance mode due to of their low transparency. For reflectance mode two components can be distinguished: *Specular reflectance* in which the angle of incidence equals the angle of reflection and *Diffuse reflectance* in which absorbed photons are reflected into a broad range of directions. In order to collect diffuse reflected light, integration spheres are used in UV-Vis spectrometers. The DR-UV-vis spectrum can be described by the Kubelka-Munk function  $F$ :

$$F = \frac{(1 - \tilde{R}_{Norm})^2}{2\tilde{R}_{Norm}} \quad (2.11)$$

with

$$\tilde{R}_{Norm} = \frac{\tilde{R}_{sample}}{\tilde{R}_{ref}} \quad (2.12)$$

with  $\tilde{R}_{sample}$  being the reflectance of the sample  
and  $\tilde{R}_{ref}$  being the reflectance of a reference material with a reflectance of 100% ("white standard").

Diffuse reflectance UV-vis spectra were measured with the help of a Perkin-Elmer Lambda 950 spectrometer equipped with a Harrick diffuse reflectance attachment. The optical system consisted of an all reflecting optical system equipped with a holographic grating monochromator with 1440 lines/mm UV-vis blazed at 240 nm, a photomultiplier R6872 for high energy in the entire UV-vis wavelength range as detector and a tungsten-halogen and deuterium source. Measurements can be taken at an overall

inelastic scattering	elastic scattering	inelastic scattering
$\Delta E_M > 0$ $\nu = \nu_0 - \nu_{\text{vib}} < \nu_0$	$\Delta E_M = 0$ $\nu = \nu_0$	$\Delta E_M < 0$ $\nu' = \nu_0 + \nu_{\text{vib}} > \nu_0$
Stokes	Rayleigh	Anti-Stokes

Figure 2.10: Schematic representation of vibrational Raman scattering

wavelength range of 175 - 3300 nm.

Samples were measured during heating with 10 K/min up to 350 °C under 20% O<sub>2</sub> in N<sub>2</sub> flow, and again after cooling down to room temperature. The used white standard was BaSO<sub>4</sub>. The measurements were recorded by PerkinElmer UV WinLab 5.2.0 software.

## 2.6 Raman spectroscopy

Raman spectroscopy is based on the electronic polarization of molecules caused by incident electromagnetic radiation. Most of the photons are elastically scattered, which means that they have the same energy as the incident photons (Rayleigh scattering). Only a very small fraction (about 1/1000 of the scattered photons<sup>[40]</sup>) is inelastically scattered. During this process the energy of vibrational states may be exchanged, and photons with a lower or higher energy are emitted. The energy difference is equal to the vibrational energy generated or, respectively, destroyed. For molecules in their vibrational ground state, the frequencies of the emitted photons are red-shifted and are called Stokes lines. If molecules are not in their vibrational ground states, the

emitted photons are blue-shifted and called Anti-Stokes. A schematic representation of these processes is shown in Figure 2.10.

Another effect which is often observed is fluorescence. Fluorescence appears when the electronic state of a molecule with one or more vibrational modes contributes to the fine structure of the band. Fluorescence can enhance the difficulty of obtaining a good spectrum, because it creates a strong broad background making it problematic to observe weak Raman lines. A separation by filters or monochromators is not possible, because the frequencies of the fluorescence can appear in a similar range as the Raman bands.<sup>[11]</sup>

Figure 2.11 shows schematically the Raman set-up used. Possible excitation source

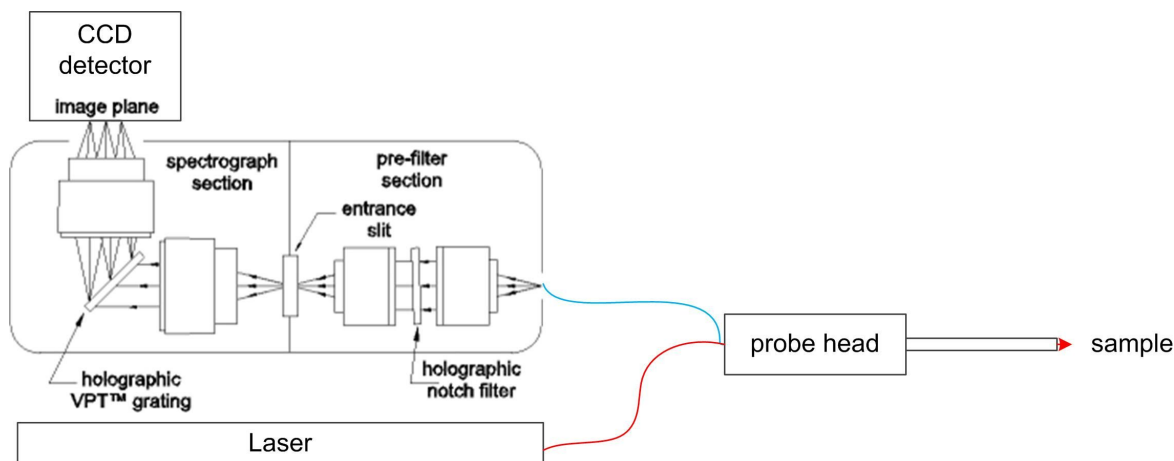


Figure 2.11: Raman set-up

can either be an argon ion laser with a wavelength of 514 nm or 488 nm, or a helium neon laser with a wavelength of 632 nm (Melles Griot, laser power 100 mW, maximum power for at the sample 25 mW (514 and 488 nm) and 10 mW (632 nm)). The emitted laser light is delivered to the probe via a single excitation fiber, and the scattered radiation collected from the sample is delivered to the spectrograph by a single collection fiber. As the intensity of the Rayleigh scattering is several orders of magnitude higher than that of the Stokes lines, part of the Rayleigh scattering is filtered out in the probe. The remaining part is attenuated by a notch filter in the spectrograph

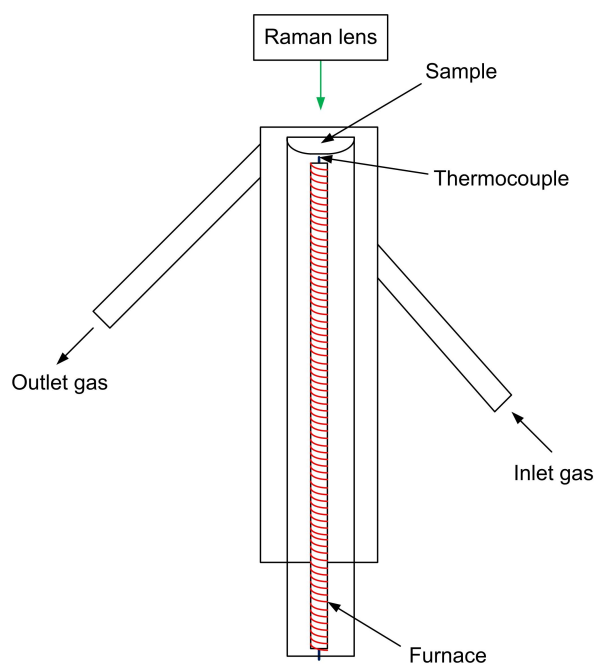


Figure 2.12: *In situ* Raman cell

(Kaiser Optical, HL5R with CCD,  $5\text{ cm}^{-1}$  spectral resolution). The Raman-scattered photons are focused in an entrance slit and pass through a transmission grating for wavelength separation. A Peltier-cooled CCD detector records the intensity of the Raman signal over the wavelength range of  $0 - 4000\text{ cm}^{-1}$  at once by dispersing the whole spectrum in two parts over the CCD. The resulting spectrum was recorded with HoloGRAMS software V1.0 and processed with the *Auto New Dark* and *Cosmic Ray Filter* functions. The wavelength axis was calibrated each time after changing the laser wavelength and optical devices with an argon or neon source. The laser wavelength was calibrated with cyclohexane before each start of the set-up. The Raman spectrum of cyclohexane was recorded and the band which appears around  $800\text{ cm}^{-1}$  was set to the literature value provided by the HoloGRAMS software ( $801.8\text{ cm}^{-1}$ ).

Raman spectra were measured at room temperature with an excitation wavelength of  $514\text{ nm}$  and a power of  $3\text{ mW}$  (measured with Ophir P/N 1J06013 Laser power/energy monitor). The probe head could either be connected with a fiber (spot size  $15 - 30\text{ }\mu\text{m}$ ) or an objective (Olympus  $10\times/0.25$ ). *In situ* Raman spectroscopy was done by using



the modified gate of the XPS set up (Figure 2.8), or an *in situ* Raman cell. Figure 2.12 shows the design of this Raman cell consisting of two cylindrical glass bodies. The both tubes are closed at the end above and fit in each other. The inner tube provides a well at the top for placing the powder sample in it. Reaction gas can flow in and out the cell through two glass tubes connected to the outer glass body. The sample is heated inside the inner tube by a resistance heating of a wire coiled up on a ceramic tube. A thermocouple is placed inside the ceramic tube to monitor the temperature. The fiber probe was used for measurements in the modified gate of the XPS set-up and for measurements without a cell. The objective was used for measurements with the *in situ* Raman cell, and again, for measurements without a cell.

If not mentioned otherwise, the samples were pretreated under 20% O<sub>2</sub> / N<sub>2</sub> flow and 350 °C for 30 min.

## 2.7 Temperature programmed reduction and oxidation

By using temperature programmed reaction methods a chemical reaction is recorded during a linear temperature increase in time. This chemical reaction can be, for instance, a reduction (TPR), an oxidation (TPO), or a desorption (TPD). The thermal analysis methods can give qualitative and quantitative information. A reaction-temperature profile can be easily compared with systems that are already known, or it can be used to compare catalysts of different chemical composition. From the amount of the used H<sub>2</sub>/O<sub>2</sub> used, the average oxidation state can be calculated. Furthermore, the temperature-programmed reaction pattern provides useful information about the temperature needed for complete reduction/oxidation of a sample.

The gas mixture used is usually 5% H<sub>2</sub> in Ar (for the oxidation: 5% O<sub>2</sub> in He), which passes a thermal conductivity detector before entering and after leaving the reactor. The heating rate during the measurement is usually 0.1 to 20 °C/min<sup>[74]</sup>. In order to remove traces of water, which would disturb the thermal conductivity measurement, a dryer is placed between the reactor and the thermal conductivity detector. The

output of these measurements is a plot of the hydrogen/oxygen consumption of the catalyst as a function of temperature.

TPR/O measurements were done on a CE Instruments TPD/R/O 1100 using CuO as a calibration standard. 50 mg of the respective sample were pretreated at 150 °C in Ar and heated with 10 °C/min up to 800 °C. The temperature profile was monitored in the middle of the sample and in the furnace.

### **2.8 Catalytic tests**

The catalyst materials were tested for partial oxidation of propane using a U-shaped fixed bed quartz reactor with an inner diameter of 6 mm. This reactor was placed in a fluidized bed of sand serving as a source of heat in order to provide operating conditions that are nearly isothermal.

To ensure the same intrinsic activity and selectivity for all samples tested, a particle size of a sieve fraction of 200...300  $\mu\text{m}$  was used. The amount of catalyst material used (250 mg for SBA-15 and 500 mg for A300 samples) was chosen according to the vanadium loading in order to reach comparable conversions. The pure catalyst was set between two layers of quartz particles to provide plug flow conditions. The feed was composed of synthetic air (20.5% O<sub>2</sub> in N<sub>2</sub>) and propane and mixed in the stoichiometric ratio of propane to oxygen of 2 (29.1% C<sub>3</sub>H<sub>8</sub>, 14.5% O<sub>2</sub>, 56.4% N<sub>2</sub>). The total gas flow of the reaction mixture was modified in the range of 25...250 ml/min, then passed a static mixer and was preheated up to 100 °C. The reaction temperature was 500 °C at atmospheric pressure.

The feed and product components leaving the reactor were analyzed by an on-line gas chromatograph (GC, Satochrom 5873), equipped with PoraPLOT Q and Molsieve 5 columns. The Molsieve 5 column allows a high resolution of permanent gases like the inert gases H<sub>2</sub>, O<sub>2</sub>, and N<sub>2</sub>. The PoraPLOT column elute polar compounds, e.g. alcohols, water, polar solvents, hydrocarbons and gases, as perfectly symmetrical peaks, allowing them to be analyzed together with light hydrocarbons or permanent gases.

Light gases ( $O_2$ ,  $N_2$ ,  $CO$ ,  $CH_4$ ,  $CO_2$ ) were detected with a thermal conductivity detector, while  $C_2$  and  $C_3$  hydrocarbons were quantified using a flame ionization detector. Apart from propene, water, and  $CO_x$ , traces of methanol and ethene were found as reaction products. Data analysis was done on the basis of carbon balance. The conversion  $X$  of propane and the selectivity  $S$  towards propene were calculated using the equations:<sup>[61]</sup>

$$X = \frac{c_{C_3H_8,0} - c_{C_3H_8}}{c_{C_3H_8,0}} \quad (2.13)$$

and

$$S = \frac{c_{C_3H_6}}{c_{C_3H_8,0} - c_{C_3H_8}} \quad , \quad (2.14)$$

with  $c_{i,0}$  being the propane/propene concentration at the reactor inlet and  $c_i$  at the reactor outlet. The tested vanadia samples supported on different silicas had different BET surface areas, but similar vanadium loadings ( $0.7 \text{ Vatoms/nm}^2$ ). For this reason, a modified residence time  $\tau_{mod}$  was calculated in order to compare the conversion of propane:

$$\tau_{mod} = \frac{m_V}{\dot{n}} \quad (2.15)$$

In this case, catalyst volume, which would normally be used in that equation, is replaced by the amount of vanadia  $m_V$ , and then divided by the flow rate of the amount of substance of the reaction gas  $\dot{n}$ . This is due to the fact, that the catalyst volume does not adequately represent the number of active sites in each sample.



# 3 Synthesis of silica-supported vanadia catalysts

## 3.1 Synthesis of SBA-15

SBA-15 was synthesized according to Zhao et al.<sup>[104]</sup>. For the first samples, 4.07 g Pluronic P123 (BASF) were dissolved in 30 ml double distilled water (two-stage quartz glass, Heraeus) and 120 ml two molar HCl in a closed PE bottle standing in an oil bath of 35 °C. After a clear solution was obtained (about 1 h), 9 ml tetraethoxysilane (TEOS, 99+%, Alfa Aesar) were added, and the now cloudy solution was stirred for 20 h at 35 °C. After aging for 24 h at 85 °C, the suspension was filtered and washed over a nutsch filter (frit with porosity 4) and a vacuum flask. For the washing procedure, firstly distilled water was added, secondly ethanol, and finally distilled water again, each 5 times. A new amount of water or ethanol was added not until the former was sucked off. Every 2 to 3 times the filter cake was stirred. The resulting dry white powder was heated to 550 °C in 6 h, calcined for 12 h at this temperature, and cooled down to room temperature without a temperature program. The yield of this synthesis was about 2.4 g of the final SBA-15.

Because of this low amount and the slight property changes in each batch<sup>1</sup>, the experimental mass was tripled (12.2 g Pluronic P123, 90 ml distilled water, 360 ml HCl, 27 ml TEOS), and the resulting amount of SBA-15 per batch was about 7.5 g.

---

<sup>1</sup>BET surface area and pore size distribution differ (see section 4.1). Furthermore, each batch has different properties in microcalorimetry measurements.

Zhao et al.<sup>[105]</sup> reported for SBA-15 the possibility of tuning pore size and wall thickness, depending on the respective temperature and reaction times. Higher temperatures or longer reaction times result in larger pore sizes and thinner silica walls.

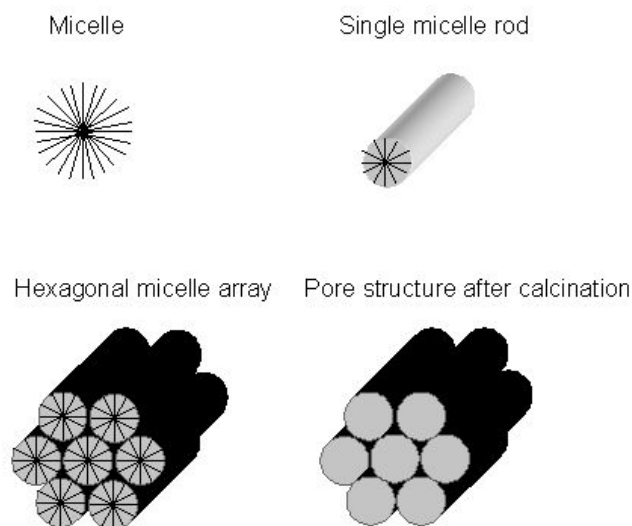


Figure 3.1: Micelle structure for mesoporous silica<sup>[49]</sup>

Figure 3.1 shows a proposed mechanism of micelle rod forming for mesoporous silica materials.<sup>[49]</sup> Micelles are statistical aggregates of surfactant molecules. The surfactant molecules consist of a polar head (hydrophilic) and a non-polar chain (hydrophobic). In water, the hydrophobic chains assemble themselves in a liquid like core and are separated from the surrounding water by a rim of polar heads. In the synthesis of SBA-15, the surfactant Pluronic P123 consisting of poly(ethylene oxide)-poly(propylene oxide)-poly(ethylene oxide) chains ( $\text{EO}_{20}\text{PO}_{70}\text{EO}_{20}$ ) is used. The poly(ethylene oxide) represents the hydrophilic part, while the poly(propylene oxide) part is hydrophobic. Huo et al.<sup>[51]</sup> proposed several pathways for self-assembly reaction of different surfactant and inorganic species (see Figure 3.2). They reported that the mesostructured phases can be synthesized by either direct pathways or mediated pathways, using differently charged surfactant molecules (cationic:  $\text{S}^-$ , anionic:  $\text{S}^+$ ) and inorganic

solution species (cationic:  $I^-$ , anionic:  $I^+$ ) at certain pH conditions. Each surfactant can act as a template for the formation of one or more mesostructures in different reaction conditions. The topology of the composite mesostructures reflects the final geometry, adopted by the organized organic array.

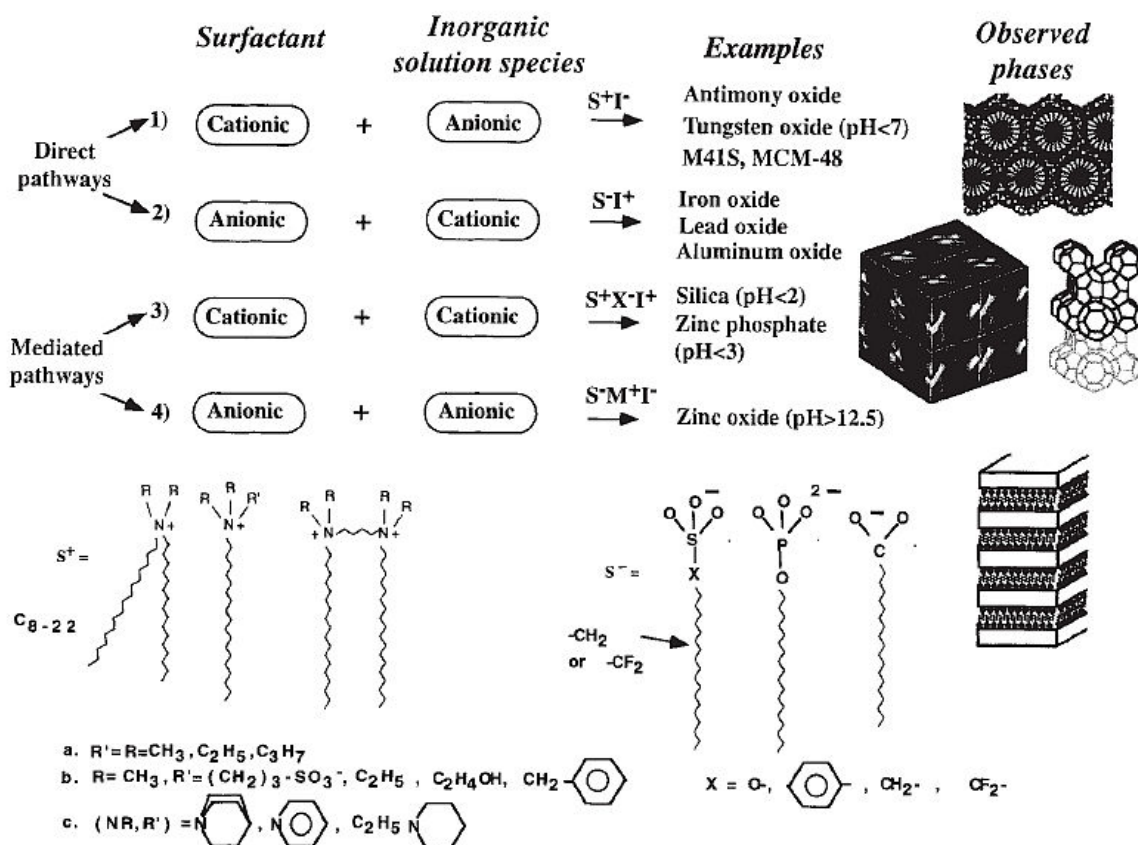
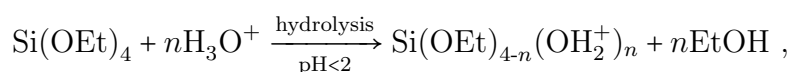
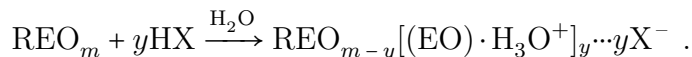


Figure 3.2: General scheme for self-assembly reaction of different surfactant and inorganic species<sup>[51]</sup>

In the literature, it is suggested that the assembly of mesoporous silica organized by non-ionic poly(alkylen oxide) triblock copolymer species like Pluronic P123 in acid media proceeds according to the so-called  $(S^0H^+)(X^-I^+)$  mechanism.<sup>[105]</sup> The first step is the hydrolyzation of the alkoxy silane



which is followed by a partial oligomerization of the silica, and the association of the EO moieties of the surfactant with the hydronium ions in strongly acidic media:



In the present case of Pluronic P123 as surfactant and HCl as acidic media,

R = poly(propylene oxide)

X<sup>-</sup> = Cl<sup>-</sup>.

The charge-associated EO units and the the cationic silica species come together by a combination of electrostatic forces, hydrogen bonding, and van der Waals interactions  $\text{REO}_{m-y}[(\text{EO})\cdot\text{H}_3\text{O}^+]_y \cdots y\text{X}^- \cdots \text{I}^+$  which can be designated as (S<sup>0</sup>H<sup>+</sup>)(X<sup>-</sup>I<sup>+</sup>) mechanism (non-ionic surfactant in acid media plus cationic inorganic solution species).<sup>[105]</sup> The application of triblock copolymer surfactants lead to materials which consist not only of a mesoporous structure but of microstructure as described in section 4.1.1.

## 3.2 Multi-step procedure with functionalization and ion exchange

The standard procedure that was used in this thesis for anchoring transition metal oxides, especially vanadia, on silica was a multi-step procedure developed by Hess et al.<sup>[45]</sup> consisting of an functionalization step, an ion exchange step, and finally, a calcination step. A scheme of this procedure can be seen in Figure 3.4. In detail, in the first step 6.4 ml of 3-aminopropyltrimethoxysilane (APTMS, 97%, Aldrich) was added to a stirred suspension of 2.5 g SBA-15 (Aerosil 300<sup>2</sup>) in 100 ml toluene at 65 °C under reflux. After stirring for 12 h at this temperature, the suspension was filtered and washed with toluene in order to remove all free amine. This procedure was

---

<sup>2</sup>Pretreatment of Aerosil 300 because of difficulties in handling (very fluffy material): Distilled water was added by drops until reaching a complete wetting. The material was dried at room temperature for 16 h and finally ground.



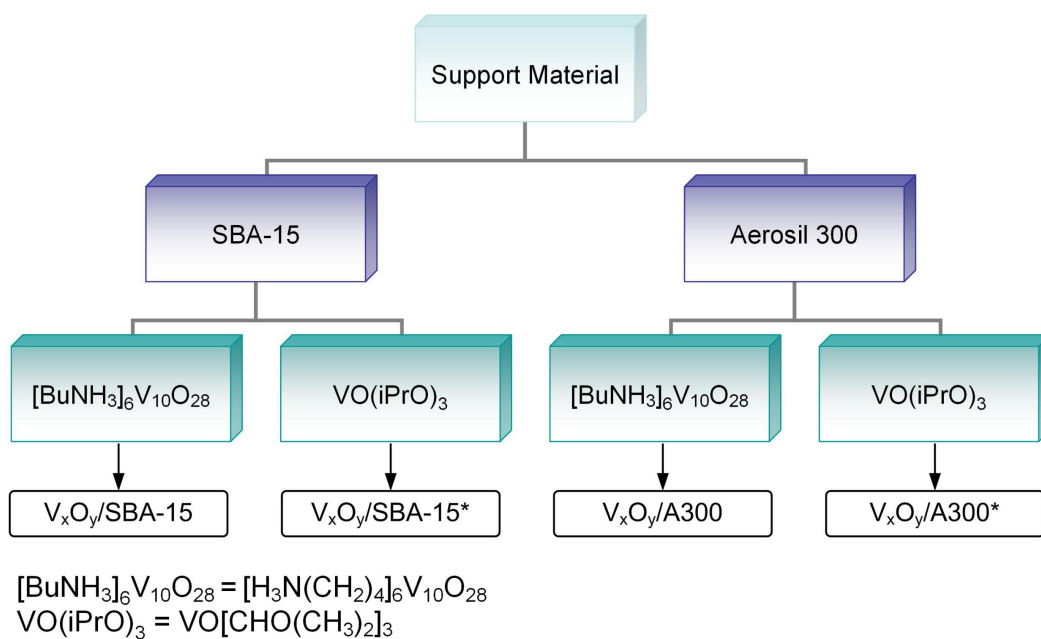


Figure 3.3: Scheme of silica supports and vanadium sources used

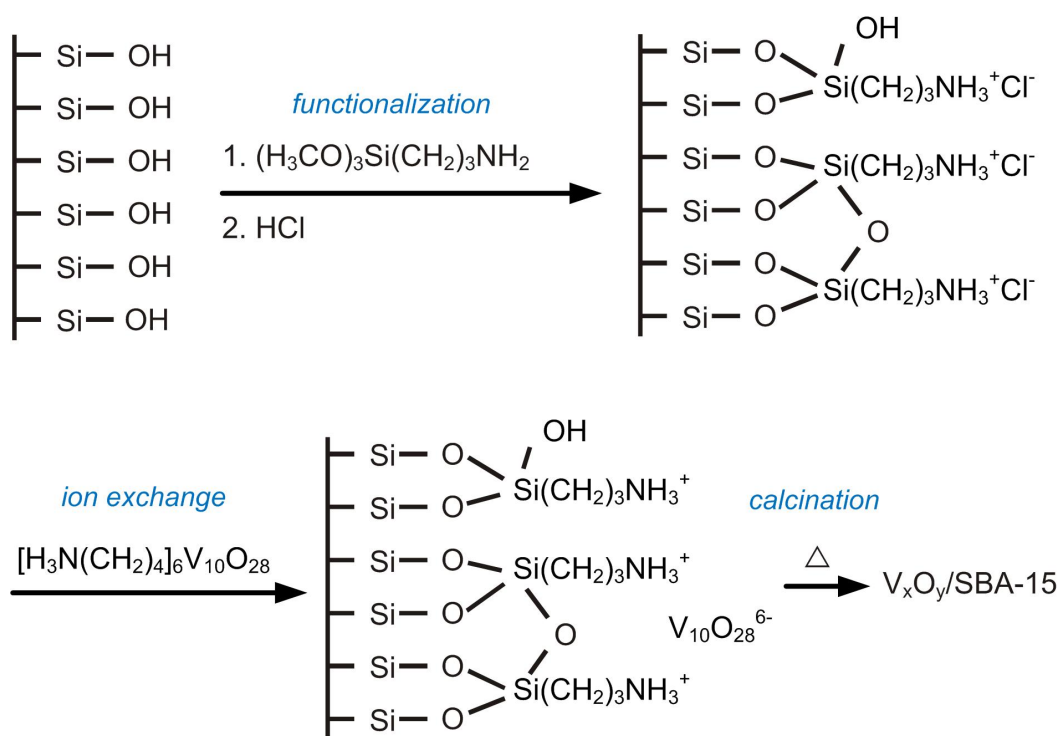


Figure 3.4: Scheme of multi-step procedure

carried out 5 times over a nutsch filter (frit wiht porosity 4) and a vacuum flask. A new amount of toluene was added not until the former was sucked off. Every 2 times the filter cake was stirred. In the second step, the obtained dry powder was stirred in 150 ml of 0.3 molar HCl for 12 h at room temperature. Afterwards, it was filtered and washed with distilled water (same procedure as described above) and dried at 110 °C over night (functionalized material). In the third step, 2 g of the functionalized SBA-15 (Aerosil 300) were stirred in 60 ml distilled water, and 146 mg butylammonium decavanadate ( $[\text{BuNH}_3]_6\text{V}_{10}\text{O}_{28}$ , synthesized according to Roman et al. [81]) were added and stirred for 12 h at room temperature. The resulting yellow content was filtered, washed with distilled water, and finally calcined in air with the same temperature program used for SBA-15 synthesis. The resulting content of vanadium was 2.7 wt% as determined by Inductively Coupled Plasma Optical Emission Spectrometry (ICP-OES, FNE Forschungsinstitut für Nichteisen-Metalle Freiberg GmbH). The samples are named  $\text{V}_x\text{O}_y/\text{SBA-15}$  ( $\text{V}_x\text{O}_y/\text{A300}$ ). The vanadia content can be varied by using different amounts of  $[\text{BuNH}_3]_6\text{V}_{10}\text{O}_{28}$ . The whole procedure was analyzed in detail in former research work by Hess et al. [48].

To explore which properties of the catalyst are directly related to the vanadia, the same procedure was used to produce a modified SBA-15 that underwent the steps explained above except the ion exchange with  $[\text{BuNH}_3]_6\text{V}_{10}\text{O}_{28}$ . The butylammonium decavanadate was replaced by potassium oxalate ( $\text{K}_2\text{C}_2\text{O}_4 \cdot 6\text{H}_2\text{O}$ , Fluka). The amount of oxalate corresponds to the amount of the used vanadium decavanadate. After calcination, the oxalate was gone yielding to a sample of modified SBA-15 or Oxa/SBA-15.

### 3.3 Incipient wetness impregnation

Another method used in this thesis to incorporate vanadia into silica was incipient wetness impregnation of Vanadium (V) triisopropoxide oxide ( $\text{VO}(\text{iPrO})_3$ , 95-99%, Alfa Aesar) according to Gao et al. [33]. For this procedure, the SBA-15 (Aerosil 300)

was dried for 16 h at 110 °C in air. Under argon atmosphere (glove box), 0.147 ml of  $\text{VO}(\text{iPrO})_3$  were mixed with 5 ml isopropanol. In air, this solution was added drop by drop to 1 g of dry SBA-15 (Aerosil 300). After drying over night at room temperature, it was calcined for 12 h at 550 °C in air with the same temperature program as mentioned above. The final content of vanadium was also 2.7 wt%. In the following, the samples resulting from this method are named  $\text{V}_x\text{O}_y/\text{SBA-15}^*$  ( $\text{V}_x\text{O}_y/\text{A300}^*$ ).



# 4 Characterization of silica-supported vanadia catalysts

## 4.1 Physical characterization of silica supports

The silica supports used in our experiments were, firstly, mesoporous *SBA-15* synthesized as described in section 3.1, and secondly, disordered microporous *Aerosil 300* by Evonik Degussa. Characterization was based on the evaluation of nitrogen adsorption-desorption isotherms, TEM, and small angle XRD.

### 4.1.1 SBA-15

A typical N<sub>2</sub> adsorption-desorption isotherm and pore size distribution of a standard SBA-15 sample can be seen in Figure 4.1. The isotherm shows all features typical of well ordered mesoporous materials, as already described in section 2.1.2.

The surface area for the different SBA-15 batches ranges from 680 to 940 m<sup>2</sup>/g depending on the detailed synthesis conditions. Also, the total pore volume and the pore diameter change slightly (see Table 4.1). We can conclude from this that the porous structure in macroscopically view (pore structure, pore size distribution) is similar, but that each batch differs in microscopically view (pore wall structure, roughness) due to the fact that the synthesis mechanism cannot be exactly determined in advance. Several research groups studied the micropores present in the walls of SBA-

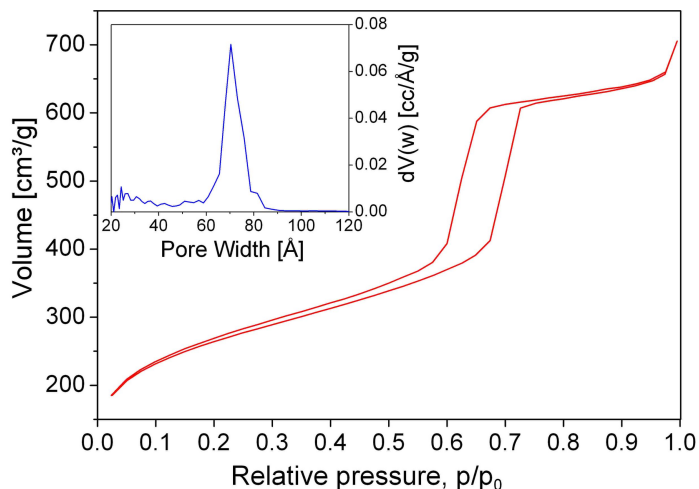


Figure 4.1: Typical  $N_2$  isotherm of SBA-15 with DFT pore size distribution

Table 4.1: BET surface area and pore volume of silica supports used

	$A_{\text{BET}}$ [ $\text{m}^2/\text{g}$ ]	$V_{\text{P}}$ [ $\text{cm}^3/\text{g}$ ]	$d_{\text{P}}$ [nm]
SBA-15	680...940	0.78...1.2	6.6...8.2
Aerosil 300	270...330	-	-

15<sup>[53][32][82][102][89][98]</sup>. On the basis of small angle XRD pattern of SBA-15, Imperor-Clerc et al.<sup>[53]</sup> calculated different models for different variations in the silica densities in the pore walls. The best fitting result was found for a model involving a corona either of uniform density or of linearly increasing density. This model distinguishes a region of dense silica from a microporous region (corona). The corona, an area of lower density, is produced in the uncalcined sample by mixing of the silica species and ethylene oxide segments in the corona region (see Figure 4.2). By contrast, a different picture arises from NMR experiments using pyridine as a sensor for surface defects. Shenderovich et al.<sup>[87]</sup> have demonstrated that surface defects of SBA-15 result in a certain degree of roughness of the pore walls. Until now, details of SBA-15 structure are still not fully understood.

The shape of a SBA-15 particles and the hexagonal pore structure can be clearly seen in Figure 4.4 and 4.5. The particles in the SEM image are approximately 5 - 7  $\mu\text{m}$  long and have a diameter of 4 - 6  $\mu\text{m}$ . The TEM image shows a cross as well as a

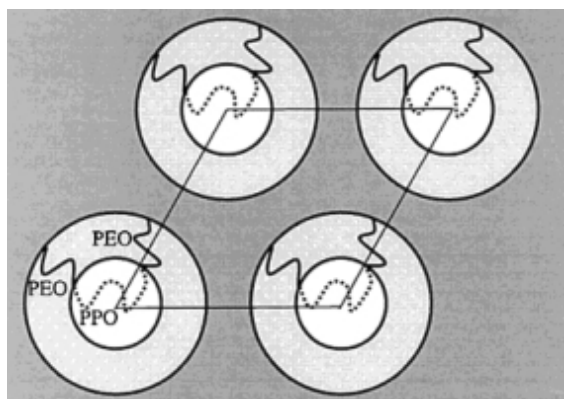


Figure 4.2: Schematic representation of the organization of uncalcined SBA-15 materials [53]

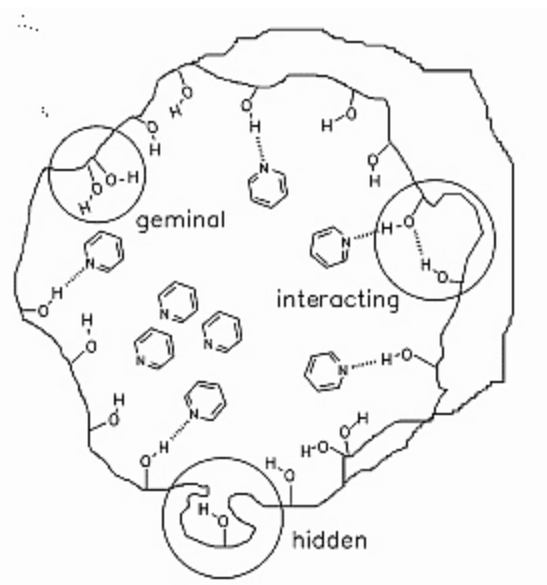


Figure 4.3: Pore model exhibiting a rough inner surface of mesoporous silica powders (schematically) hosting pyridine- $^{15}\text{N}$  [87]

longitudinal sectional view. From evaluating the TEM images, a pore wall thickness of 3 - 4 nm and a pore diameter of about 5 nm can be estimated.

For further characterization, small-angle XRD is highly useful (see section 2.2). Typically, intensities for a  $p6mm$  hexagonal symmetry occur for planes with Miller indices (100), (110), (200) and (210). [104] In Figure 4.6, the three well-resolved peaks can be indexed as (100), (110) and (200). The inset magnifies the peaks at planes with Miller indices (110) and (200). The fitting of the peaks results in unit cell parameters (referred to  $a$ ) of 99 to 113 Å and corresponding lattice plane spacing of 86 to 98 Å. With help of the value of the wall thickness deduced from TEM images, the pore diameter can be calculated and yields values of 5.9 to 8.3 nm. These are in agreement with the values of the pore diameters evaluated by adsorption-desorption of  $\text{N}_2$ .

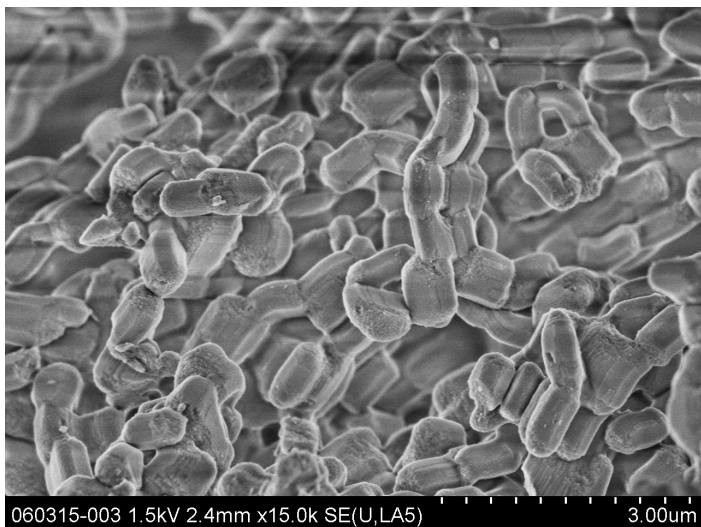


Figure 4.4: SEM image of SBA-15 particles

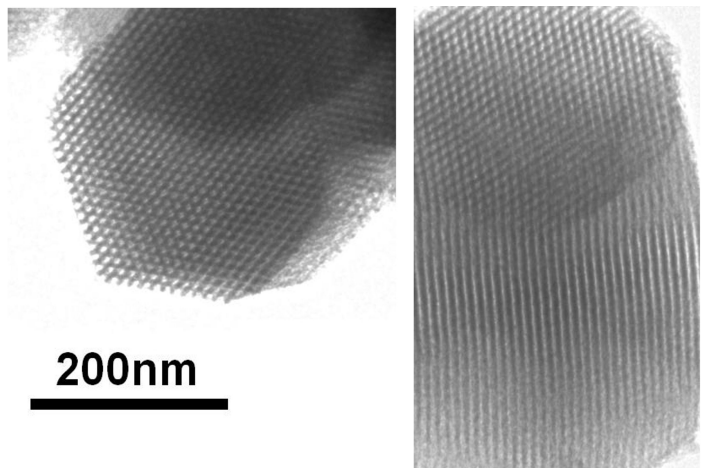


Figure 4.5: TEM images of SBA-15 in cross sectional view (left) and longitudinal sectional view (right)

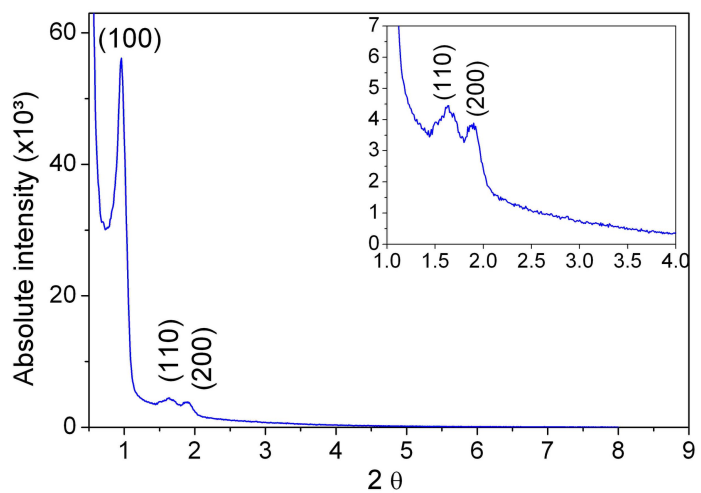


Figure 4.6: Small-angle XRD of SBA-15 with magnification inset



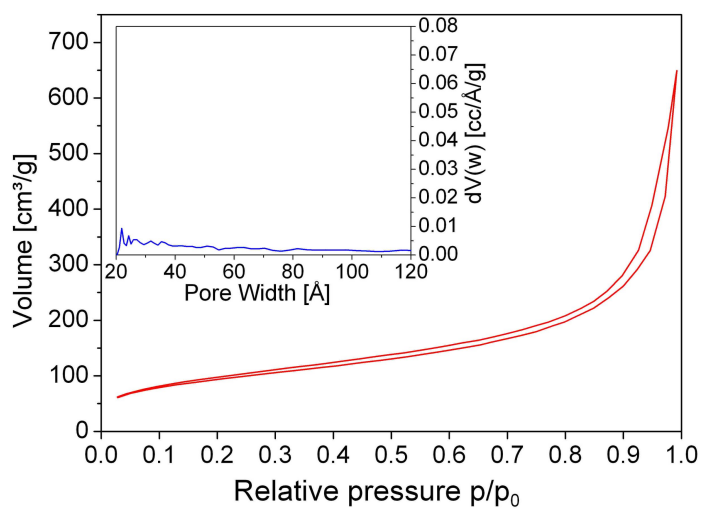


Figure 4.7: N<sub>2</sub> isotherm of Aerosil 300 with DFT pore size distribution

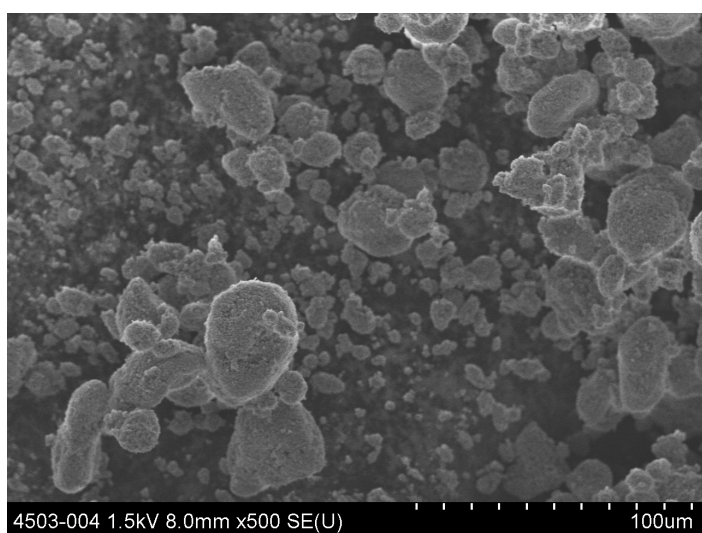


Figure 4.8: SEM image of Aerosil 300 particles

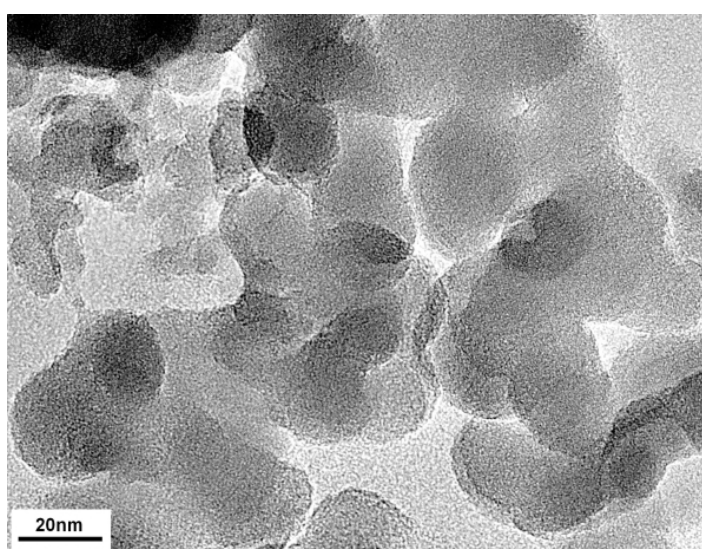


Figure 4.9: TEM images of Aerosil 300

### 4.1.2 Aerosil 300

Figure 4.7 shows the nitrogen adsorption-desorption isotherm of Aerosil 300. This amorphous silica, produced by Evonik Degussa, neither gives an indication for an ordered pore structure in its isotherm shape nor a clearly defined pore size distribution. This isotherm shape is typical of agglomerates of flat particles which result in the occurrence of slit pores (see section 2.1.2). The BET surface area is 300 ( $\pm 30$ ) m<sup>2</sup>/g and the average primary particle size is 7 nm (Evonik).

In Figure 4.8 a typical SEM image of agglomerates of Aerosil 300 is shown. The amorphous structure can be seen in the TEM image in Figure 4.9.

## 4.2 Mechanical, thermal, and hydrothermal stability

Catalysis is often done under aggressive conditions as high temperatures and pressures. Especially for the partial oxidation of propane / propene steam is added during the reaction in order to reach a high selectivity of acrylic acid. Furthermore in industry, pellets are necessary. Industrial conditions for making pellets are in the pressure range of 10 - 400 MPa<sup>[10]</sup> which is already critical for the pore structure of mesoporous material. For this reason we tested the mechanical, thermal and hydrothermal stability of the vanadia-supported SBA-15 samples.

The mechanical stability of blank SBA-15 and V<sub>x</sub>O<sub>y</sub>/SBA-15, synthesized according to the multi-step procedure explained in section 3.2 and incipient wetness impregnation (see section 3.3), was tested and characterized in detail. Blank and modified SBA-15 were tested for thermal and hydrothermal stability. Characterization concerning the pore structure was based on the evaluation of nitrogen adsorption-desorption isotherms, small-angle XRD data, and TEM images. The former two, as integral methods, are known as powerful tools helping to characterize structural changes in mesoporous silica like SBA-15.<sup>[26]</sup> TEM images always show local spots of a sample and are helpful by visualization. Regarding changes of the vanadia species, Raman-

and DRUV-vis spectroscopy was employed.

### 4.2.1 Mechanical stability

Mechanical stability was tested by compressing 100 mg of the tested samples into pellets measuring 13 mm in diameter. The pressure was increased to 750 MPa for a duration of 3 s. Afterwards, the pellets were ground again for characterization. Table 4.2 shows the BET surface area and the pore volume before and after pressure treatment. The pore size distribution was not determined because the calculation models are designed for regular (cylindrical) pores and are not an accurate means for evaluating irregular pore structures.

Figure 4.10 shows the N<sub>2</sub> adsorption-desorption isotherms of blank SBA-15 after

Table 4.2: BET surface area and pore volume of blank SBA-15 and V<sub>x</sub>O<sub>y</sub>/SBA-15 after mechanical treatment

	mech. treatment [MPa]	A <sub>BET</sub> [m <sup>2</sup> /g]	V <sub>p</sub> [cm <sup>3</sup> /g]
SBA-15	0	928	1.1
	75	770	0.94
	188	759	0.89
	376	810	0.86
	752	667	0.61
V <sub>x</sub> O <sub>y</sub> /SBA-15	0	533	0.68
	75	531	0.65
	188	531	0.65
	376	505	0.65
	752	416	0.45

pressure treatment of (a) 0 MPa, (b) 75 MPa, (c) 188 MPa, (d) 376 MPa and (e) 752 MPa. The isotherms are continuously shifting to lower volumes, which indicates

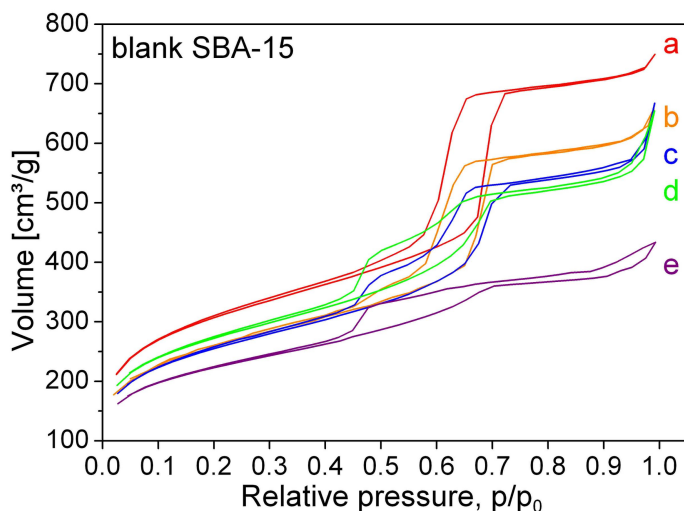


Figure 4.10:  $N_2$  Isotherms of blank SBA-15 after mechanical treatment at (a) 0 MPa, (b) 75 MPa, (c) 188 MPa, (d) 376 MPa, and (e) 752 MPa

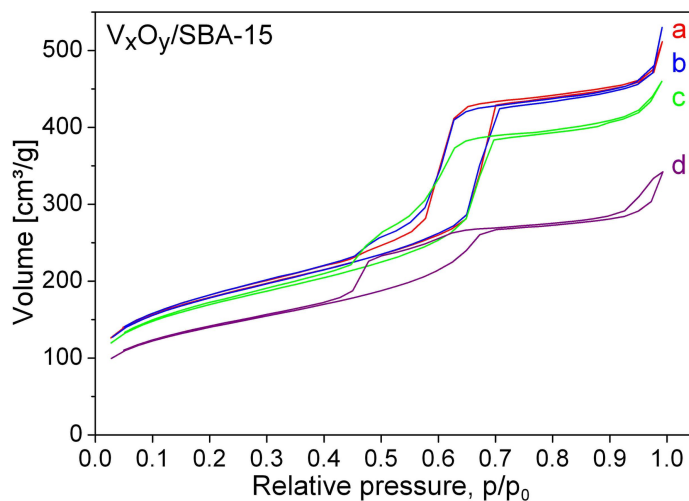


Figure 4.11:  $N_2$  Isotherms of  $V_xO_y/SBA-15$  after mechanical treatment at (a) 0 MPa, (b) 188 MPa, (c) 376 MPa, and (d) 752 MPa

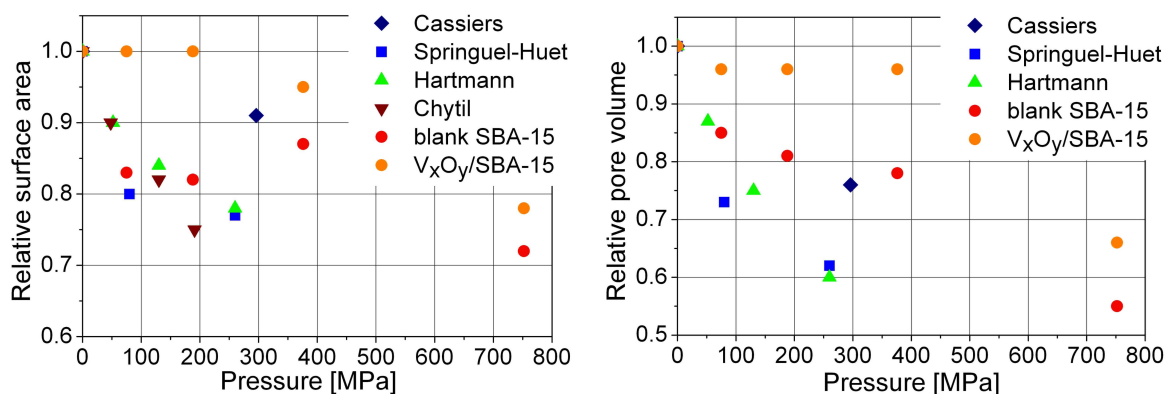


Figure 4.12: Comparison of data from this work after pressure treatment with literature data of Cassiers et al.<sup>[20]</sup>, Springuel-Huet et al.<sup>[91]</sup>, Hartman et al.<sup>[41]</sup>, and Chytil et al.<sup>[26]</sup>

a decrease of the BET surface area and the pore volume. The typical hysteresis loop for well ordered mesoporous materials (type H1) keeps its shape up to a pressure of 376 MPa. At 752 MPa, the shape deforms to a combination of type H2 and H4 hysteresis. Type H2 results from a disordered materials in which the distribution of pore size and shape is not precisely defined, whereas materials with type H4 hysteresis are often associated with narrow slit pores (see section 2.1.2). In other words, the uniform hexagonal channels of the SBA-15 are pressed together and the well-ordered mesoporous structure is destroyed. These results are in good agreement with literature data on blank SBA-15, as can be seen in Figure 4.12. [91] [20] [41]

The decrease of the structural order can also be seen in small-angle XRD (see Figure 4.13). The typical pattern of the two dimensional hexagonal structure ( $p6mm$ ) of SBA-15 shows reflections at (100), (110), and (200) ((110) and (200) are magnified in the inset). The patterns were normalized to the (100) reflection and show a decrease in intensity with increasing pressure. For the sample pressed with 752 MPa all reflections disappear; only the (100) reflection is discernible in the figure. These results about the loss of structure nicely confirm the observations already stated with regard to the N<sub>2</sub> adsorption-desorption isotherm.

In contrast to the blank SBA-15, the N<sub>2</sub> adsorption-desorption isotherms of V<sub>x</sub>O<sub>y</sub>/SBA - 15 (multi-step procedure) treated the same way (Figure 4.11), do not show a significant change of the N<sub>2</sub> adsorption-desorption isotherm, and consequently of the BET surface area and the pore volume until pressures of 152 MPa. The shape of the hysteresis loop starts deforming at 376 MPa but is still acceptable at 752 MPa. This means that there are still well-defined pores. This behavior is again confirmed by the XRD patterns (see Figure 4.14). The normalized patterns show less intensity with increasing pressure, however, the three main features are always present. The different degree of structural loss for blank SBA-15 and V<sub>x</sub>O<sub>y</sub>/SBA-15 can also be seen in the TEM images in Figures 4.16 (b) and (c).

One effect of the multi-step procedure is a decrease of the BET surface area of up to 50% in comparison to blank SBA-15. Samples synthesized using incipient wetness

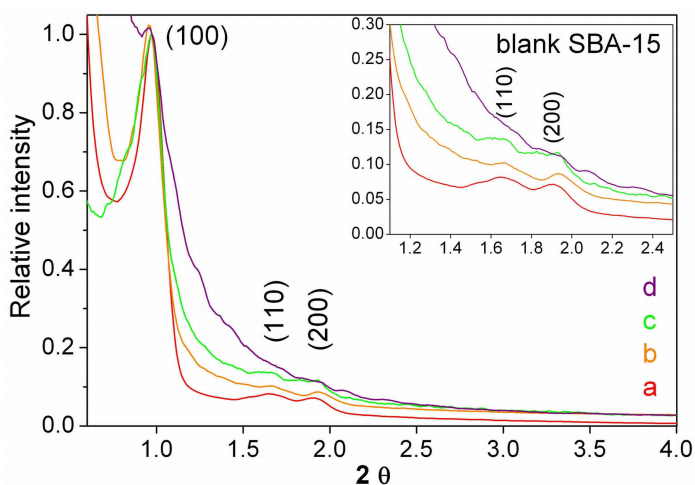


Figure 4.13: Small-angle XRD of blank SBA-15 after mechanical treatment at (a) 0 MPa, (b) 75 MPa, (c) 376 MPa, and (d) 752 MPa

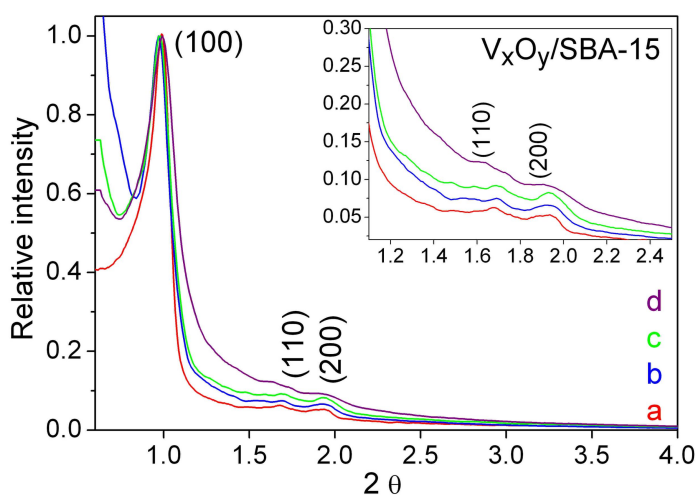


Figure 4.14: small-angle XRD of  $V_xO_y/SBA-15$  after mechanical treatment at (a) 0 MPa, (b) 188 MPa, (c) 376 MPa, and (d) 752 MPa

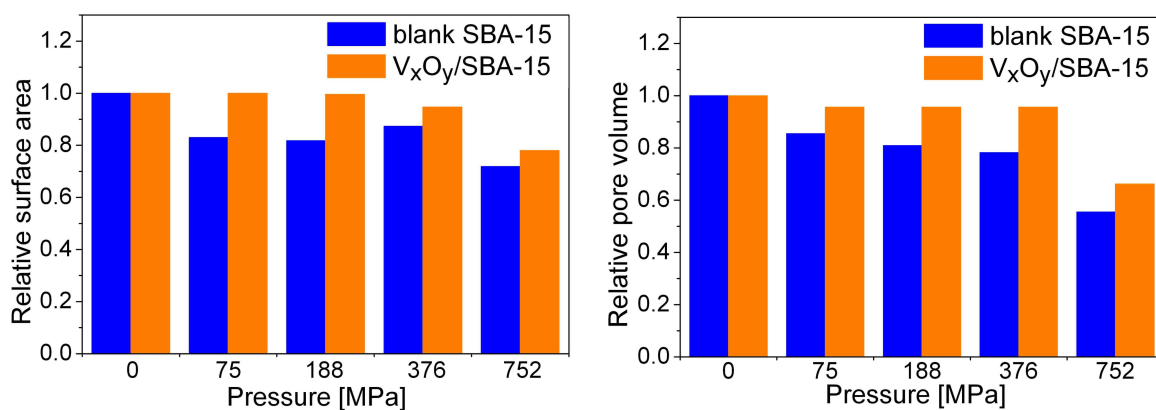


Figure 4.15: Relative surface area and pore volume after mechanical treatment of blank SBA-15 and  $V_xO_y/SBA-15$

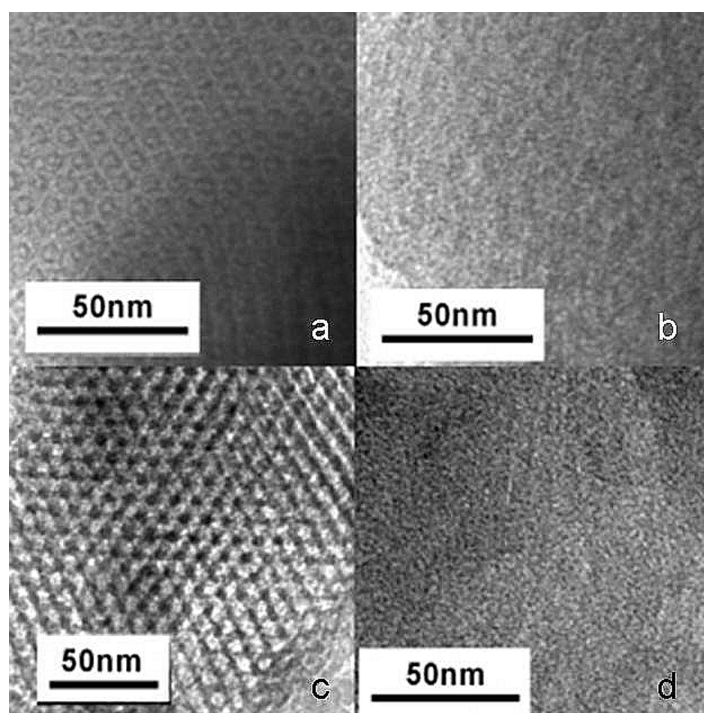


Figure 4.16: TEM picture after mechanical treatment of (a) blank SBA-15 at 0 MPa, (b) blank SBA-15 at 752 MPa, (c)  $V_xO_y$ /SBA-15 at 752 MPa, and (d)  $V_xO_y$ /SBA-15\* at 752 MPa

impregnation show a decrease of only 25%. The larger impact of the multi-step procedure on surface area seems to correlate with the increased stability. To show the changes in surface area and pore volume, after different treatments more clearly, Figure 4.15 depicts the corresponding relative values (related to the parent samples) for blank SBA-15 and  $V_xO_y$ /SBA-15. Obviously, the relative decrease of the BET area and the pore volume for blank SBA-15 is higher compared to that of  $V_xO_y$ /SBA-15. This observation combined with the results from small-angle XRD and TEM clearly point to a higher degree of mechanical stability of the modified material.

In order to unravel the origin of this higher mechanical stability, we first took data for blank SBA-15 mixed with the corresponding amount (2.7 wt% V) of powder  $V_2O_5$  as well as for a sample of  $V_xO_y$ /SBA-15\* synthesized using incipient wetness impregnation under the same conditions. In both cases match those of blank SBA-15 (Figure 4.17). However, the sample resulting from the multi-step procedure using potassium oxalate (Oxa/SBA-15) instead of decavanadate shows a pressure resistance closely matching that of  $V_xO_y$ /SBA-15. This strongly suggests that the reason for the ob-

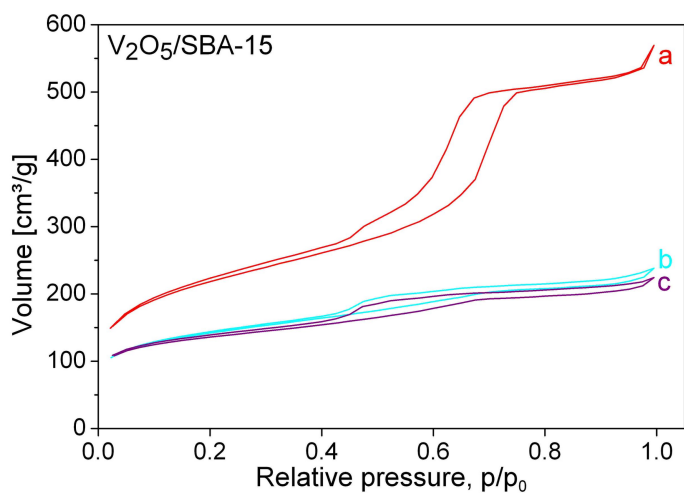


Figure 4.17:  $N_2$  isotherms after mechanical treatment of (a) blank SBA-15 0 MPa, (b)  $V_2O_5/SBA-15$  at 752 MPa and (c)  $V_xO_y/SBA-15^*$  at 752 MPa

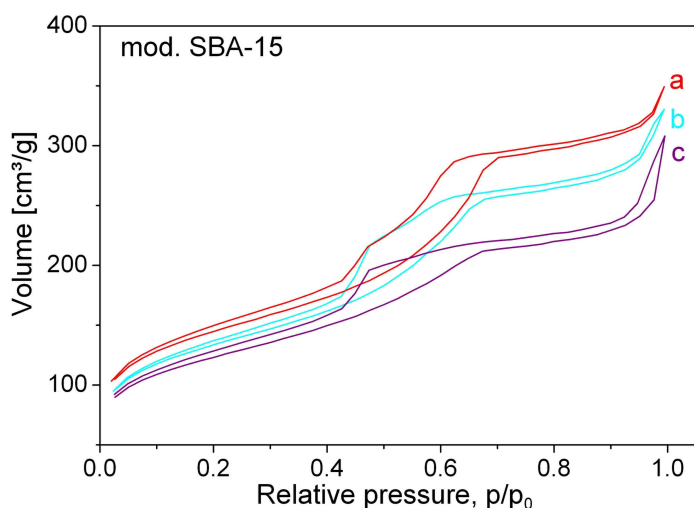


Figure 4.18:  $N_2$  isotherms after mechanical treatment of (a)  $V_xO_y/SBA-15$  at 0 MPa, (b) Oxa/SBA-15 at 752 MPa and (c)  $V_xO_y/SBA-15$  at 752 MPa

served increase in the mechanical stability results from the synthesizing procedure. Investigation of the individual steps of the multi-step procedure demonstrates that the decisive step leading to an increased stability is the functionalization with APTMS. This is also the step in which the BET surface area decreases. One explanation for this behavior could be that the rough surface of SBA-15 (see Figure 4.3 in section 4.1.1) is smoothed during the grafting of APTMS resulting in a higher density of the corona.

In literature, a proposed mechanism for SBA-15 damage at high pressures is based on an opening of rings containing  $SiO_4$  units through a cleavage of the Si-O-Si bonds. At pressures higher than 112 MPa this process is assumed to be accompanied by a rupture



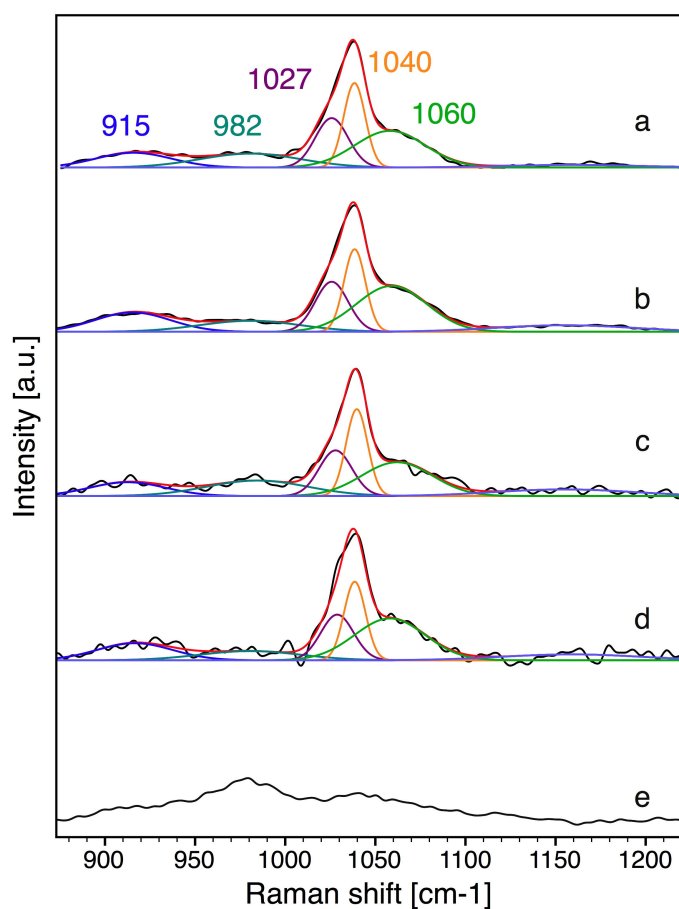


Figure 4.19: Raman spectra before pressure treatment of (a)  $V_xO_y/SBA-15$ , (c)  $V_xO_y/SBA-15^*$  and after pressure treatment at 752 MPa, (b)  $V_xO_y/SBA-15$ , (d)  $V_xO_y/SBA-15^*$  and (e) blank SBA-15

of the 3-membered siloxane rings.<sup>[26]</sup> An explanation could be that the grafting with APTMS seems to prevent this process.

### Raman spectroscopy

Spectroscopic analysis of the supported surface vanadia species before and after pressure treatment was done using Raman and DRUV-vis spectroscopy. The Raman spectra are shown in Figure 4.19. The intensities are normalized to the intensity of the band at  $1040\text{ cm}^{-1}$  and fitted in the range of  $860$  to  $1210\text{ cm}^{-1}$  with 5 curves. Intensities are found at  $915 \pm 3\text{ cm}^{-1}$ ,  $982 \pm 3\text{ cm}^{-1}$ ,  $1027 \pm 2\text{ cm}^{-1}$ ,  $1040 \pm 1\text{ cm}^{-1}$  and  $1060 \pm 3\text{ cm}^{-1}$ . Referring to theoretical calculation by Magg et al.<sup>[70]</sup>, these bands can be assigned to out-of-phase ( $915\text{ cm}^{-1}$ ) and in-phase ( $1060\text{ cm}^{-1}$ ) Si-V-O interface

stretching vibrations. The band at  $982\text{ cm}^{-1}$  was assigned to free Si-OH stretches.<sup>[15]</sup> In the literature the band at  $1040\text{ cm}^{-1}$  is assigned to vanadyl stretches.<sup>[86][84][68]</sup> It is obviously that the peak has several components, which were not yet analyzed in literature. We assigned the V=O stretches at  $1027\text{ cm}^{-1}$  to vanadia clusters of a low degree of polymerization and the one at  $1040\text{ cm}^{-1}$  to vanadia clusters of a relatively higher degree of polymerization. The ratio was determined in order to compare the polymerization degree of the four samples. Neither before, nor after pressure treatment could there be detected differences concerning the vanadyl stretches.

### **DRUV-vis spectroscopy**

After pressure treatment, the DRUV-vis spectra (Figure 4.20 and 4.21) of the multi-step sample and the incipient wetness impregnated sample both show an increased overall intensity. The multi-step sample shows a broadening to higher wavelengths, whereas the position of the maximum intensity is still observed around 262 nm. The mechanical treated impregnated sample, however, shows a shift in intensity to lower wavelength (from 271 to 262 nm) and a broadening as well.

Absorption in the DRUV-vis spectrum of metal oxides is due to charge transfer (CT) between oxygen and the metal, in our case vanadium. The CT bands are strongly influenced by the number of ligands surrounding the central vanadium ion, which provides information on the coordination of the vanadium. A shift to higher wavelengths is interpreted in literature as an increase of the concentration of the oligomeric structure.<sup>[84][4][8]</sup> Concerning tetrahedrally coordinate vanadia, low-intensive absorption bands ( $d-d$  transitions) higher than 335 nm can be assigned to partially reduced vanadium forms ( $V^{3+}/V^{4+}$ ) and smaller wavelength to the oxidized vanadium form ( $V^{5+}$ ). The excitation of oxidized vanadium leads to electron transitions that are energetically close to each other. As a result, DRUV-vis absorption bands tend to overlap.<sup>[7]</sup>

Avdeev et al.<sup>[7]</sup> calculated electronic spectra for monomeric and dimeric vanadia ( $V^{5+}$ )

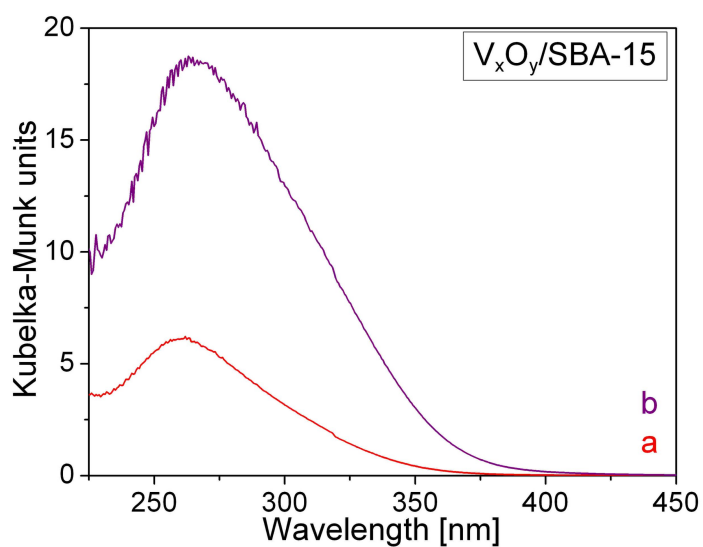


Figure 4.20: DRUV-vis spectrum of  $V_xO_y/SBA-15$  (a) before pressure treatment and (b) after pressure treatment at 752 MPa

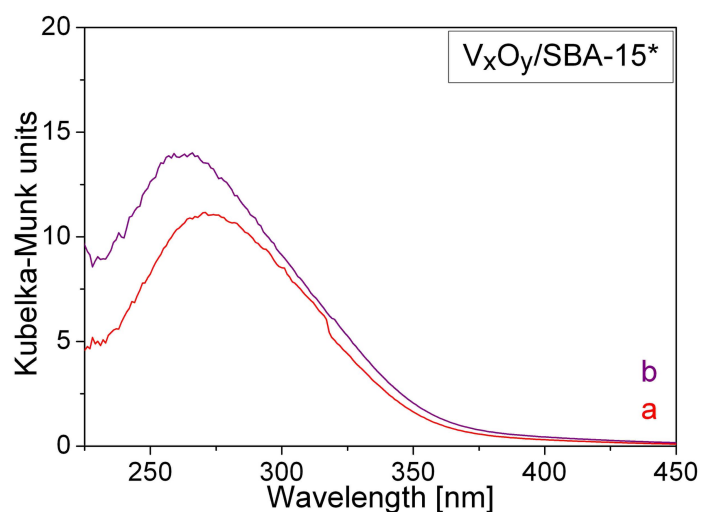


Figure 4.21: DRUV-vis spectrum of  $V_xO_y/SBA-15^*$  (a) before pressure treatment and (b) after pressure treatment at 752 MPa

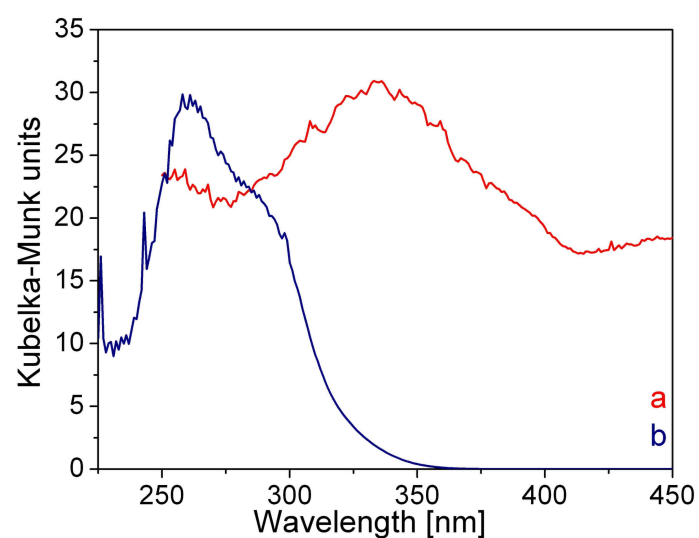


Figure 4.22: DRUV-vis spectra of (a)  $V_2O_5$  and (b)  $NH_4VO_3$

on SiO<sub>2</sub>. The bands showing the highest intensity in case of monomeric species appear at wavelengths smaller than 200 nm, which we were not able to measure with our spectrometer. For the dimeric species the bands with the highest intensities appear between 200 and 250 nm. Within this region Avdeev et al.<sup>[7]</sup> assign a band at a calculated wavelength of 240 nm which corresponds to the transition of  $\pi(\text{O} - \text{Si} - \text{O}) \rightarrow 3d_{\delta}(\text{V})$  type. Transitions between 260 and 300 nm are assigned to charge transfer from the interface atoms of oxygen onto vanadium:  $\pi(\text{V} - \text{O} - \text{Si}) \rightarrow 3d_{\delta}(\text{V})$  including terminal oxygen atoms [ $\pi(\text{V} = \text{O}) + \pi(\text{V} - \text{OH})$ ].

Our own reference measurements of V<sub>2</sub>O<sub>5</sub> (99.5%, Riedel-de Haen) and NH<sub>4</sub>VO<sub>3</sub> (99.9%, Aldrich) are shown in Figure 4.22. NH<sub>4</sub>VO<sub>3</sub> shows an intensity at 285 nm and a broad tail between 350 and 500 nm, whereas V<sub>2</sub>O<sub>5</sub> shows a broad intensity at 335 and at 450 nm. Crystalline ammonium metavanadate contains infinitely long chains of corner-sharing VO<sub>4</sub> tetrahedra, whereas crystalline vanadium pentoxide is octahedral coordinated. With these results, the broadening to higher wavelength in the spectrum of the multi-step sample can be assigned to an increase of the degree of oligomeric species. The intensity at wavelengths higher than 300 nm could be assigned to very long chains as described in for NH<sub>4</sub>VO<sub>3</sub>. The presence of V<sub>2</sub>O<sub>5</sub> can be excluded because we found no signal in the Raman spectrum or SEM images. Similar conclusion can be made for the features at higher wavelengths of the impregnated sample. The shift to lower wavelengths can be explained by a splitting of vanadia chains to species with a lower degree of polymerization due to destruction of the mesoporous pore structure of the SBA-15.

### 4.2.2 Thermal stability

Thermal stability was tested for blank and modified SBA-15 (Oxalate/SBA-15), because it could be shown that the increased stability is not related to the incorporated vanadia. It is created by the treatment with APTMS in the multi-step procedure. The thermal stability was tested by heating the samples in air with 5 °C/min to 650,

750, 850 and 1000 °C and treated for 24 h at these temperatures, respectively.

Table 4.3 shows the values of the BET surface area and pore volume for blank SBA-15 and modified SBA-15 after thermal treatment at temperatures up to 1000 °C for 24 h. It can be seen that the BET surface area as well as the pore volume decreases with increasing temperatures for both samples.

This is also visible in the nitrogen isotherms in Figure 4.23 (blank SBA-15) and Figure

Table 4.3: BET surface area and pore volume of blank SBA-15 and modified SBA-15 after thermal treatment

	thermal treatment	$A_{\text{BET}}[\text{m}^2/\text{g}]$	$V_p[\text{cm}^3/\text{g}]$
SBA-15	calcined	701	0.86
	24h, 650 °C	468	0.68
	24h, 750 °C	354	0.52
	24h, 850 °C	228	0.35
	24h, 1000 °C	58.4	0.058
mod. SBA-15	calcined	492	0.63
	24h, 650 °C	411	0.55
	24h, 750 °C	294	0.44
	24h, 850 °C	213	0.32
	24h, 1000 °C	8.09	0.016

4.24 (modified SBA-15). The isotherms in both figures shift to lower adsorbed volumes ( $\Rightarrow$  lower surface area) with an increase of temperature. After thermal treatment at 1000 °C the hysteresis loop is collapsed and indicates the damage of the mesoporous structure of the material.

The relative values for both properties are shown in Figure 4.25. A dramatic loss of surface area and pore volume at 1000 °C is found for both samples. At this temperature the structure collapses completely and, as a consequence, values smaller than 10% compared to the original samples are obtained. The surface area for blank SBA-15

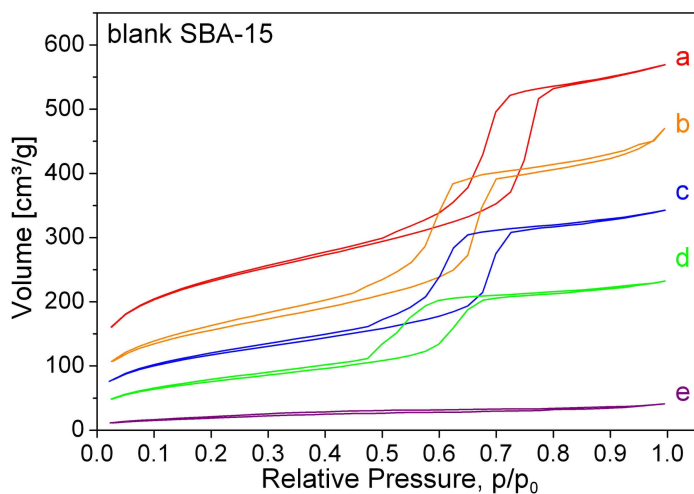


Figure 4.23: N<sub>2</sub> isotherm of blank SBA-15 after thermal treatment at (a) 550 °C, (b) 650 °C, (c) 750 °C, (d) 850 °C, and (e) 1000 °C

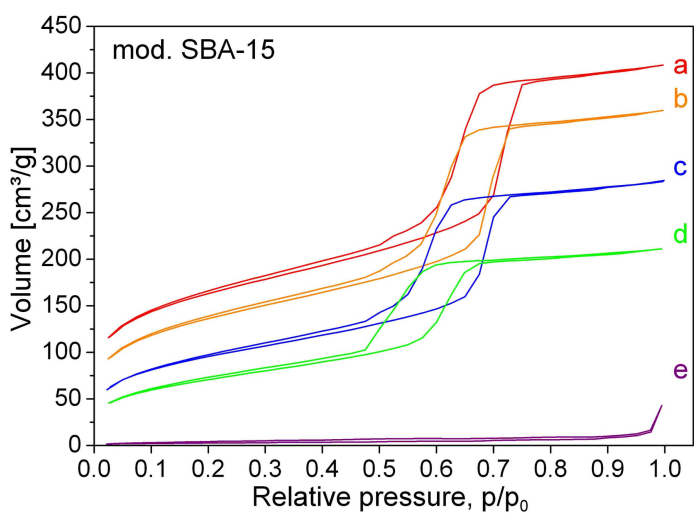


Figure 4.24: N<sub>2</sub> isotherm of modified SBA-15 after thermal treatment at (a) 550 °C, (b) 650 °C, (c) 750 °C, (d) 850 °C, and (e) 1000 °C

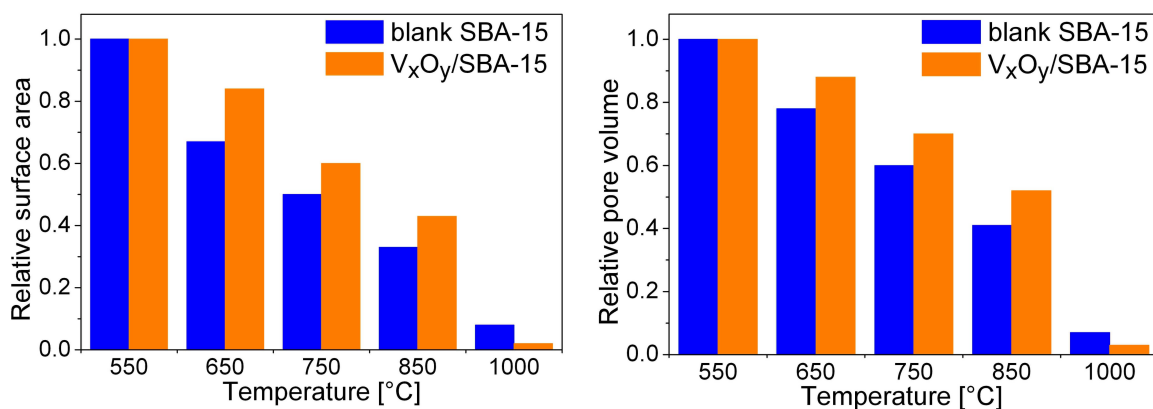


Figure 4.25: Relative surface area and pore volume of blank SBA-15 and modified SBA-15 after thermal treatment

shrinks to 67% at 650 °C and 50% at 750 °C whereas the surface area for modified SBA-15 is reduced to 84% and 60%, respectively. Similar observations were made for the pore volume. At 650 °C, the pore volume is 88% of its original value in the case of modified SBA-15 and 78% in the case of blank SBA-15. Cassiers et al.<sup>[20]</sup>, who looked at the thermal stability of surfactant assembled mesoporous silicas, observed a lower decrease of surface area (88% at 650 °C, 71% at 750 °C) and pore volume (89% at 650 °C, 76% at 750 °C) for blank SBA-15 at the same temperatures. However, in their investigations the final temperature was only kept for 8 h. This leads to the conclusion that the duration of keeping the material at the final temperature has an influence on the decrease of surface area and pore volume.

### 4.2.3 Hydrothermal stability

Hydrothermal stability was tested by heating 100 mg of each sample with 500  $\mu$ l water in an autoclave (wall material Teflon) with a volume of 41 ml.

Several authors<sup>[20][103][38]</sup> have examined the hydrothermal stability of SBA-15, but comparisons are difficult because of the different conditions. The aim of this study was to evaluate potential benefits of the modification of SBA-15 compared to blank SBA-15. BET surface areas and pore volume data before and after hydrothermal treatment of blank and modified SBA-15 are shown in Table 4.4. In hydrothermal treatment, again, modified SBA-15 is more stable than blank SBA-15. The N<sub>2</sub> adsorption-desorption isotherms in Figure 4.26 and 4.27 show a shift to lower volumes for both samples, but in case of blank SBA-15 the shift is significantly larger than for the modified sample. The shape of the hysteresis loop remains unchanged in the two samples. This means that, while the pore structure is still intact, the surface area of blank SBA-15 shrinks to 71% of its original value and that of modified SBA-15 to 76%. In contrast to that, the pore volume of the modified sample after hydrothermal treatment is retained at 99%, that is nearly the same as before the treatment (see Figure 4.28). A possible explanation could be that the surface roughness, as de-

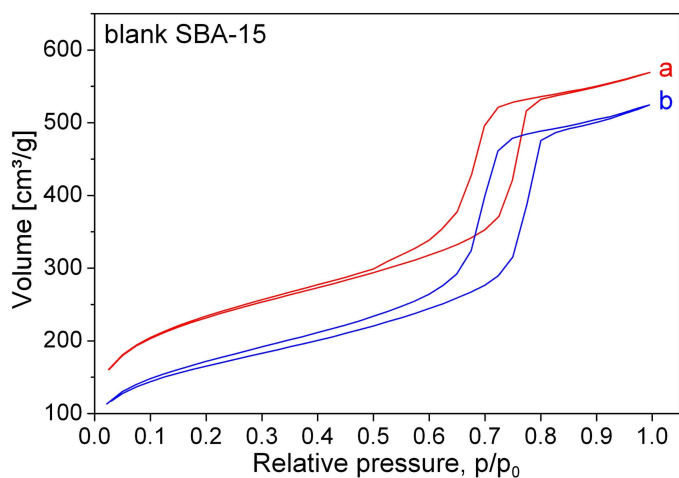


Figure 4.26: N<sub>2</sub> isotherm of blank SBA-15 (a) before and (b) after hydrothermal treatment

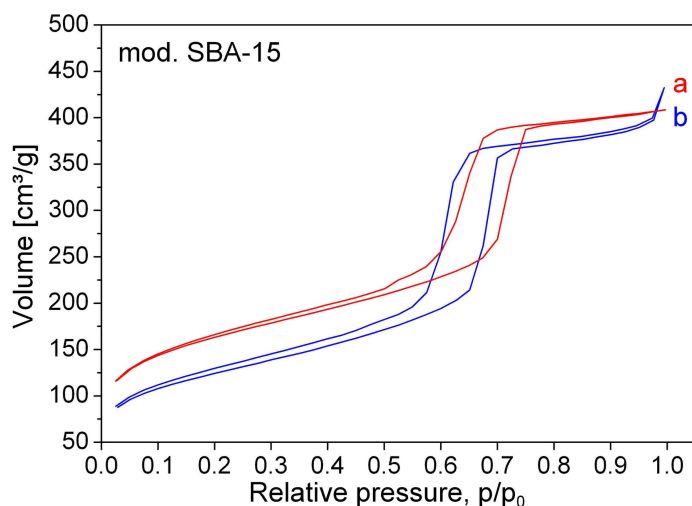


Figure 4.27: N<sub>2</sub> isotherm of modified SBA-15 (a) before and (b) after hydrothermal treatment

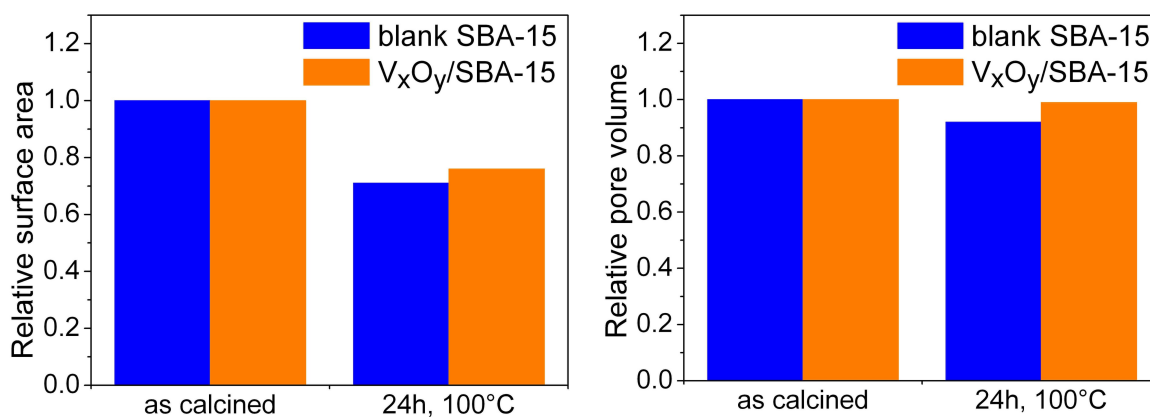


Figure 4.28: Relative surface area and pore volume after hydrothermal treatment



Table 4.4: BET surface area and pore volume of blank SBA-15 and modified SBA-15 after hydrothermal treatment

	hydrothermal	$A_{\text{BET}}[\text{m}^2/\text{g}]$	$V_{\text{p}}[\text{cm}^3/\text{g}]$
	treatment		
SBA-15	calcined	701	0.86
	24h, 100 °C	498	0.79
mod. SBA-15	calcined	492	0.63
	24h, 100 °C	370	0.62

scribed by Shenderovich<sup>[87]</sup>, is smoothed but that this process has no influence on the macroscopic pore structure.

#### 4.2.4 Conclusion

Investigation on the mechanical, thermal, and hydrothermal stability of blank SBA-15,  $V_xO_y/\text{SBA-15}$ , and  $V_xO_y/\text{SBA-15}^*$  showed a significant increase of the stability for all treatments for the samples synthesized according to the multi-step procedure. This effect of stabilization is ascribed to the grafting of the APTMS to the surface of SBA-15. Raman spectroscopy has not shown any differences after mechanical treatment. DRUV-vis spectra for the same treatment indicate a higher degree of polymerization for the pressed samples. This effect is stronger for the incipient wetness impregnated sample than for the multi-step sample. The damage of the mesoporous structure seems to lead to an increase of the degree of polymerization.

## 4.3 Comparison of silica supports and synthesis methods

Supported vanadia catalysts were synthesized using two differently structured silica materials and with two different preparation methods. The properties of the support materials used, namely SBA-15 and Aerosil 300, were described in section 4.1. As synthesis methods a multi-step procedure including grafting and ion exchange and incipient wetness impregnation were applied. These are described in section 3.2 and 3.3. The vanadium content in all samples was designed to obtain an atom density of 0.7 V-atoms/nm<sup>2</sup>.

### 4.3.1 Physical characterization

The nitrogen adsorption-desorption isotherms for SBA-15 supported vanadia samples in Figure 4.29 show a shift to lower volumes. The following order can be deduced:

blank SBA-15 → incipient wetness impregnated sample → multi-step sample.

Hence, the surface area decreases to 80% for the incipient wetness impregnated sample, and to 60% for the multi-step sample compared to SBA-15. With regard to pore volumes, we noted values of 90% and 70%, respectively. Investigations of the individual steps of the multi-step procedure led to the observation that the surface area already shrinks in the first step, that is when APTMS is grafted to SBA-15.

The pore size distribution slightly shifted to smaller values for the vanadia samples, as well. But in both samples the main emphasis was found at 7.0 nm (blank SBA-15 7.3 nm). The only difference is the broader distribution for the multi-step sample, which indicates a higher impact of this procedure to the support material. This impact can also be seen in the fraction of micropore volume in the different samples applying the  $\beta_s$ -method (Figure 4.31). In blank SBA-15 micropores are filled with a volume of 40% of the total pore volume, whereas the impregnated samples are filled with 37% and

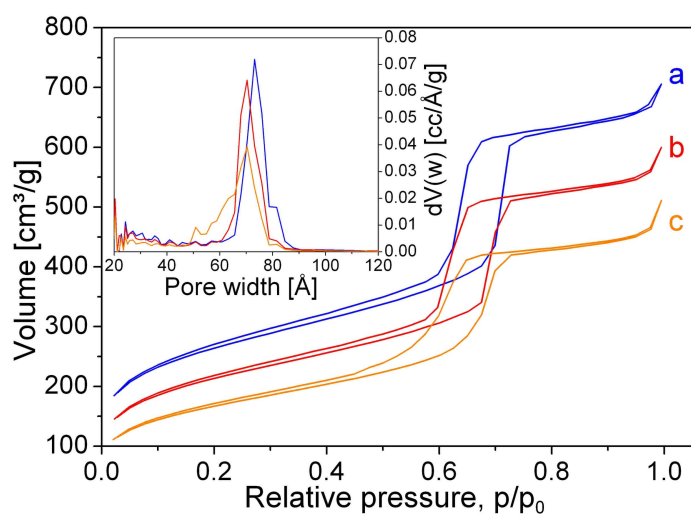


Figure 4.29:  $N_2$  isotherm and pore size distribution of (a) blank SBA-15, (b)  $V_xO_y/SBA-15^*$  and (c)  $V_xO_y/SBA-15$

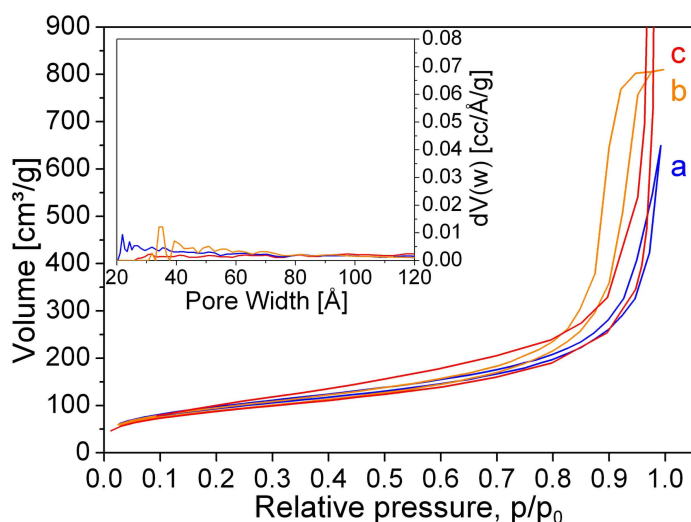


Figure 4.30:  $N_2$  isotherm and pore size distribution of (a) blank Aerosil 300, (b)  $V_xO_y/A300$  and (c)  $V_xO_y/A300^*$

the multi-step sample with 33 %, respectively.

For the samples on Aerosil 300, no change of the nitrogen isotherm could be seen (see Figure 4.30). A hysteresis appears for the multi-step sample at a relative pressure of 0.8 - 0.9, which leads to a pore size distribution with pore diameters bigger than 70 nm. As the average particle size of the Aerosil 300 is about 7 nm, this seems to be due to an agglomeration of particles. The isotherm of the incipient wetness impregnated sample shows a high amount of adsorbed volume for relative pressures above 0.9. This indicates an unrestricted monolayer-multilayer adsorption. The pore size distribution feature between 10 - 30 nm, too, seems to be due to agglomeration.

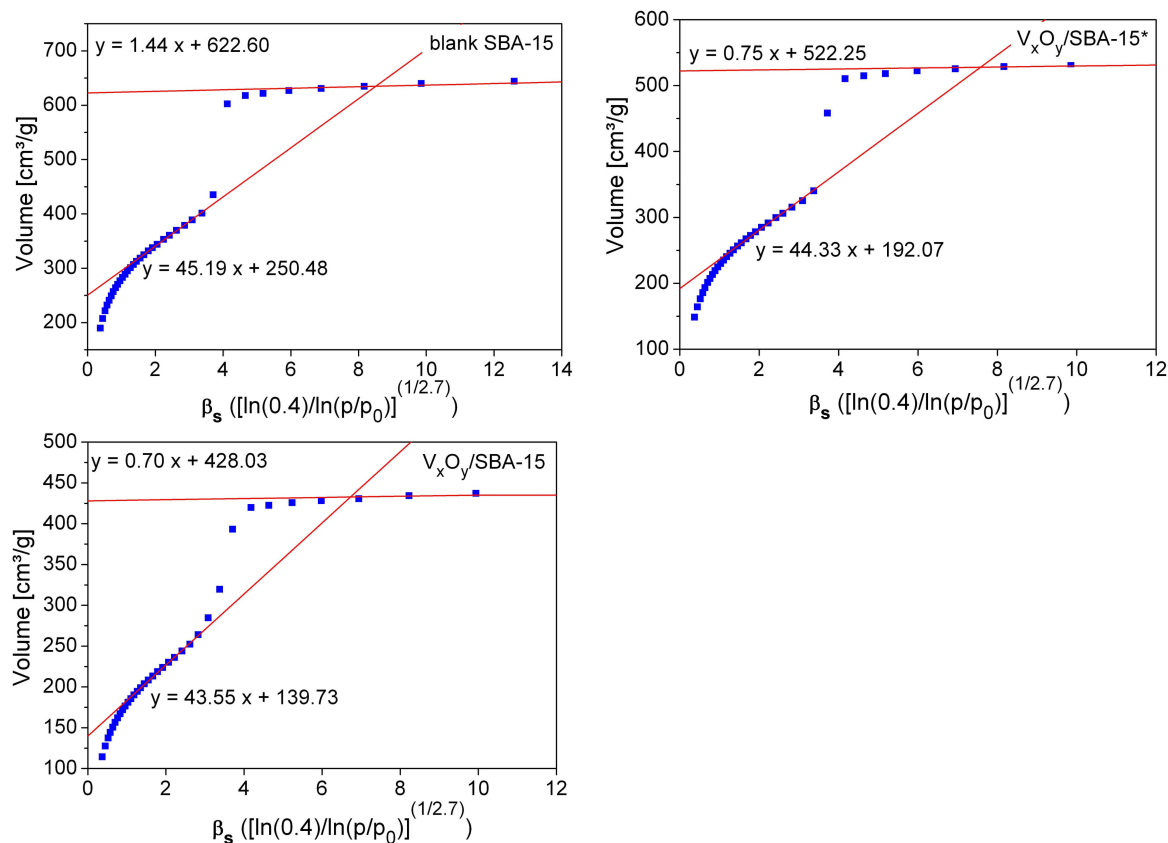


Figure 4.31:  $\beta_s$ -plots for micropore estimation of supported SBA-15 samples

Neither the low angle XRD nor the electron microscopy of vanadia on SBA-15 showed any differences compared to the blank sample. In XRD, only big crystals of  $V_2O_5$  can be seen, and for the electron microscopy the contrast of vanadium on silica is not high enough to discriminate one from the other.

### 4.3.2 Spectroscopic characterization

In order to analyze the vanadia structure of the samples Raman-, DRUV-vis- and XP spectroscopy were used.

#### Raman spectroscopy

Raman spectra for all four of the prepared samples and for the blank support materials are shown in Figure 4.32. Features delivered by the support material are at

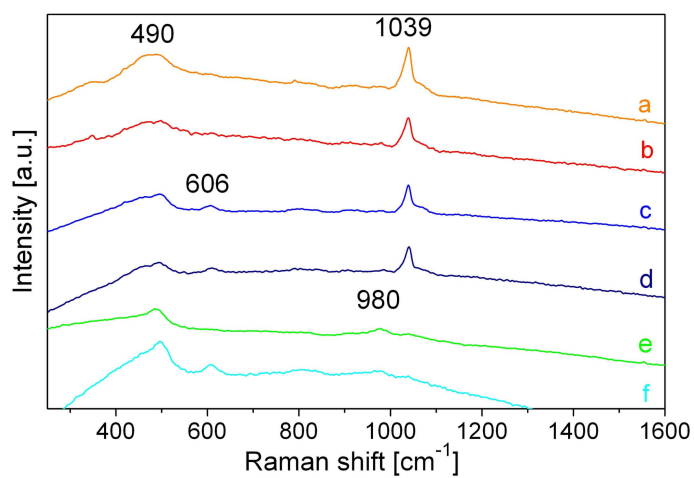


Figure 4.32: Raman spectra of (a)  $\text{V}_x\text{O}_y/\text{SBA-15}$ , (b)  $\text{V}_x\text{O}_y/\text{SBA-15}^*$ , (c)  $\text{V}_x\text{O}_y/\text{A300}$ , (d)  $\text{V}_x\text{O}_y/\text{A300}^*$ , (e) blank SBA-15 and (f) blank Aerosil 300

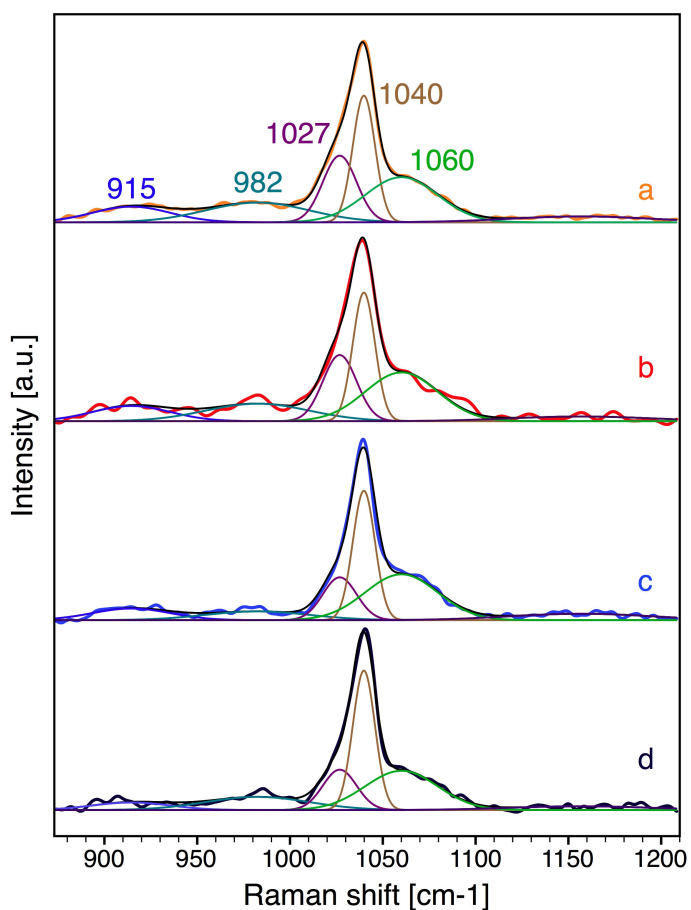


Figure 4.33: Raman spectra of the vanadyl band of (a)  $\text{V}_x\text{O}_y/\text{SBA-15}$ , (b)  $\text{V}_x\text{O}_y/\text{SBA-15}^*$ , (c)  $\text{V}_x\text{O}_y/\text{A300}$  and (d)  $\text{V}_x\text{O}_y/\text{A300}^*$

wavenumbers 490, 606 and 980. The peak at 490  $\text{cm}^{-1}$  is assigned to vibrationally isolated 4-membered siloxane rings, and the one at 606  $\text{cm}^{-1}$  can be attributed to vibrationally isolated 3-membered siloxane rings.<sup>[15][84]</sup> Si-OH stretching of free surface silanols can be seen at 980  $\text{cm}^{-1}$ .<sup>[15]</sup> The asymmetric band at  $1039 \pm 6 \text{ cm}^{-1}$  is related to tetrahedral surface vanadia species with one short V=O bond and three longer V-O bonds in the bridging position.<sup>[84][86][68]</sup>  $\text{V}_2\text{O}_5$  could not be detected.

Figure 4.33 focuses more on the vibration originating from the vanadia. It is clear that the peak has several components, which were not yet analyzed in the literature. The spectra were normalized to the vanadyl band and fitted in the range of 860 to 1210  $\text{cm}^{-1}$  with 5 curves. Intensities are found at  $915 \pm 3 \text{ cm}^{-1}$ ,  $982 \pm 3 \text{ cm}^{-1}$ ,  $1027 \pm 2 \text{ cm}^{-1}$ ,  $1040 \pm 1 \text{ cm}^{-1}$  and  $1060 \pm 3 \text{ cm}^{-1}$ . Based on theoretical calculations by Magg et al.<sup>[70]</sup>, these bands can be assigned to out-of-phase ( $915 \text{ cm}^{-1}$ ) and in-phase ( $1060 \text{ cm}^{-1}$ ) Si-O-V stretch vibrations. The band at  $982 \text{ cm}^{-1}$  was assigned to Si-OH stretches as mentioned above. As from IR spectroscopy, NEXAFS and EXAFS we have a clear indication for the presence of vanadia species containing V-O-V<sup>[97][99][21]</sup>, we assigned the V=O stretches at  $1027 \text{ cm}^{-1}$  to vanadia clusters of a low degree of polymerization and the one at  $1040 \text{ cm}^{-1}$  to vanadia clusters of a relatively higher degree of polymerization. The ratio was determined in order to compare the polymerization degree of the four samples. There is a clear difference between the support materials but only a small difference between the synthesis methods. The ratio of 0.79 for the SBA-15 samples was higher than that of 0.47 for the Aerosil samples. This suggests that the samples supported on Aerosil 300 show a higher degree of polymerization.

#### **DRUV-vis spectroscopy**

The DRUV-vis spectra in Figure 4.34 show differences between the samples concerning the support materials as well as the synthesis methods. The Kubelka-Munk units were normalized to the peak maximum in order to compare the shape of the curves. A clear shift to higher wavelength can be seen for the peak maxima of the Aerosil 300

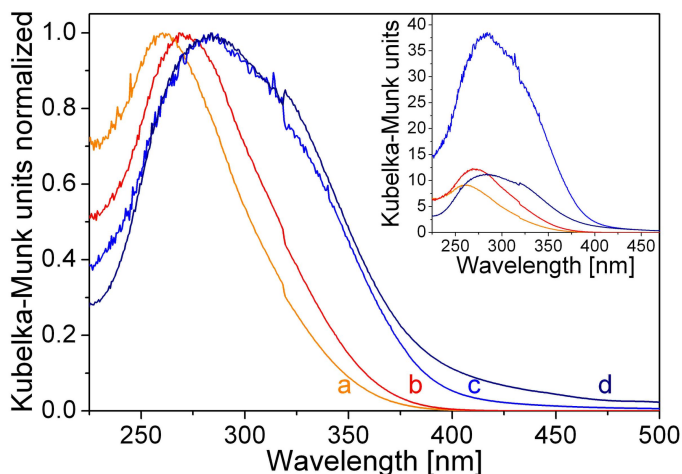
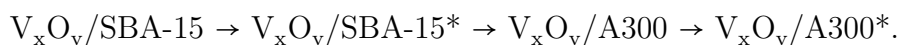


Figure 4.34: DRUV-vis spectra of (a)  $V_xO_y/SBA-15$ , (b)  $V_xO_y/SBA-15^*$ , (c)  $V_xO_y/A300$  and (d)  $V_xO_y/A300^*$

samples (285 nm) in comparison to the SBA-15 samples (260 / 270 nm). Furthermore, the peaks for these samples are broader than those of the SBA-15 samples. Among the SBA-15 samples the peak shifts from 260 nm (multi-step sample) to 270 nm (incipient wetness impregnated sample). The curve shapes of these samples do not show any significant differences. Among the Aerosil 300 samples the position of the peak maximum is at 285 nm for both samples, but the incipient wetness sample shows an additional shoulder at 425 nm.

As already described in section 4.2.1, an intensity shift to higher wavelengths could be correlated with an increase of the concentration of the oligomeric structure.<sup>[84][4][8]</sup> Therefore the DRUV-vis spectra can be interpreted as an increase of the degree of polymerization in the following order:



### XP spectroscopy

The XP spectra were normalized to the Si2p peak. The O1s and V2p emissions are depicted in Figure 4.35. The left picture shows the O1sV2p region for the two SBA-15 and Aerosil 300 samples. The O1s peak can be clearly seen in this graphical representation. The V2p<sub>3/2</sub> peak is magnified in the picture on the right-hand side. This peak is fitted with three curves for all samples. The first, namely the one at 515.8 - 0.2 eV,

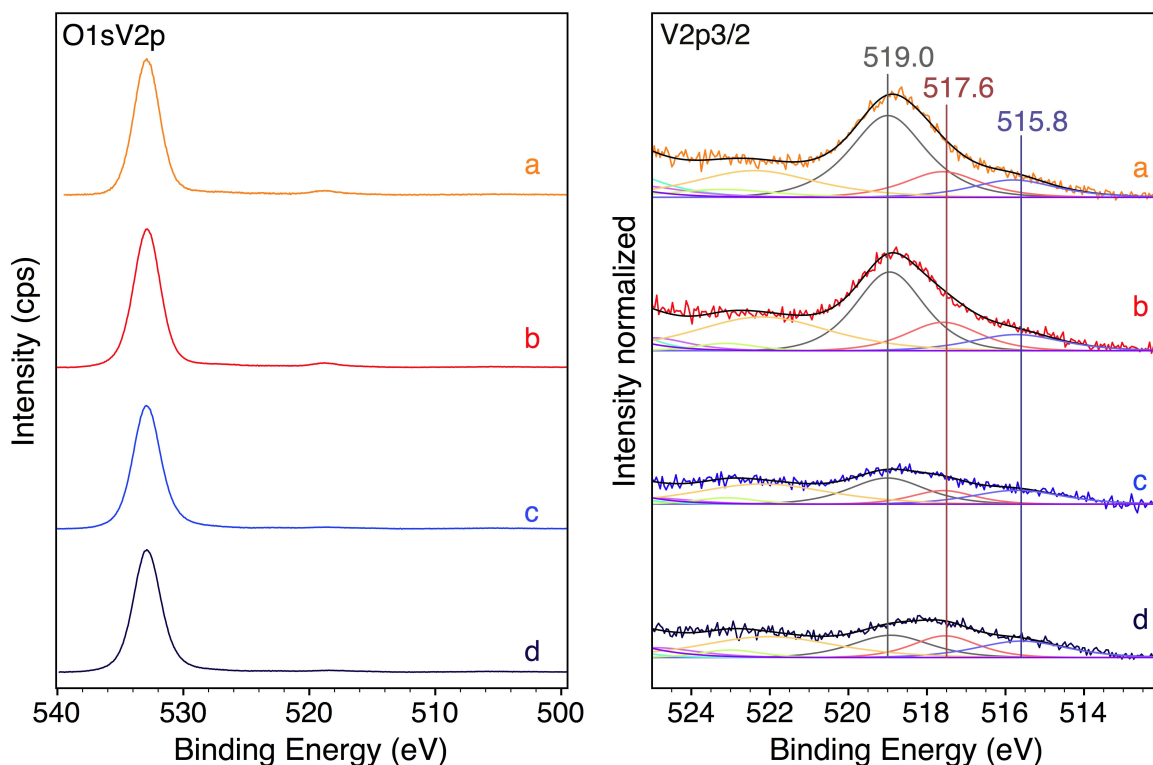
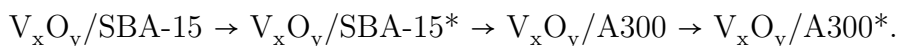


Figure 4.35: XP spectra (O1sV2p) of (a)  $V_xO_y/SBA-15$ , (b)  $V_xO_y/SBA-15^*$ , (c)  $V_xO_y/A300$  and (d)  $V_xO_y/A300^*$

can be assigned to  $V^{3+}$ , the one at  $517.6 \pm 0.1$  eV to bulk like  $V_2O_5$  and the third one at  $519.0 - 0.1$  eV to highly dispersed vanadia. This assignment has been proposed in recent work<sup>[47]</sup>. Values of the fitted area and the ratios are given in Table 4.5. The amount of the  $V^{3+}$  species is comparable for all samples. However, the ratios of the highly dispersed vanadia to the bulk like  $V_2O_5$  differ. Regarding this ratio the samples follow the order:



These results indicate the same order as found in the interpretation of the DRUV-vis data.

One idea concerning the vanadia was to use the information which can be gained by using XPS, precisely stoichiometry data, in order to add it to the structural information given by Raman- and DRUV-vis spectroscopy. Therefore, XP difference



Table 4.5: XPS: fitted areas of V2p<sub>3/2</sub> peaks

	area			$\Sigma$	area ratio
	519.0 eV	517.6 eV	515.8 eV		$\left[ \frac{519.0\text{eV}}{517.6\text{eV}} \right]$
V <sub>x</sub> O <sub>y</sub> /SBA-15	0.1084	0.0341	0.0258	0.1683	3.18
V <sub>x</sub> O <sub>y</sub> /SBA-15*	0.0913	0.0357	0.0248	0.1518	2.56
V <sub>x</sub> O <sub>y</sub> /A300	0.0336	0.0144	0.0211	0.0691	2.33
V <sub>x</sub> O <sub>y</sub> /A300*	0.0296	0.024	0.0253	0.0789	1.22

spectra were used by subtraction of the spectrum of the blank support from the supported vanadia spectrum. The resulting spectra were fitted using reference spectra of vanadia. However, the result was not satisfactory for two reasons. Firstly, there are various oxygen species contributing to the occurrence of the O1s peak, but as they cannot be assigned exclusively to vanadia, resulting values are not representative. Secondly, samples with a low vanadium content tend to become highly charged during XPS, which has an effect to the stoichiometry data. This was not expected in this extend because measurements on a V/SiO<sub>2</sub>/Si sample (prepared on flat Si(100) wafer via spin-coating impregnation) showed that the V 2p<sub>3/2</sub> signal strongly resembles that of the V<sub>x</sub>O<sub>y</sub>/SBA-15 powder catalyst regarding position, width and intensity distribution.<sup>[46]</sup> Thus it was concluded that charging does not have a significant effect on the V 2p<sub>3/2</sub> emission of the V/SBA-15 powders samples studied.

### 4.3.3 Conclusion

Differences in curve shape, intensity and position related to the support materials can be seen in DRUV-vis- and Raman spectra. Most prominently, the DRUV-vis spectra show a shift of the peak maxima to higher wavelength for the Aerosil 300 supported samples. For the same samples, Raman spectra delivers a decrease of the ratio of the vanadyl band at 1027 cm<sup>-1</sup> and 1040 cm<sup>-1</sup>. Both characteristics can be interpreted as

an increase of the degree of polymerization for vanadium on Aerosil 300.

Additionally, the synthesis method seems to influence the degree of polymerization, however to a lower degree. Less polymerized vanadia is created by using the multi-step method. Trends concerning the increase of the degree of polymerization can be stated in an order of  $V_xO_y/SBA-15 \rightarrow V_xO_y/SBA-15^* \rightarrow V_xO_y/A300 \rightarrow V_xO_y/A300^*$ .

The much more prominent influence of the support material can be explained with differences of silica material. As described in section 1.2.1 the type of silanol groups and their distribution is important for the reactivity of the material. The density of more reactive silanols seems to be higher at Aerosil 300, leading to a higher degree of polymerization of the vanadia.

# 5 Reactivity of silica-supported vanadia catalysts

## 5.1 Catalytic tests after mechanical treatment

Reactivity tests for ODH of propane show for  $V_xO_y/SBA-15$  a selectivity of 77% and of 75% for  $V_xO_y/SBA-15^*$  at a conversion of 2% (Figure 5.1). After pressure treatment, the selectivity drops to 68% for  $V_xO_y/SBA-15$  and 63% for  $V_xO_y/SBA-15^*$  at a conversion of 1.5%. This means that the pressed  $V_xO_y/SBA-15$  synthesized by using the multi-step procedure has better performance than the pressed  $V_xO_y/SBA-15^*$  synthesized with incipient wetness impregnation. From the physical characterization we were able to reason that the mesoporous structure after pressure treatment of  $V_xO_y/SBA-15^*$  completely collapses, in contrast to  $V_xO_y/SBA-15$  which is more stable. Consequently, I put forward the hypothesis that in both samples there are vanadia sites which are no longer accessible (blocked sites). For the completely destroyed  $V_xO_y/SBA-15^*$ , their amount should be higher than for the sample that has only been partially destroyed. In order to prove this theory, we plotted the conversion of propane over the modified residence time with and without a correction of the BET surface area<sup>1</sup>, and hence, of the accessible vanadia sites in Figure 5.2 and 5.3. The plot lacking correction (Figure 5.2) shows smaller conversion for the mechanically treated samples, the smallest one for the completely damaged  $V_xO_y/SBA-15^*$ . Nevertheless,

---

<sup>1</sup>The fraction of BET surface area decreased was related proportional to amount of the vanadium sites.

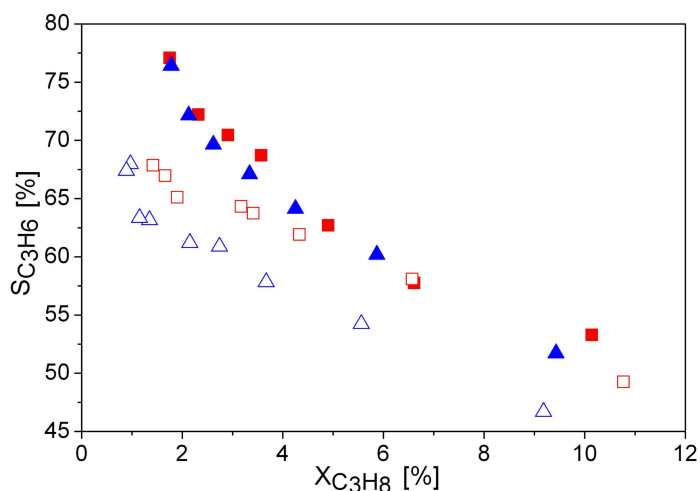


Figure 5.1: Selectivity towards propene at 500 °C before pressure treatment of (■)  $V_xO_y/SBA-15$ , (▲)  $V_xO_y/SBA-15^*$  and after pressure treatment at 752 MPa of (□)  $V_xO_y/SBA-15$ , (△)  $V_xO_y/SBA-15^*$

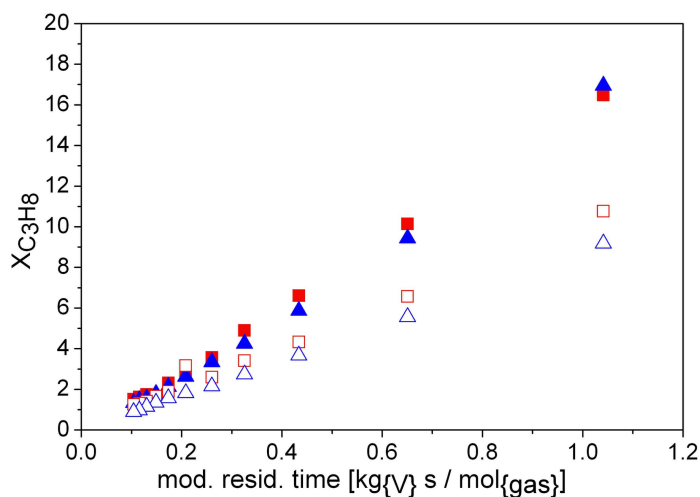


Figure 5.2: Conversion of propane at 500 °C before pressure treatment of (■)  $V_xO_y/SBA-15$ , (▲)  $V_xO_y/SBA-15^*$  and after pressure treatment at 752 MPa of (□)  $V_xO_y/SBA-15$ , (△)  $V_xO_y/SBA-15^*$

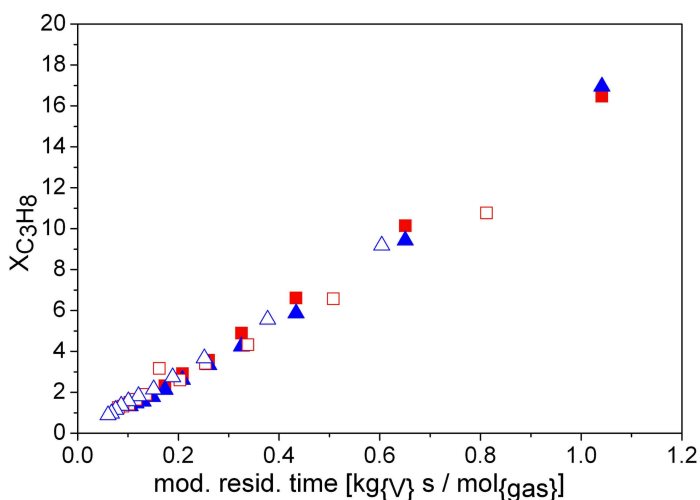


Figure 5.3: Conversion of propane before pressure treatment of (■)  $V_xO_y/SBA-15$ , (▲)  $V_xO_y/SBA-15^*$  and after pressure treatment at 752 MPa with BET surface area correction of (□)  $V_xO_y/SBA-15$ , (△)  $V_xO_y/SBA-15^*$

in the plot with a correction of accessible sites (Figure 5.3) the samples do not show any significant differences. These results confirm my theory of blocked vanadia sites after mechanical treatment.

## 5.2 Reactivity of different silica supports and synthesis methods

Supported vanadia catalysts were synthesized on two different silica materials by making use of two different preparation methods. The properties of the used supports, namely SBA-15 and Aerosil 300, are described in section 4.1. A multi-step procedure including a grafting and ion exchange step and an incipient wetness impregnation were applied as synthesis methods. These methods are described in section 3.2 and 3.3. For all samples the vanadium content was designed in order to achieve an atom density of 0.7 V-atoms/nm<sup>2</sup>. The results of spectroscopic characterization are described in section 4.3. Differences could be seen concerning the support materials in particular. This section deals with the reactivity of the specified samples.

### 5.2.1 Temperature programmed reduction and oxidation

#### Influence of pretreatment

As a pretreatment for all measurements, a flow of 20% O<sub>2</sub> in N<sub>2</sub> at 350 °C was sent through the sample for 30 min to achieve the same starting conditions for all samples. The importance of using the same conditions becomes obvious from Figure 5.4 with focusing on V<sub>x</sub>O<sub>y</sub>/SBA-15: the influence of the pretreatment on hydrogen consumption and oxidation in TPRO measurements was investigated by using pure argon and 5% oxygen in helium at 350°C before the first reduction. The first plot clearly shows a consumption of oxygen and no changes in the argon line. This indicates that there is an oxidation process taking place during the pretreatment in addition to a mere

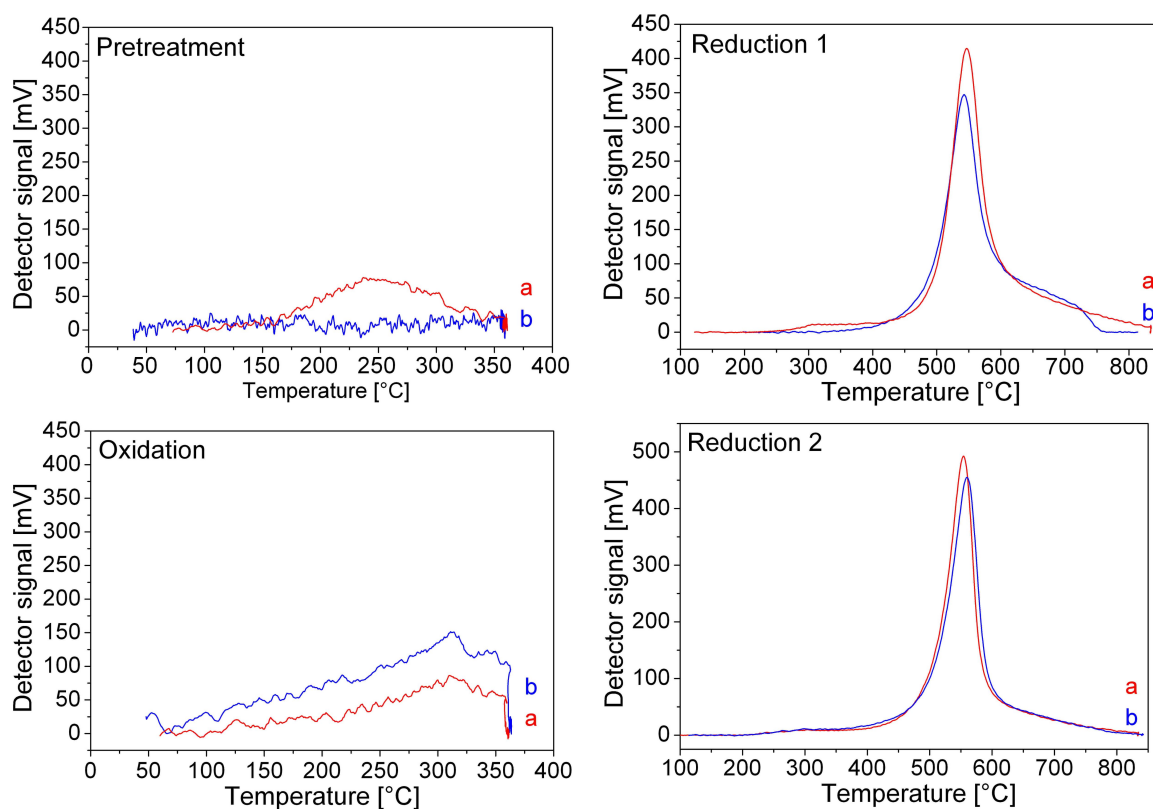


Figure 5.4: Influence of pretreatment for TPRO measurements focusing on  $V_xO_y/SBA-15$ : (a) pretreatment in oxygen, (b) pretreatment in argon

dehydration process. This assumption can be confirmed when having a look at the Reduction 1 diagram. The sample pretreated in oxygen shows a higher amount of consumed hydrogen and a slightly higher temperature for the peak maximum. Even the shapes of the two samples differ. For the following oxidation process, the amount of oxygen consumed by the sample pretreated in argon is higher than that consumed by the one pretreated in oxygen, whereas shape and peak maxima are similar. For both samples, the second reduction differs from the first one in the following aspects. The peak of hydrogen consumption shifts about 10 °C to higher temperatures, and the shape becomes narrower. However, both samples develop similar shapes during the second reduction. On the other hand, now the peak maximum for the sample pretreated in argon appears at slightly higher temperatures. Unfortunately, TPRO

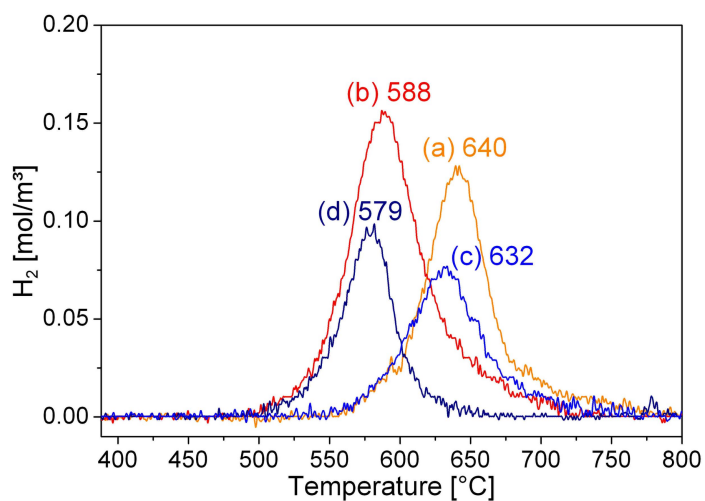


Figure 5.5: TPR of (a)  $V_xO_y/SBA-15$ , (b)  $V_xO_y/SBA-15^*$ , (c)  $V_xO_y/A300$  and (d)  $V_xO_y/A300^*$

data noted after the first reduction have to be handled with care. Our studies on the thermal stability of  $V_xO_y/SBA-15$  samples showed a decrease of the surface area after heating up to temperatures higher than 550 °C (see section 4.2.2). This decrease may have some influence on the vanadia structure as well.

### Comparison of different silica supports and synthesis methods

TPR patterns for different vanadia samples are shown in Figure 5.5. All TPR measurements were done after a pretreatment in oxygen flow and all of them show one single peak. The temperatures representing the peak maxima clearly differ with regard to the respective syntheses methods (see Figure 5.5). With 640 and 632 °C, the multi-step samples show distinctly higher maximum temperatures than the incipient wetness impregnated samples (588 and 579 °C max.). For both silica supports the difference between the synthesis methods is comparable (52 and 53 °C). When comparing the support materials, the Aerosil samples appear at lower temperatures than the SBA-15 samples synthesized by the same respective method.

In literature, TPR data for comparable systems show one single peak, too, even though the maximum temperatures differ considerably. SBA-15 systems with comparable vanadium loading (0.7 V atoms/nm<sup>2</sup>) prepared by impregnation with a solution of  $NH_4VO_3$  show maxima at about 500 °C<sup>[64][30]</sup>. For MCM-41 materials with a vana-

dium loading of 0.33 V atoms/nm<sup>2</sup>, similar temperatures have been measured<sup>[78][64]</sup>. Berndt et al.<sup>[12]</sup> have investigated MCM-41 in the loading range of 0.19 - 0.83 V atoms/nm<sup>2</sup> and for all samples generally found a temperature maximum at 527 °C and a shoulder for the highest loading at higher temperatures. Kondratenko et al<sup>[56]</sup> looked at MCM-41 with vanadium densities of 0.08 - 0.79 V atoms/nm<sup>2</sup> as well, and they found a shift of the maximum from 515 to 532 °C with increasing loading. For amorphous unstructured SiO<sub>2</sub> no significant differences were found<sup>[78][64][4][56]</sup>. In most of the cited, literature loadings surmounting the theoretically calculated monolayer coverage result in an additional shoulder at higher temperatures. These observations can be interpreted as follows: firstly, that there is an reduction of dispersed tetrahedral monomeric and/or oligomeric species at low temperatures, and followed by the reduction of bulk like V<sub>2</sub>O<sub>5</sub> or polymeric species at higher temperatures (shoulder). Most papers do not report any differences between the different silica supports. Yet there is one research group reporting different behavior of vanadia on SBA-15. Kustrowski et al.<sup>[58]</sup> investigated vanadium densities of 0.1 - 0.73 V-atoms/nm<sup>2</sup> on SBA-15 prepared by molecular designed dispersion. The peak maxima in their work are between 625...646 °C for loadings smaller than 0.4 V-atoms/nm<sup>2</sup>. For the sample of 0.73 V-atoms/nm<sup>2</sup>, they observed two overlapping peaks with peak maxima at 580 °C and 710 °C. This temperature range is comparable with the temperatures we found, but in our case, no comparable peak overlapping is found. Furthermore, they oppose the interpretation of first reducing the monomeric and/or oligomeric species. They conclude that oxygen in V-containing agglomerates has weaker bonds than oxygen in isolated V<sub>x</sub>O<sub>y</sub> species, and therefore is more easily detached by hydrogen. Thus, the reduction temperature of polymeric species of V<sup>5+</sup> is lower than that of isolated V<sup>5+</sup> species.

The amount of hydrogen consumed was used to calculate valences assuming V<sup>3+</sup> after reduction. Valences are between 4.43 and 4.29 (see Table 5.1) and are higher for the multi-step samples than for the incipient wetness samples. For both silica supports the difference between the synthesis methods is identical (0.04). In this respect,

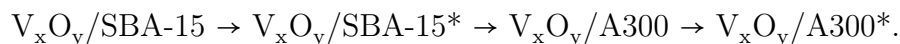


Table 5.1: TPR temperature maxima, valences provided by TPR data and activation energies provided by ODH of propane

	$T_{\max}$ [°C]	valence	$E_A$ [kJ/mol]
$V_xO_y$ /SBA-15	640	4.43	165
$V_xO_y$ /SBA-15*	588	4.39	151
$V_xO_y$ /A300	632	4.33	179
$V_xO_y$ /A300*	579	4.29	144

the amount of hydrogen consumed does not equal the required amount for a complete reduction of  $V^{5+}$  to  $V^{3+}$ . Literature reports both: a complete<sup>[4]</sup> reduction of the vanadia on silica and also incomplete reduction<sup>[30][12]</sup>. The reason for incomplete reduction could be the presence of a small amount of  $V^{4+}$  and/or  $V^{3+}$  and/or the presence of non-reducible  $V^{5+}$  species.

We concluded from the spectroscopic characterization data described in section 4.3.2 that the degree of polymerization increases in the order



Therefore a trend concerning the temperature maxima of reduction in the same order would have been easy to correlate with. However, TPR data shows a difference between the support materials which could not be distinguished that clearly with spectroscopic methods. Though, the incipient wetness impregnated samples serve as a starting point to a higher degree of polymerization than the multi-step samples. Within the support materials we observed similar differences in temperature maxima and valences.

## 5.2.2 Catalytic tests

Catalytic tests were done for the oxidative dehydrogenation of propane as described in section 2.8. Table 5.1 shows the activation energies (calculated from Arrhenius plot in Figure 5.6) for the samples tested. The multi-step samples show values of 165 kJ/mol

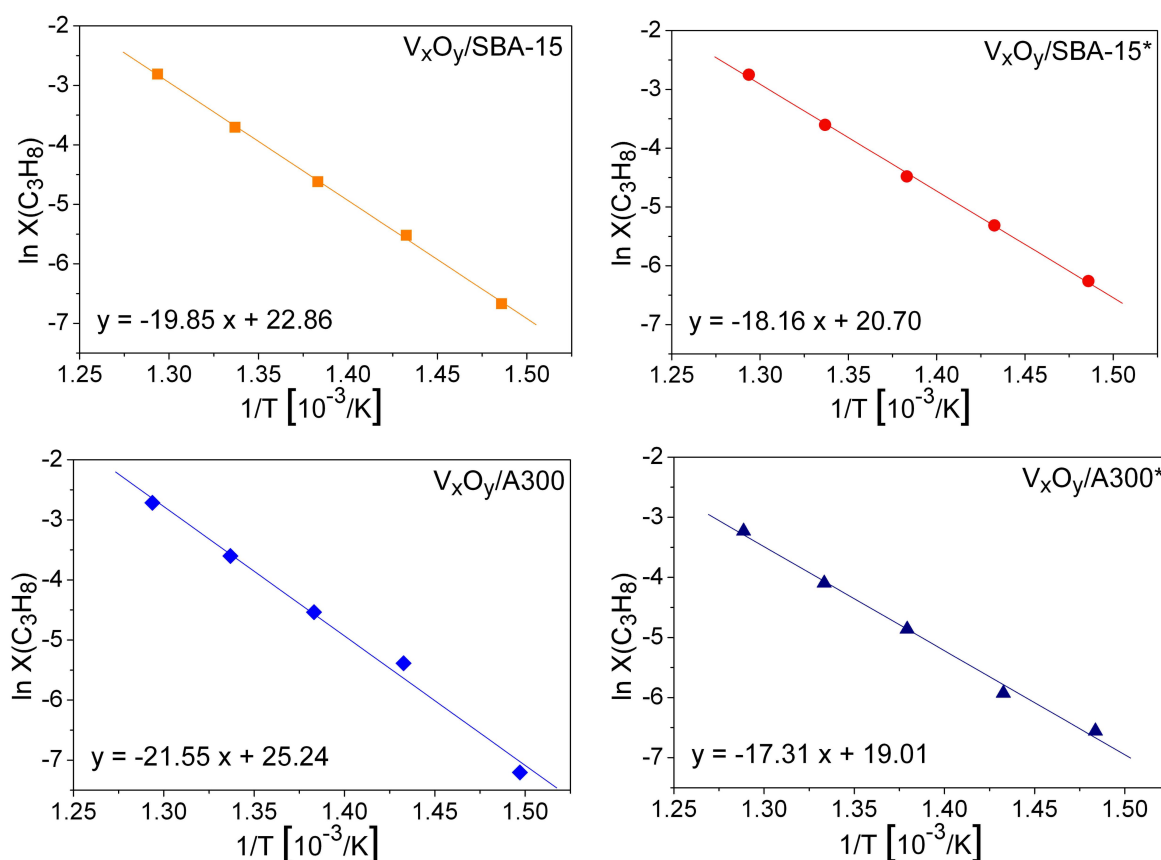


Figure 5.6: Arrhenius plot for calculation of activation energies of (■)  $\text{V}_x\text{O}_y/\text{SBA-15}$ , (●)  $\text{V}_x\text{O}_y/\text{SBA-15}^*$ , (◆)  $\text{V}_x\text{O}_y/\text{A300}$ , (▲)  $\text{V}_x\text{O}_y/\text{A300}^*$

for  $\text{V}_x\text{O}_y/\text{SBA-15}$  and 179 kJ/mol for  $\text{V}_x\text{O}_y/\text{A300}$ , while those of the incipient wetness impregnation are 151 (SBA-15) and 144 kJ/mol (A300). The values for the multi-step samples are thus higher than those of the incipient wetness impregnated samples. This fact is in agreement with the trend observed for the temperature maxima in the TPR measurements (see section 5.2.1).

The conversion-selectivity plot at 500 °C in Figure 5.7 does not show any differences between the syntheses methods or the support materials. For all samples, a selectivity of propene of about 75% at a conversion level of 2% was achieved. The selectivity decreases with increasing conversion. Hence, at a conversion of 10% the propene selectivity is 55%.

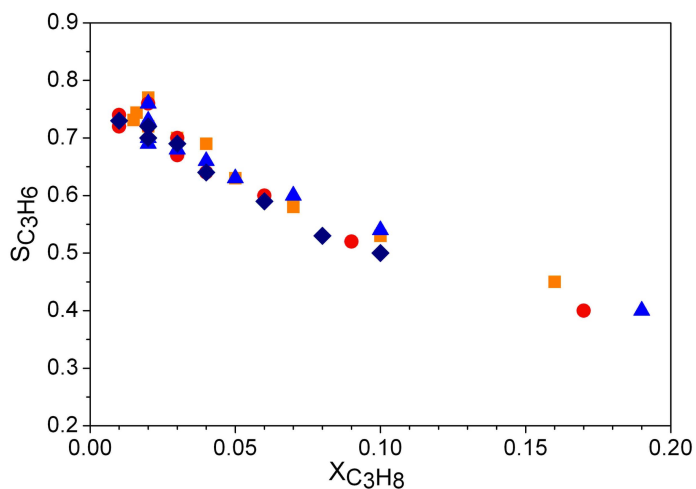


Figure 5.7: Selectivity towards propene at 500 °C of (■)  $V_xO_y/SBA-15$ , (●)  $V_xO_y/SBA-15^*$ , (◆)  $V_xO_y/A300$ , (▲)  $V_xO_y/A300^*$

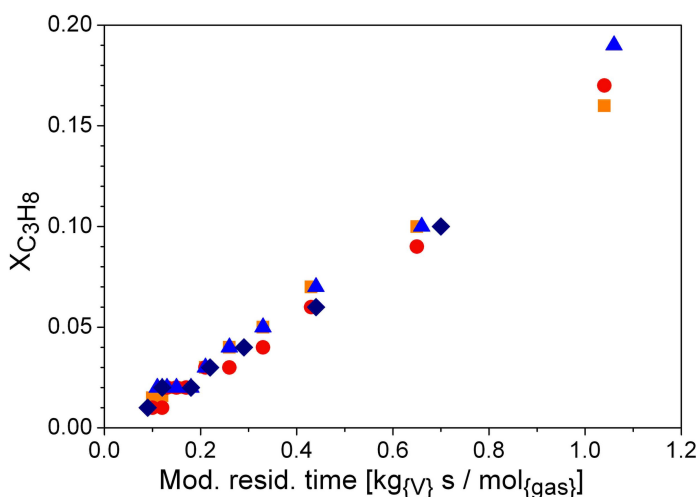


Figure 5.8: Conversion of propane at 500 °C of (■)  $V_xO_y/SBA-15$ , (●)  $V_xO_y/SBA-15^*$ , (◆)  $V_xO_y/A300$ , (▲)  $V_xO_y/A300^*$

When comparing the degree of conversion plotted over the residence time, normalized to the amount of vanadia, the samples show no differences either at the conditions used (Figure 5.8). The selectivity of CO (given in Figure 5.9) is approximately 25% at propane conversion of 2% and about 30% at a conversion of 10% for all samples. For  $CO_2$  the values for the selectivity are <5% and 15%, respectively. Here, no significant differences between the samples could be observed either. Furthermore ethene and methanol was detected for all samples, but a quantitative evaluation was not possible. A quantitative comparison with literature data is quite difficult because of the different reaction conditions and conversion ranges. Only Kondratenko et al.<sup>[56]</sup> gives ODH of propane data in about the same conversion range observed by us. They com-

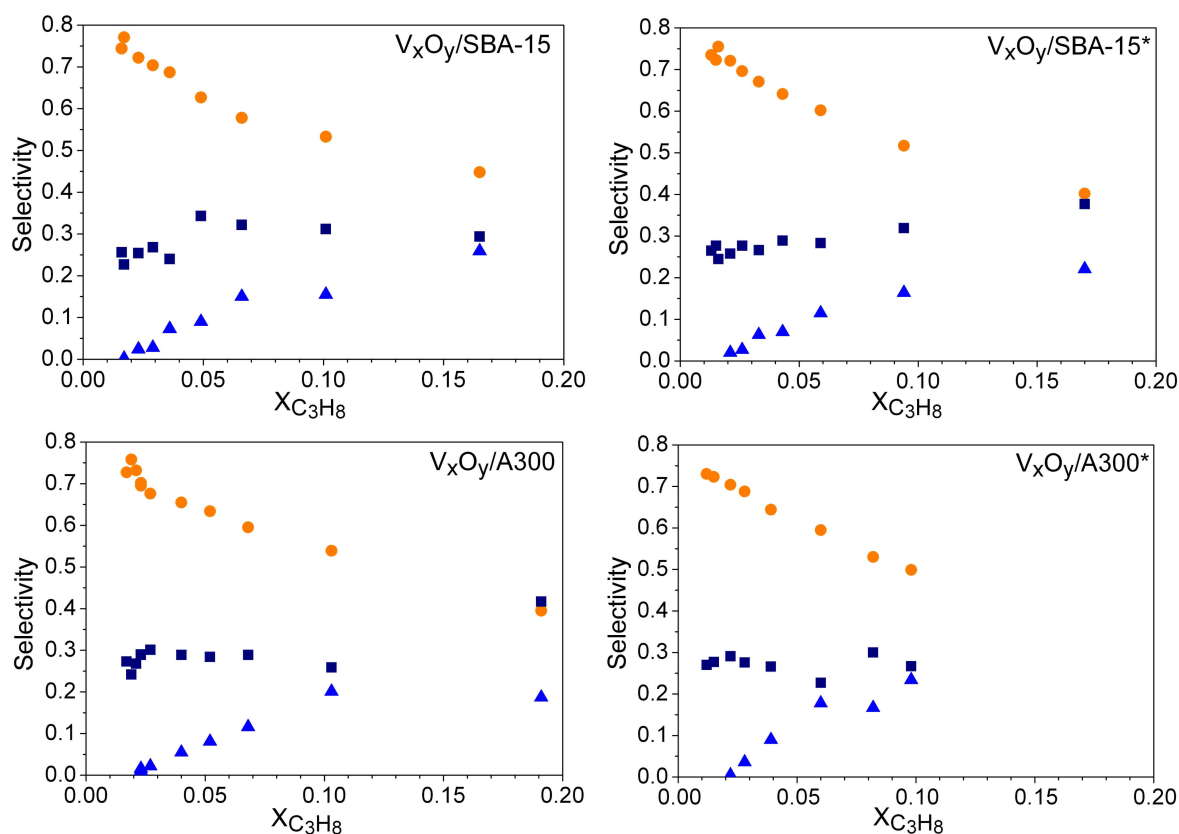


Figure 5.9: Selectivity towards (●)  $C_3H_6$ , (■) CO and (▲)  $CO_2$  of  $V_xO_y/SBA-15$ ,  $V_xO_y/SBA-15^*$ ,  $V_xO_y/A300$  and  $V_xO_y/A300^*$  at 500 °C

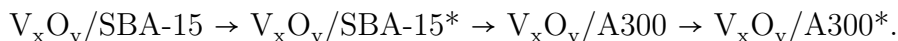
pared MCM-41 with amorphous silica as support materials for vanadium (V loading 0.08 - 1.38 atoms/nm<sup>2</sup>) at a reaction temperature of 475 °C and found no significant difference concerning the selectivities of propene, which again fits perfectly with our data. In contrast to that Pena et al. [78], who compared MCM-41, MCM-48, and amorphous silica as supports (V loading 0.04 - 0.33 atoms/nm<sup>2</sup>, reaction temperature of 500 - 550 °C), found a higher propene selectivity for the MCM materials than for the amorphous silica. Liu et al. [64] on the other hand stated higher conversions to olefins for SBA-15 than for MCM-41 and amorphous silica as support materials (V loading 0.21 - 2.4 atoms/nm<sup>2</sup>, reaction temperature of 600 °C). Note that the before mentioned investigations were made on the basis of materials with comparable weight% of vanadia. Because of the different surface areas of the supports, the vana-

dium density is not comparable, and therefore, the samples show inconsistent degrees of dispersion/polymerization. The differences observed by Pena et al.<sup>[78]</sup> and Liu et al.<sup>[64]</sup> could be explained by their disregard of the different features of vanadia species used in the samples and in the case of Liu et al by the high temperature used for reaction.

### 5.2.3 Conclusion and outlook

TPR data show clear differences with regard to the synthesis method. The peak maxima appear at higher temperatures for the multi-step samples than for the incipient wetness samples. This trend can also be seen in the average oxidation state and in the activation energies of the oxidative dehydrogenation of propane.

We concluded from the spectroscopic characterization data described in section 4.3.2 that the degree of polymerization increases in the order



As already described in section 5.2.1 a trend concerning the temperature maxima of reduction and activation energies in the same order would have been easy to interpret. However, TPR data show a difference between the synthesis methods which could not be found that clearly with spectroscopic methods. Nevertheless, the incipient wetness impregnated samples serve as a starting point to a higher degree of polymerization than the multi-step samples. Within the support materials we observed similar differences in temperature maxima and valences.

During the oxidative dehydrogenation of propane, no significant changes within the different support materials and/or synthesis methods were observed concerning both conversion and selectivity, although we observed differences in the vanadia structure using Raman, UV-vis spectroscopy and XPS. This could lead to the assumption that during catalysis the vanadia structures of all samples converge to very similar ones. However, UV-vis spectroscopy of the samples before and after reaction shows differences. In Figure 5.10 it is obvious that after reaction the samples show a decreased

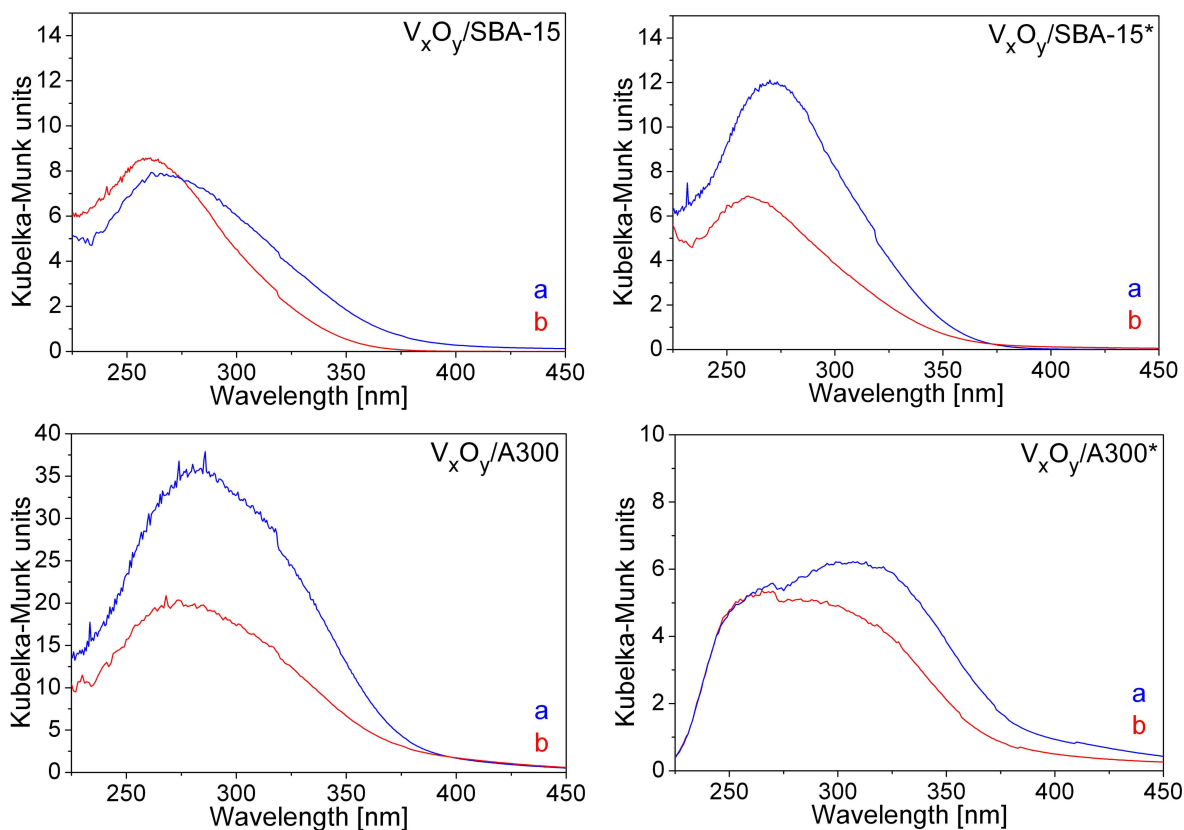


Figure 5.10: UV-vis spectra (a) before and (b) after ODH of propane

intensity at higher wavelengths, but they do not resemble each other.

Another more likely explanation could be that in each sample there are comparable species which are responsible for the ODH reaction, but that the spectroscopic data are dominated by those which are relevant for our purpose. This assumption directly leads to the question how these different species can be distinguished and how one can find out which of them are responsible for ODH reaction.

Another question which arises is due to the fact that TPR data show clear differences at least between the synthesis methods. TPR gives information about the reducibility of the catalyst, consequently one would expect that this has an influence to the ODH reaction. On the one hand, there are differences in the activation energies of the samples but on the other hand, a clear correlation between both results is not visible. For a better comparison of TPR data and ODH reaction it would be useful to calculate

activation energies by running TPR at different heating rates and/or recording TPR data with propane as a reduction gas.

The challenge for future investigation would be to discriminate between species which are responsible for catalytic activity and between the ones which are not responsible. From my point of view, the next step in this direction is to find out which characterization method is to be preferred. Therefore, in situ analysis for ODH of propane with different spectroscopic tools is necessary. If one can observe changes concerning species with different degree of polymerization during reaction, one will be a step closer for discriminating the desired species.





## 6 Characterization and catalytic tests of V/Ti-supported SBA-15 catalysts

Materials containing vanadium and titanium oxides are known as excellent catalysts in a number of redox reactions. Vanadium oxide is a powerful redox catalyst in many industrial processes, and it is used in oxidation reactions for the manufacturing of important chemicals.<sup>[100]</sup> Titanium oxide, when superimposed on a silica support, is mainly used as a photocatalyst, acid catalyst, and redox catalyst.  $\text{TiO}_2$  is widely used, as well, for many oxidation reactions of organic molecules requiring a highly dispersed layer on the support<sup>[35]</sup>. Silica-based materials containing titanium have been studied intensely for several years. Among these catalysts, titanium silicalite-1 (TS-1) selectively catalyzes a broad range of oxidations with hydrogen peroxide.<sup>[54]</sup> Catalysts based on  $\text{V}_2\text{O}_5/\text{TiO}_2$  are mainly used in the oxidation of *o*-xylene to phthalic anhydride, in the ammoxidation of toluene and in the reduction of nitrogen oxides.<sup>[49]</sup> It is generally recognized that  $\text{TiO}_2$  (anatase) is the best support; however, it only has a low specific surface area. The use of a silica support instead of titania offers advantages because of the higher surface area and higher resistance to sintering processes.<sup>[86]</sup> In order to combine the high surface area of mesoporous silica with the catalytic properties of  $\text{V}_2\text{O}_5/\text{TiO}_2$ , SBA-15 has to be covered by dispersed titania and doped with vanadia. The following section shows first results on the characterization of several titania loadings supported on SBA-15. Furthermore, a vanadia-titania SBA-15 catalyst was tested in the oxidative dehydrogenation of propane.

Table 6.1: BET surface area and pore volume of Ti/SBA-15 with several loadings

	loading	density	$A_{\text{BET}}$	$V_{\text{P}}$	$d_{\text{p}}$
	[wt%]	$[\frac{\text{Ti-atoms}}{\text{nm}^2}]$	$[\text{m}^2/\text{g}]$	$[\text{cm}^3/\text{g}]$	$[\text{nm}]$
SBA-15			668	0.75	6.5
3 Ti/SBA-15	3	0.66	591	0.70	6.5
5 Ti/SBA-15	5	1.3	517	0.63	6.5
10 Ti/SBA-15	10	3.1	447	0.55	(5.1) 6.4
20 Ti/SBA-15	20	8.2	382	0.48	(5.1) 6.4

## 6.1 Characterization of Ti-supported SBA-15 with different loadings

SBA-15 was synthesized as described in section 3.1. Titania was incorporated via incipient wetness impregnation (see section 3.3) using Titanium(IV) isopropoxide (99.999%, Sigma Aldrich) as titanium source. The titanium loading was increased from 3 to 20 wt%, with the result of a titanium density of 0.66 to 8.2 Ti-atoms/nm<sup>2</sup>.

Table 6.1 shows the specific BET area, the average pore volume and pore size of the samples. BET area and pore volume decrease with an increasing titanium loading. The pore size of 6.5 nm remains constant for loadings smaller than 10 wt%. Starting with this loading the pore size distribution becomes bimodal by showing a second smaller peak at 5.1 nm.

### Raman spectroscopy

Figure 6.1 shows Raman spectra of blank SBA-15, Ti/SBA-15 and TiO<sub>2</sub> anatase (Sigma Aldrich). In the spectra of TiO<sub>2</sub> one may note five clear peaks at 144, 196, 395, 516 and 637 cm<sup>-1</sup>. These bands are confirmed by literature data.<sup>[85][67]</sup> The same bands are present in the spectrum of 20 Ti/SBA-15, indicating crystalline TiO<sub>2</sub>. For the samples with lower loading no bands for crystalline TiO<sub>2</sub> are detected. The spec-

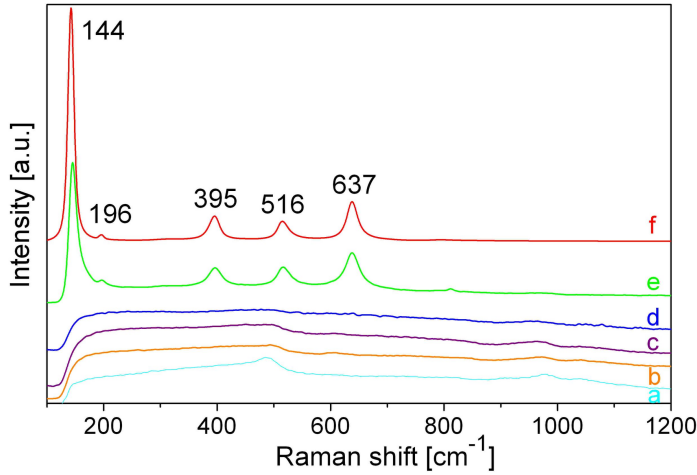


Figure 6.1: Raman spectra of (a) blank SBA-15, (b) 3wt% Ti/SBA-15, (c) 5wt% Ti/SBA-15, (d) 10wt% Ti/SBA-15, (e) 20wt% Ti/SBA-15 and (f) TiO<sub>2</sub> anatase

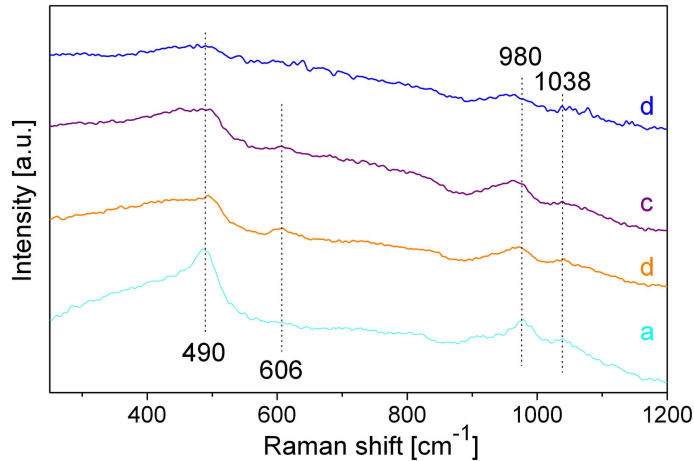


Figure 6.2: Raman spectra of (a) blank SBA-15, (b) 3wt% Ti/SBA-15, (c) 5wt% Ti/SBA-15 and (d) 10wt% Ti/SBA-15

tra of these samples are magnified in Figure 6.2. For blank SBA-15 bands appear at 490, 606, 980 and 1038 cm<sup>-1</sup>. The peak at 490 cm<sup>-1</sup> is assigned to vibrationally isolated 4-membered siloxane rings and the one at 606 cm<sup>-1</sup> to vibrationally isolated 3-membered siloxane rings.<sup>[15][84]</sup> Si-OH stretching of free surface silanols can be observed at 980 cm<sup>-1</sup>.<sup>[15]</sup> With the increase of titanium loading the band at 490 cm<sup>-1</sup> is getting weaker, and the one at 980 cm<sup>-1</sup> is getting broader and slightly shifted to 970 cm<sup>-1</sup>. In literature a band between 960 and 970 cm<sup>-1</sup> is assigned to asymmetric Si-O-Ti stretches of isolated tetrahedrally coordinated titania.<sup>[5][6][54][90]</sup> Alternatively, this band could be assigned to Ti-OH stretches.

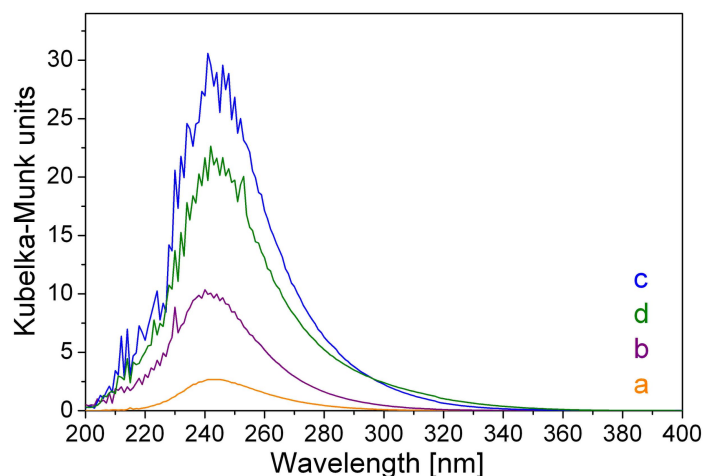


Figure 6.3: DRUV-vis spectra of (a) 3wt% Ti/SBA-15, (b) 5wt% Ti/SBA-15, (c) 10wt% Ti/SBA-15 and (d) 20wt% Ti/SBA-15

### DRUV-vis spectroscopy

Figure 6.3 shows the DRUV-vis spectra of Ti/SBA-15 after pretreatment in 20% O<sub>2</sub> / N<sub>2</sub> at 350 °C. The peak maxima of the Kubelka-Munk units all appear at 243 nm with a tail towards a higher wavelength. The intensity mounts with an increase of loading, except for the spectrum found for the 20 Ti/SBA-15 sample. This sample displays a lower intensity than the 10 Ti/SBA-15 sample at 240 nm, but the tail is higher for wavelengths above 295 nm. Interpretations of UV-vis data for titania are going back to the investigation of titanium silicalites, e.g. TS-1. In these samples, the titania becomes tetrahedrally coordinated and shows one single absorption maximum at 208 nm due to O<sup>2-</sup> → Ti<sup>4+</sup> charge transfer transition.<sup>[36] [6] [54]</sup> In Ti-β zeolites an additional band at 270 nm appears when extra framework Ti species are present. This band is ascribed to octahedral Ti with the shape of Ti-O-Ti chains.<sup>[28]</sup> A similar band is observed in Engelhard titanosilicates (ETS-10) at 282 nm and ascribed to straight Ti-O-Ti chains present in those microporous Ti-silicates.<sup>[14] [80]</sup> This material shows a second band at 214 nm that is related to a ligand-to-metal charge transfer (O<sup>2-</sup>-Ti<sup>4+</sup> → O-Ti<sup>3+</sup>).<sup>[14]</sup> The Ti-silicate ETS-4 shows main bands at 246 and 285 nm. The former is related to tetrahedral silicate units bridging two TiO<sub>6</sub> octahedra and thereby forming Ti-O-Si-O-Ti structures, and the latter is related to corner-sharing TiO<sub>6</sub> octahedra and isolated TiO<sub>6</sub> octahedra.<sup>[5]</sup> Crystalline TiO<sub>2</sub> shows an absorption

band at 330...360 nm.<sup>[6] [85] [19] [5]</sup>

Judging from these observations, we can relate the main band (243 nm) in our samples to tetrahedrally coordinated titania and the tail to octahedrally coordinated titania in chains. The amount of these chains increases with increased loading. For the highest loading of 20 wt%, a small intensity is observed at wavelength higher than 330 nm which indicates the presence of crystalline TiO<sub>2</sub>.

### XP spectroscopy

Figure 6.4 and Figure 6.5 show XP spectra of the different titanium loaded SBA-15 samples. The reference sample TiO<sub>2</sub> anatase shows the maximum of the Ti2p<sub>3/2</sub> at 459.0 eV, which fits well with the values given in literature.<sup>[1]</sup> Samples with a loading up to 10 wt% show a broader peak with a maximum at 459.8 eV. The 20 wt% sample shows the peak maximum at 459.0 eV, which indicates the presence of crystalline TiO<sub>2</sub>, and a shoulder at 459.8 eV. A peak at 560.0 eV is predominant for TS-1.<sup>[27]</sup>

The O1s spectrum shows the main feature at 532.9 eV, which mainly results from the silica support. With higher loading of titanium a shoulder at 530.2 eV appears indicating TiO<sub>2</sub>. This shoulder is clearly visible for the 20 wt% sample. These data are can be confirmed by the literature.<sup>[67] [27]</sup>

### Conclusion

In different spectroscopic characterization methods we see crystalline TiO<sub>2</sub> at a titanium density of 8.2 atoms/nm<sup>2</sup> supported on SBA-15. Up to a density of 3.1 titanium atoms/nm<sup>2</sup>, no crystallinity can be detected. Raman shows a weak intensity at 970 cm<sup>-1</sup> for low loading, which is assigned to asymmetric Si-O-Ti stretches of isolated tetrahedrally coordinated titania in literature. DRUV-vis spectra show their main intensity at 243 nm, which is assigned to tetrahedrally coordinated titania as well, with the difference that here, we find units bridging two TiO<sub>6</sub> octahedra forming Ti-O-Si-O-Ti structures, not isolated ones. This leads to the conclusion, the Raman band at

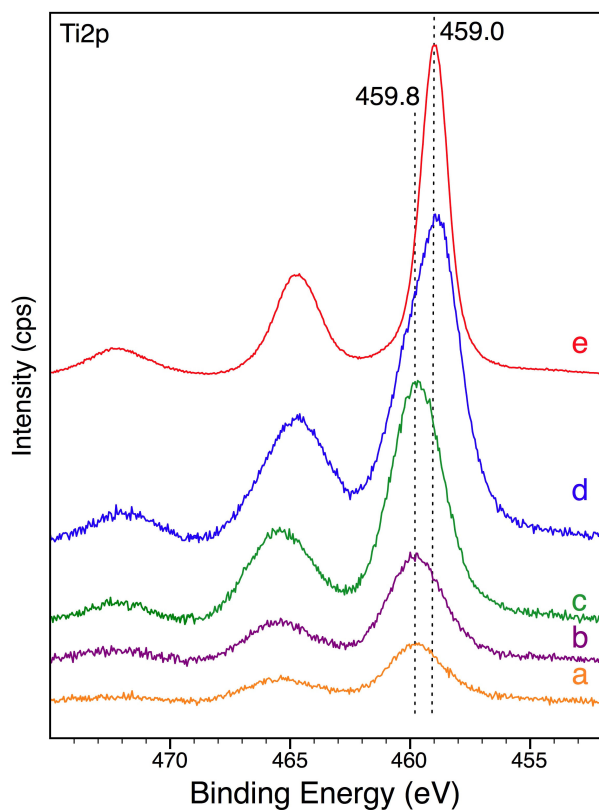


Figure 6.4: Ti2p XPS spectra of (a) 3 wt% Ti/SBA-15, (b) 5 wt% Ti/SBA-15, (c) 10 wt% Ti/SBA-15, (d) 20 wt% Ti/SBA-15 and (e) TiO<sub>2</sub> anatase

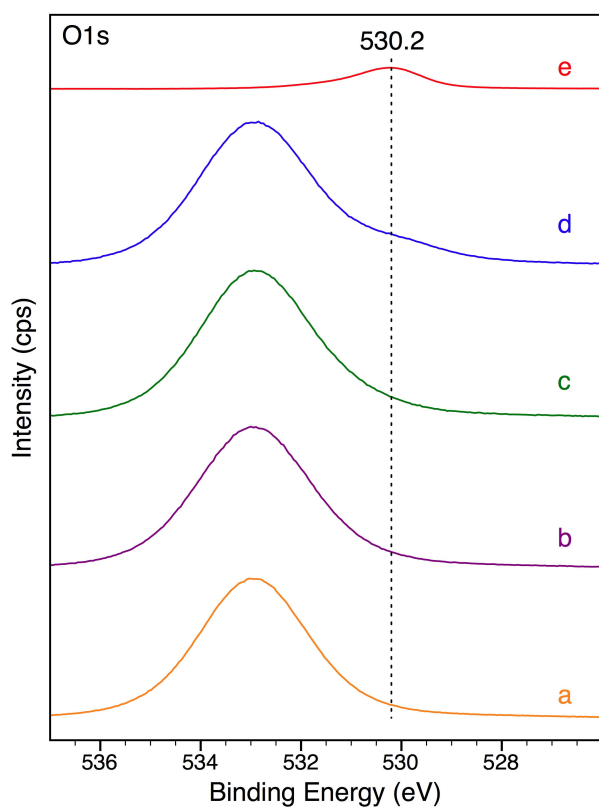


Figure 6.5: O1s XPS spectra of (a) 3 wt% Ti/SBA-15, (b) 5 wt% Ti/SBA-15, (c) 10 wt% Ti/SBA-15, (d) 20 wt% Ti/SBA-15 and (e) TiO<sub>2</sub> anatase

970  $\text{m}^{-1}$  is more likely due to Ti-OH stretches than to isolated titania sites. The tail in the DRUV-vis spectra with intensity at 285 nm can be assigned to octahedrally coordinated titania in chains. With increasing loading, the chains are growing until crystalline  $\text{TiO}_2$  is formed. Using this cognition for interpretation of the XPS  $\text{Ti}2\text{p}_{3/2}$  peak one can assign the feature at higher binding energy to tetrahedrally coordinated titania chains and the one at lower binding energy to octahedrally coordinated titania.

## 6.2 Characterization and catalytic tests of V/Ti-supported SBA-15

In order to combine the catalytic properties of vanadia/titania catalysts with the high surface area of SBA-15, a sample with both elements was prepared using incipient wetness impregnation see section (3.3). Firstly, the SBA-15 was impregnated with Titanium(IV) isopropoxide, and then calcined. Afterwards, a part of this sample was impregnated with Vanadium (V) triisopropoxide oxide and calcined in the same way.

Table 6.2: BET surface area and pore volume of Ti/SBA-15 and V-Ti/SBA-15

	loading		density		$A_{\text{BET}}$ [ $\text{m}^2/\text{g}$ ]	$V_{\text{P}}$ [ $\text{cm}^3/\text{g}$ ]	$d_{\text{P}}$ [nm]
	Ti [wt%]	V [wt%]	$[\frac{\text{Ti-atoms}}{\text{nm}^2}]$	$[\frac{\text{V-atoms}}{\text{nm}^2}]$			
SBA-15					944	1.2	7.5
Ti/SBA-15	3		0.53		715	0.91	7.0
V-Ti/SBA-15	3	3	0.74	0.73	513	0.72	7.0

Table 6.2 shows the titanium and vanadium density as well as the BET surface areas, the average pore volume and pore size. The samples are prepared in such a way that the combined titanium-vanadium sample displays comparable densities of both elements. The surface area and pore volume decrease with each treatment. Both pore size decreases only during the first synthesis; afterwards it remains constant at 7.0 nm with incorporated titania and vanadia.

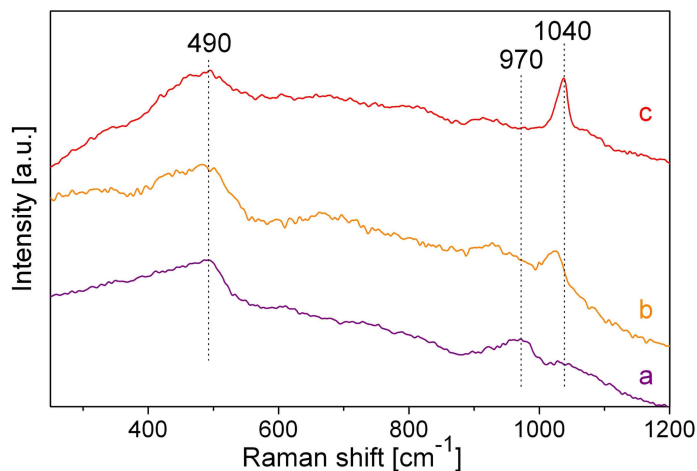


Figure 6.6: Raman spectra of (a) Ti/SBA-15 (*asis*), (b) V-Ti/SBA-15 (*asis*) and (c) V-Ti/SBA-15 (*pretreated*)

### Raman spectroscopy

The Raman spectra in Figure 6.6 show the Ti/SBA-15 sample measured *asis* and the V-Ti/SBA-15 both in the *asis* state and after pretreatment as described in section 2.6 (20% O<sub>2</sub> / N<sub>2</sub> at 350 °C). The Ti/SBA-15 sample did not undergo any pretreatment, because no significant differences could be seen before and after it. The sample without vanadia shows the same features described in section 6.1. In the spectrum of Ti/SBA-15 a broad band at 970 cm<sup>-1</sup> (tetrahedrally coordinated titania or Ti-OH) is observed, but it can not be detected for the V-Ti/SBA-15 sample. The band at 1040 cm<sup>-1</sup> (vanadyl stretches) can already be seen for the V-Ti/SBA-15 *asis* sample and is much more prominent for the pretreated sample.

### DRUV-vis spectroscopy

The UV-vis spectrum of Ti/SBA-15 has already been described in section 6.1. The spectrum of V-Ti/SBA-15 is dominated by features of the V<sub>x</sub>O<sub>y</sub>/SBA-15 samples (see section 4.2.1). Both spectra are measured after pretreatment in 20% O<sub>2</sub> / N<sub>2</sub> at 350 °C. Transitions between 260 and 300 nm are due to a charge transfer from the interface atoms of oxygen to vanadium  $\pi(\text{V}-\text{O}-\text{Si}) \rightarrow 3d_{\delta}(\text{V})$ , including terminal oxygen atoms [ $\pi(\text{V}=\text{O}) + \pi(\text{V}-\text{OH})$ ]. Since the signal of titania is in the same region as that of vanadia, the bands are overlapping and can not be separated.



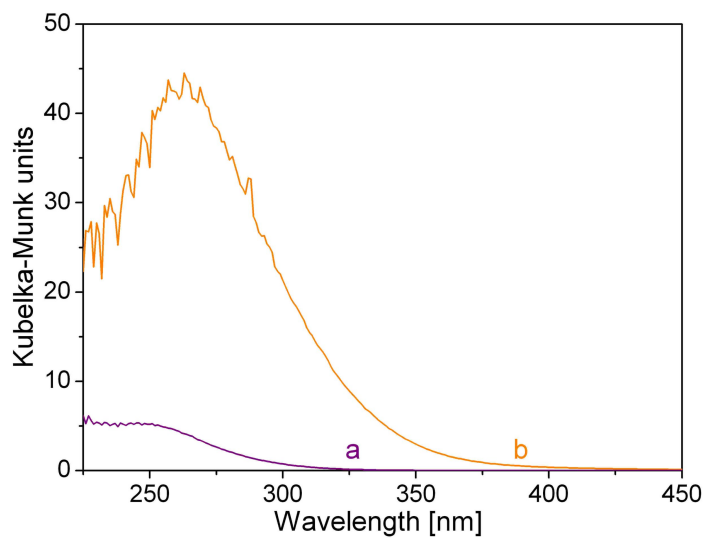


Figure 6.7: DRUV-vis spectra of (a) Ti/SBA-15 and (b) V-Ti/SBA-15

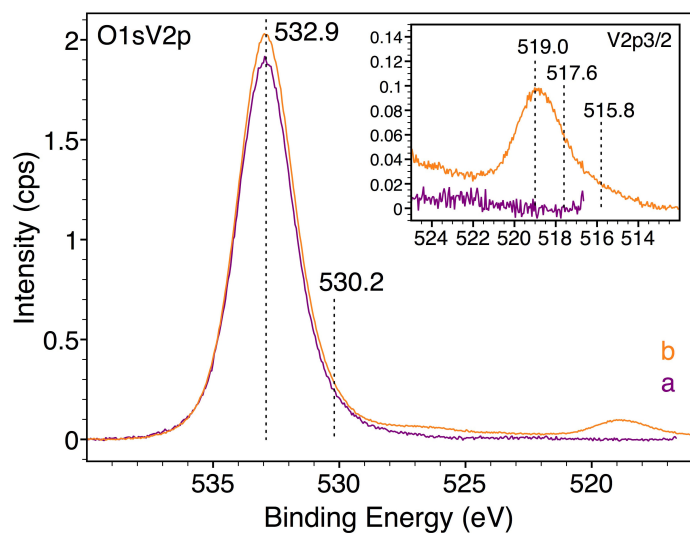


Figure 6.8: O1sV2p XP spectra of (a) Ti/SBA-15 and (b) V-Ti/SBA-15

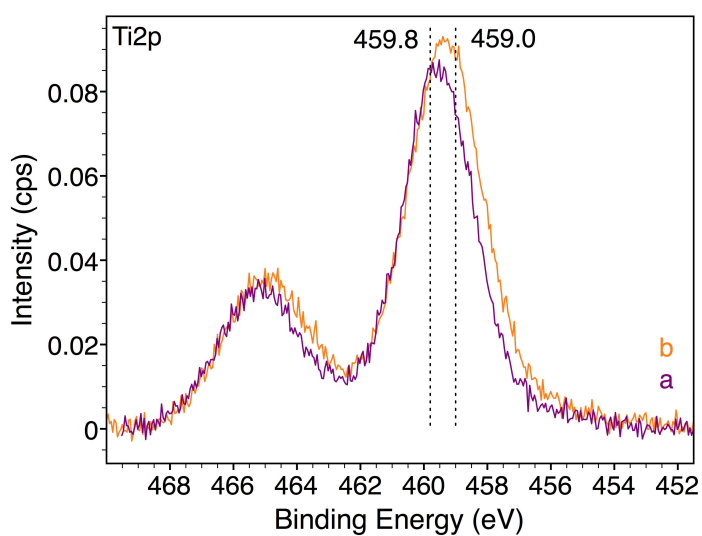


Figure 6.9: Ti2p XP spectra of (a) Ti/SBA-15 and (b) V-Ti/SBA-15

### XP spectroscopy

The XP spectra of both samples are normalized to the area of the Si2p peak. Looking at the O1s spectra in Figure 6.8, a higher intensity of the main binding energy at 532.9 eV appears for the V-Ti/SBA-15. This is also the case for the feature at 530.2 eV. Due to the fact that there are various oxygen species which contribute to the O1s signal, it is hard to determine which species is growing. A similar behavior can be seen for the Ti2p peak. The intensity of V-Ti/SBA-15 is higher than the one of Ti/SBA-15, especially at lower binding energies.

For the V2p peak the shape and intensity of the V-Ti/SBA-15 sample is comparable to those of  $V_xO_y$ /SBA-15 of section 4.3.2.

### Catalytic testing

	$E_A$ [kJ/mol]
$V_xO_y$ /SBA-15*	151
Ti/SBA-15	122
V-Ti/SBA-15	101

Table 6.3: Activation energies for ODH of propane

Tests for the catalytic performance of the Ti-SBA-15 samples were done for the ODH of propane (see section 2.8). When comparing the activation energies (calculated from Arrhenius plots in Figure 5.6 and 6.10) of  $V_xO_y$ /SBA-15\*, Ti/SBA-15\* and V-Ti/SBA-15\*, the combination of titanium and vanadium shows the lowest one (101 kJ/mol), followed by Ti/SBA-15\* (122kJ/mol) and  $V_xO_y$ /SBA-15\* (151 kJ/mol).

Conversion-selectivity plots of the three samples (Figure 6.11) show very different kinds of behavior at 500 °C under identical conditions. The vanadia sample covers a propane conversion range from 2% to 17%, the titania sample from 1% to 7%, and the combined titania-vanadia sample from 19% to 26%. Only in the latter sample the oxygen conversion is 100%. For this reason, we measured the combined sample again under the same conditions, but at a temperature of 450 °C. In this case the conversion

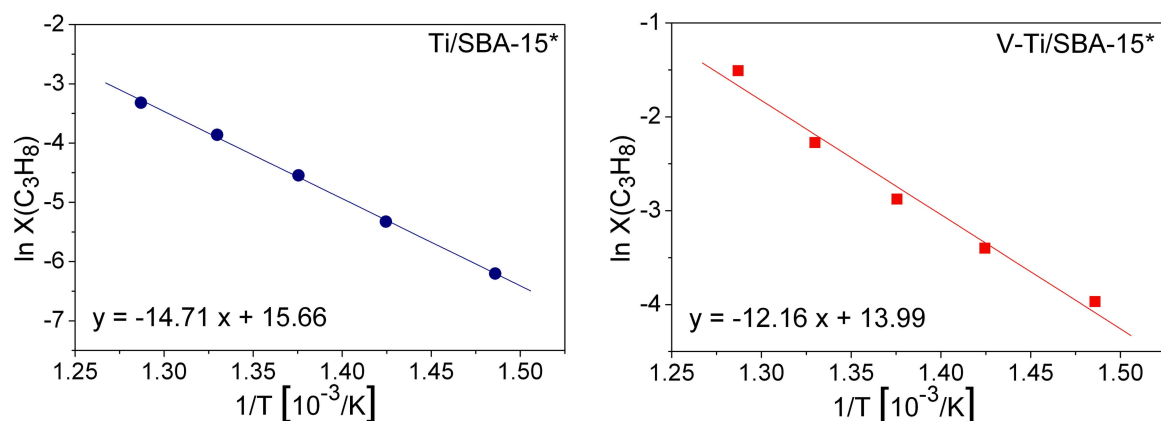


Figure 6.10: Arrhenius plot for calculation of activation energies of (●) Ti/SBA-15\* and (■) V-Ti/SBA-15\*

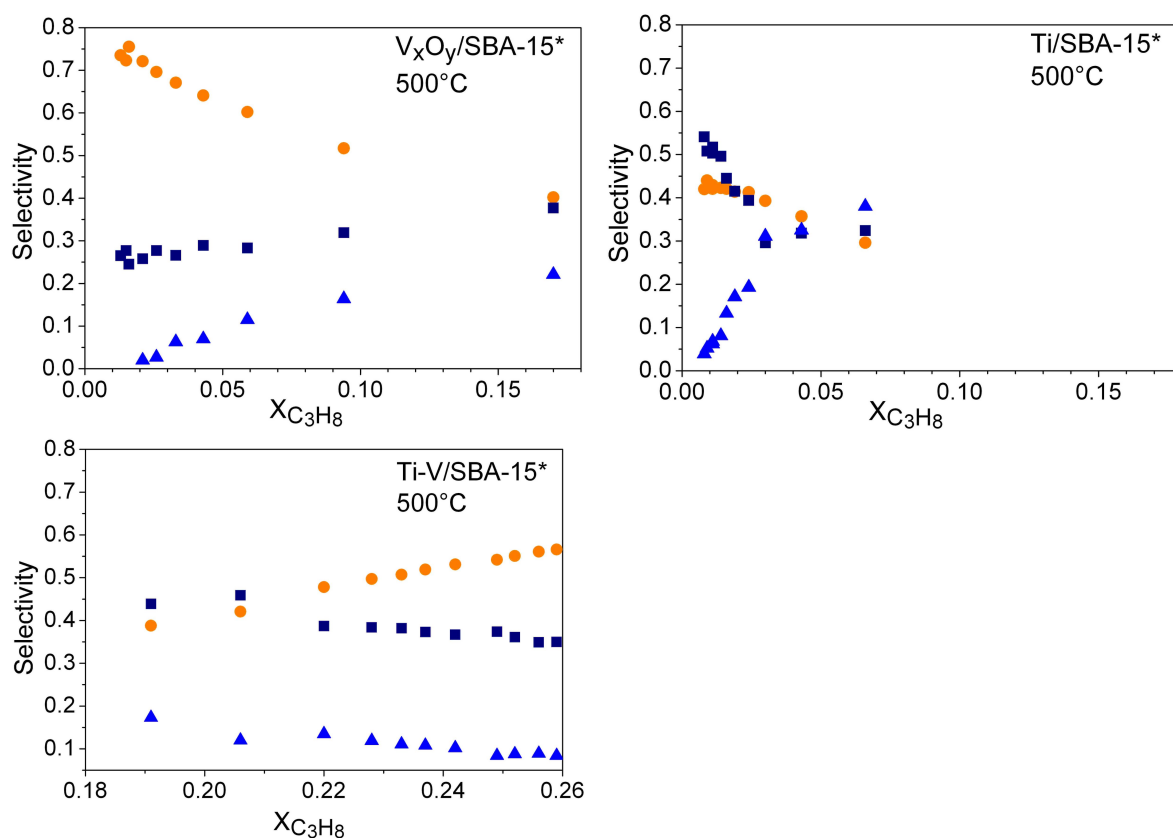


Figure 6.11: Selectivity towards (●)  $\text{C}_3\text{H}_6$ , (■) CO and (▲)  $\text{CO}_2$  of  $\text{V}_x\text{O}_y/\text{SBA-15}$ , Ti/SBA-15 and V-Ti/SBA-15

of propane ranged from 1 % to 12%. This shows that the behavior of V-Ti/SBA-15 at 500 °C is completely different from the one at 450 °C. Furthermore, the selectivities are quite different from each other. For the vanadia sample the selectivities towards propene are between 75% at 2% conversion and 40% at 17% conversion. Titanium only shows a selectivity of 42% at 2% conversion. Figure 6.12 shows selectivity towards propene of V-Ti/SBA-15 and  $V_xO_y$ /SBA-15\* at a temperature of 450 °C. Here, the V-Ti sample shows a selectivity of 64% at a conversion rate of 2%. The selectivity for  $V_xO_y$ /SBA-15\* at conversions smaller 5% is slightly higher, but comparable for the conversion range between 5% and 12%. Obviously, both samples behave similar at a temperature of 450 °C but completely different at 500 °C. This means that the titania influences the selectivity only at temperatures higher than 450 °C. Furthermore, the activation energy in the ODH of propane is reduced by the titania.

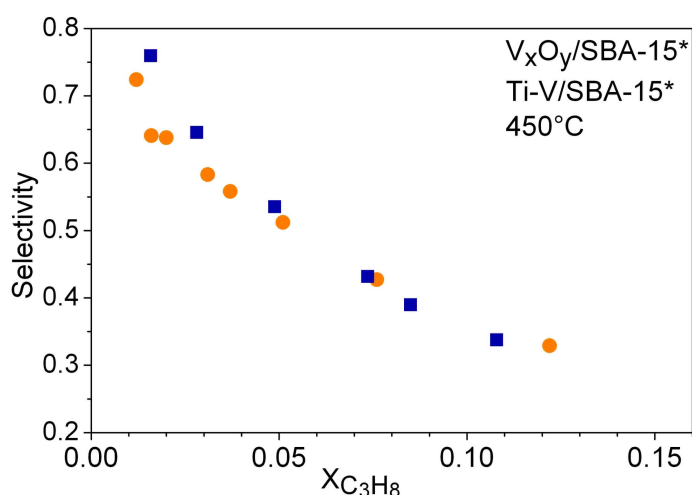


Figure 6.12: Selectivity towards  $C_3H_6$  of (●) Ti-V/SBA-15\*, (■)  $V_xO_y$ /SBA-15\*

## Conclusion

Spectroscopic characterization does not show any differences between  $V_xO_y$ /SBA-15\* and V-Ti/SBA-15 with regard to vanadia.

However, differences can be observed between Ti/SBA-15 and V-Ti/SBA-15 in Raman spectra and XP spectra. Raman spectroscopy shows the disappearance of the band at  $970\text{ cm}^{-1}$  for the sample containing titania and vanadia. The intensity observed for

the XPS V2p<sub>3/2</sub> peak of V-Ti/SBA-15 is higher than the one of Ti/SBA-15, especially at lower binding energies, which were assigned to octahedrally coordinated titania. By assigning Ti-OH stretch vibration as reason for the Raman band at 970 cm<sup>-1</sup> one can conclude that the vanadium reacts with the titania via OH groups followed by a transformation of some octahedrally coordinated titania sites. Further characterization should be done by varying the loading of the vanadium on Ti/SBA-15 in order to discriminate whether the vanadia is anchored via the titania or directly on the silica support.

In the ODH of propane, titanium influences the selectivity towards propene at temperatures higher than 450 °C, and obviously reduces the activation energy. A possible explanation can be the diffusion of V<sub>x</sub>O<sub>y</sub> from the silica surface to the titania at high temperatures, which is responsible for the significant increase in the conversion of propane. However, further investigations concerning conversions and selectivities at different reaction temperatures are required.



## 7 Conclusion and outlook

The subject of this study were investigations of silica-supported highly dispersed vanadia model catalysts with a vanadium loading of  $0.7 \text{ V atoms/nm}^2$  and their use in the partial oxidation of propane. The effects of synthesis methods (a multi-step synthesis with grafting and ion exchange and incipient wetness impregnation) and of two different silica supports (SBA-15 and Aerosil 300) have been described, as well as their catalytic results in the oxidative dehydrogenation (ODH) of propane. Furthermore, first results of a combination of titanium and vanadium supported by silica SBA-15 have been reported.

Investigation on the mechanical, thermal, and hydrothermal stability of blank SBA-15,  $\text{V}_x\text{O}_y/\text{SBA-15}$  (multi-step), and  $\text{V}_x\text{O}_y/\text{SBA-15}^*$  (incipient wetness) have shown for all treatments a significant increase of the stability of those samples synthesized according to the multi-step procedure. This effect of stabilization has been ascribed to the grafting of APTMS to the surface of SBA-15 resulting in a corona with higher density and consequently a higher stability of the pore walls. Raman spectroscopy has not shown any differences after mechanical treatment, which means that a change in the structure of the vanadia species during this process is not visible. DRUV-vis spectra for the same treatment indicate a higher degree of polymerization for the pressed samples. This effect is stronger for the incipient wetness impregnated sample than for the multi-step sample. The destruction of the mesoporous structure seems to lead to an increase in the degree of polymerization. This is probably due to the reduced BET surface area and consequently the space available for the vanadia.

In the oxidative dehydrogenation of propane, the pressed  $V_xO_y$ /SBA-15 synthesized by using the multi-step procedure displays a better performance than the pressed  $V_xO_y$ /SBA-15\* synthesized with incipient wetness impregnation. Selectivities are lower for both samples as compared to the untreated material. The reason for this are blocked vanadia sites occurring after mechanical treatment as has been shown by a correction of the reduced BET surface area.

Comparing the different synthesis methods and supports after pretreatment in oxygen at 350 °C, differences regarding curve shape, intensity and position related to the support materials were observed in DRUV-vis- and Raman spectra. Most prominently, the DRUV-vis spectra show a shift of the peak maxima to higher wavelengths for the samples supported on Aerosil 300. For the same samples, Raman spectra show a decrease of the ratio of the vanadyl band at 1027  $\text{cm}^{-1}$  and 1040  $\text{cm}^{-1}$ . Both characteristics can be interpreted as an increase of the degree of polymerization for vanadium on Aerosil 300.

Additionally, the synthesis method seems to influence the degree of polymerization, though only to a low degree. Less polymerized vanadia is created by using the multi-step method. Trends concerning an increase of the degree of polymerization can be stated in an order of  $V_xO_y$ /SBA-15  $\rightarrow$   $V_xO_y$ /SBA-15\*  $\rightarrow$   $V_xO_y$ /A300  $\rightarrow$   $V_xO_y$ /A300\*. The much more prominent influence of the support material can be explained with differences of the silica materials. As described in section 1.2.1, the type of silanol groups and their distribution is important for the reactivity of the material. The density of more reactive silanols seems to be lower with Aerosil 300, leading to a higher degree of polymerization of the vanadia.

TPR data show clear differences with regard to the synthesis method. The peak maxima appear at higher temperatures for the multi-step samples than for the incipient wetness samples. This trend is also evident in the average oxidation state and in the activation energies of the oxidative dehydrogenation of propane.

Assuming a correlation between structure, which in this case equals the degree in poly-



---

merization, and reactivity, one would equally expect a relation between the temperature maxima of reduction and activation energies and the degree of polymerization. However, TPR data show a difference between the support materials which could not be distinguished that clearly with spectroscopic methods. Nevertheless, the incipient wetness impregnated samples serve as a starting point to a higher degree of polymerization than the multi-step samples. We observed similar differences in temperature maxima and valences among the support materials.

For the oxidative dehydrogenation of propane, no significant changes were observed among the different support materials and/or synthesis methods with regard to both conversion and selectivity, although we observed differences in the vanadia structure as described above. This could lead to the assumption that during catalysis the vanadia structures of all samples converge to very similar ones. However, UV-vis spectroscopy of the samples before and after reaction shows differences.

Another more likely explanation could be that in each sample there are comparable species which are responsible for the ODH reaction, but that the spectroscopic data are dominated by those which are relevant for our purpose. This assumption directly leads to the question how these different species can be distinguished and how one can find out which of them are responsible for ODH reaction.

Another question arises from the fact that TPR data show clear differences at least between the respective support materials. TPR gives information about the reducibility of the catalyst. As a consequence, one would expect that this has an influence on the ODH reaction. There are differences in the activation energies of the samples but a clear correlation between both results is not observed. It is concluded that the gas phase composition has a strong influence on the reducibility. For a better comparison of TPR data and ODH reaction it would be useful to calculate activation energies by running TPR at different heating rates and/or recording TPR data with propane as a reduction gas.

In order to combine the high surface area of mesoporous silica with the catalytic

properties of  $V_2O_5/TiO_2$ , SBA-15 was covered by dispersed titania and doped with vanadia. In different spectroscopic characterization methods, we can observe crystalline  $TiO_2$  at a titanium density of 8.2 atoms/nm<sup>2</sup> supported on SBA-15. Up to a density of 3.1 titanium atoms/nm<sup>2</sup>, no crystallinity can be detected. DRUV-vis spectra can be interpreted as tetrahedrally coordinated titania with additional units bridging two  $TiO_6$  octahedra, forming Ti-O-Si-O-Ti structures and octahedrally coordinated titania in chains. With an increase in loading, the chains are growing until crystalline  $TiO_2$  is formed. Spectroscopic characterization does not show any differences between  $V_xO_y/SBA-15^*$  and V-Ti/SBA-15 with regard to vanadia. However, differences concerning the titanium can be observed in Raman spectra and XP spectra. From these data one can conclude that there is a reaction of vanadium with titania via OH groups, which is followed by a transformation of some octahedrally coordinated titania sites. Further characterization should be done by varying the loading of the vanadium on Ti/SBA-15 in order to find out whether the vanadia is actually anchored via the titania or directly on the silica support.

In the ODH of propane, titanium influences the selectivity towards propene at temperatures higher than 450 °C, and it obviously reduces the activation energy and reaction temperature. However, further investigations concerning conversions and selectivities at different reaction temperatures are required.

In an additional analysis of XPS data, we tried to obtain information about the structure, or, to be more precisely, about the oxidation states of vanadium in our samples. By the evaluation of difference spectra we found out that there are several species contributing to the O1s peak, which makes it difficult to have one particular oxygen species assigned to vanadium. Fitting results have shown that the oxidation states calculated are approximately in the expected range; however, they are not precise enough to obtain new information insights.

The aim of this study was to investigate the structure of vanadia supported on different

---

silica and synthesized with different methods and to analyze the structure in relation to the catalytic performance. We succeeded in pointing out that the synthesis method as well as the silica support has an influence on the vanadia structure. However, a correlation between structure and catalytic performance could not be clearly determined. In all our samples there seem to be minor amounts of species which are responsible for catalysis, but cannot be singled out. The challenge for future investigation would be to discriminate between species which are responsible for catalytic activity and those that are not responsible. From my point of view the next step in this direction is to find out which characterization method is to be preferred. Therefore in situ analysis for ODH of propane with different spectroscopic tools is necessary. If one can observe changes concerning species with different degrees of polymerization during reaction, one will be a step closer for discriminating the desired species.



# List of Figures

1.1	Dehydration process of silica SBA-15 observed by mass spectroscopy . . .	5
1.2	Scheme of several forms of silanol groups . . . . .	6
1.3	Effect of small pore radii and small particle sizes on the hydroxyl spacing <sup>[94]</sup> . . . . .	7
1.4	Structural motifs of surface vanadium oxide species proposed in literature	8
1.5	Correlation of structure and dispersion for silica SBA-15 supported vanadia <sup>[44]</sup> . . . . .	10
1.6	Schematic structural representation of hydrated $V_xO_y$ /SBA-15 <sup>[99]</sup> . . .	10
1.7	Schematic structural representation of dehydrated $V_xO_y$ /SBA-15 <sup>[99]</sup> . .	10
1.8	Propane oxidation pathways and calculated standard reaction enthalpies <sup>[63]</sup>	11
2.1	IUPAC classification of sorption isotherms <sup>[66]</sup> . . . . .	14
2.2	Nitrogen adsorption-desorption isotherm of well-ordered mesoporous silica SBA-15 . . . . .	16
2.3	IUPAC classification of hysteresis loops in sorption isotherms <sup>[66]</sup> . . . .	17
2.4	$\beta_s$ -plot of well-ordered mesoporous silica SBA-15 . . . . .	19
2.5	Bragg diffraction . . . . .	21
2.6	Geometry of hexagonal pores <sup>[31]</sup> . . . . .	22
2.7	Vacuum system ESCA . . . . .	23
2.8	ESCA set-up for combined Raman spectroscopy, XPS and DRUV-vis spectroscopy . . . . .	24

2.9	Interaction between primary electrons and the sample in electron microscopy <sup>[74]</sup> . . . . .	27
2.10	Schematic representation of vibrational Raman scattering . . . . .	30
2.11	Raman set-up . . . . .	31
2.12	<i>In situ</i> Raman cell . . . . .	32
3.1	Micelle structure for mesoporous silica <sup>[49]</sup> . . . . .	38
3.2	General scheme for self-assembly reaction of different surfactant and inorganic species <sup>[51]</sup> . . . . .	39
3.3	Scheme of silica supports and vanadium sources used . . . . .	41
3.4	Scheme of multi-step procedure . . . . .	41
4.1	Typical N <sub>2</sub> isotherm of SBA-15 with DFT pore size distribution . . . . .	46
4.2	Schematic representation of the organization of uncalcined SBA-15 materials <sup>[53]</sup> . . . . .	47
4.3	Pore model exhibiting a rough inner surface of mesoporous silica powders (schematically) hosting pyridine- <sup>15</sup> N <sup>[87]</sup> . . . . .	47
4.4	SEM image of SBA-15 particles . . . . .	48
4.5	TEM images of SBA-15 in cross sectional view (left) and longitudinal sectional view (right) . . . . .	48
4.6	Small-angle XRD of SBA-15 with magnification inset . . . . .	48
4.7	N <sub>2</sub> isotherm of Aerosil 300 with DFT pore size distribution . . . . .	49
4.8	SEM image of Aerosil 300 particles . . . . .	49
4.9	TEM images of Aerosil 300 . . . . .	49
4.10	N <sub>2</sub> Isotherms of blank SBA-15 after mechanical treatment at (a) 0 MPa, (b) 75 MPa, (c) 188 MPa, (d) 376 MPa, and (e) 752 MPa . . . . .	52
4.11	N <sub>2</sub> Isotherms of V <sub>x</sub> O <sub>y</sub> /SBA-15 after mechanical treatment at (a) 0 MPa, (b) 188 MPa, (c) 376 MPa, and (d) 752 MPa . . . . .	52

---

4.12 Comparison of data from this work after pressure treatment with literature data of Cassiers et al. <sup>[20]</sup> , Springuel-Huet et al. <sup>[91]</sup> , Hartman et al. <sup>[41]</sup> , and Chytil et al. <sup>[26]</sup> . . . . .	52
4.13 Small-angle XRD of blank SBA-15 after mechanical treatment at (a) 0 MPa, (b) 75 MPa, (c) 376 MPa, and (d) 752 MPa . . . . .	54
4.14 small-angle XRD of $V_xO_y$ /SBA-15 after mechanical treatment at (a) 0 MPa, (b) 188 MPa, (c) 376 MPa, and (d) 752 MPa . . . . .	54
4.15 Relative surface area and pore volume after mechanical treatment of blank SBA-15 and $V_xO_y$ /SBA-15 . . . . .	54
4.16 TEM picture after mechanical treatment of (a) blank SBA-15 at 0 MPa, (b) blank SBA-15 at 752 MPa, (c) $V_xO_y$ /SBA-15 at 752 MPa, and (d) $V_xO_y$ /SBA-15* at 752 MPa . . . . .	55
4.17 $N_2$ isotherms after mechanical treatment of (a) blank SBA-15 0 MPa, (b) $V_2O_5$ /SBA-15 at 752 MPa and (c) $V_xO_y$ /SBA-15* at 752 MPa . . . . .	56
4.18 $N_2$ isotherms after mechanical treatment of (a) $V_xO_y$ /SBA-15 at 0 MPa, (b) Oxa/SBA-15 at 752 MPa and (c) $V_xO_y$ /SBA-15 at 752 MPa . . . . .	56
4.19 Raman spectra before pressure treatment of (a) $V_xO_y$ /SBA-15, (c) $V_xO_y$ /SBA-15* and after pressure treatment at 752 MPa, (b) $V_xO_y$ /SBA-15, (d) $V_xO_y$ /SBA-15* and (e) blank SBA-15 . . . . .	57
4.20 DRUV-vis spectrum of $V_xO_y$ /SBA-15 (a) before pressure treatment and (b) after pressure treatment at 752 MPa . . . . .	59
4.21 DRUV-vis spectrum of $V_xO_y$ /SBA-15* (a) before pressure treatment and (b) after pressure treatment at 752 MPa . . . . .	59
4.22 DRUV-vis spectra of (a) $V_2O_5$ and (b) $NH_4VO_3$ . . . . .	59
4.23 $N_2$ isotherm of blank SBA-15 after thermal treatment at (a) 550 °C, (b) 650 °C, (c) 750 °C, (d) 850 °C, and (e) 1000 °C . . . . .	62
4.24 $N_2$ isotherm of modified SBA-15 after thermal treatment at (a) 550 °C, (b) 650 °C, (c) 750 °C, (d) 850 °C, and (e) 1000 °C . . . . .	62

4.25	Relative surface area and pore volume of blank SBA-15 and modified SBA-15 after thermal treatment . . . . .	62
4.26	N <sub>2</sub> isotherm of blank SBA-15 (a) before and (b) after hydrothermal treatment . . . . .	64
4.27	N <sub>2</sub> isotherm of modified SBA-15 (a) before and (b) after hydrothermal treatment . . . . .	64
4.28	Relative surface area and pore volume after hydrothermal treatment . .	64
4.29	N <sub>2</sub> isotherm and pore size distribution of (a) blank SBA-15, (b) V <sub>x</sub> O <sub>y</sub> /SBA-15* and (c) V <sub>x</sub> O <sub>y</sub> /SBA-15 . . . . .	67
4.30	N <sub>2</sub> isotherm and pore size distribution of (a) blank Aerosil 300, (b) V <sub>x</sub> O <sub>y</sub> /A300 and (c) V <sub>x</sub> O <sub>y</sub> /A300* . . . . .	67
4.31	β <sub>s</sub> -plots for micropore estimation of supported SBA-15 samples . . . . .	68
4.32	Raman spectra of (a) V <sub>x</sub> O <sub>y</sub> /SBA-15, (b) V <sub>x</sub> O <sub>y</sub> /SBA-15*, (c) V <sub>x</sub> O <sub>y</sub> /A300, (d) V <sub>x</sub> O <sub>y</sub> /A300*, (e) blank SBA-15 and (f) blank Aerosil 300 . . . . .	69
4.33	Raman spectra of the vanadyl band of (a) V <sub>x</sub> O <sub>y</sub> /SBA-15, (b) V <sub>x</sub> O <sub>y</sub> /SBA-15*, (c) V <sub>x</sub> O <sub>y</sub> /A300 and (d) V <sub>x</sub> O <sub>y</sub> /A300* . . . . .	69
4.34	DRUV-vis spectra of (a) V <sub>x</sub> O <sub>y</sub> /SBA-15, (b) V <sub>x</sub> O <sub>y</sub> /SBA-15*, (c) V <sub>x</sub> O <sub>y</sub> /A300 and (d) V <sub>x</sub> O <sub>y</sub> /A300* . . . . .	70
4.35	XP spectra (O1sV2p) of (a) V <sub>x</sub> O <sub>y</sub> /SBA-15, (b) V <sub>x</sub> O <sub>y</sub> /SBA-15*, (c) V <sub>x</sub> O <sub>y</sub> /A300 and (d) V <sub>x</sub> O <sub>y</sub> /A300* . . . . .	72
5.1	Selectivity towards propene at 500 °C before pressure treatment of (■) V <sub>x</sub> O <sub>y</sub> /SBA-15, (▲) V <sub>x</sub> O <sub>y</sub> /SBA-15* and after pressure treatment at 752 MPa of (□) V <sub>x</sub> O <sub>y</sub> /SBA-15, (△) V <sub>x</sub> O <sub>y</sub> /SBA-15* . . . . .	76
5.2	Conversion of propane at 500 °C before pressure treatment of (■) V <sub>x</sub> O <sub>y</sub> /SBA-15, (▲) V <sub>x</sub> O <sub>y</sub> /SBA-15* and after pressure treatment at 752 MPa of (□) V <sub>x</sub> O <sub>y</sub> /SBA-15, (△) V <sub>x</sub> O <sub>y</sub> /SBA-15* . . . . .	76



5.3	Conversion of propane before pressure treatment of (■) $V_xO_y/SBA-15$ , (▲) $V_xO_y/SBA-15^*$ and after pressure treatment at 752 MPa with BET surface area correction of (□) $V_xO_y/SBA-15$ , (△) $V_xO_y/SBA-15^*$ . . . . .	76
5.4	Influence of pretreatment for TPRO measurements focusing on $V_xO_y/SBA-15$ : (a) pretreatment in oxygen, (b) pretreatment in argon . . . . .	78
5.5	TPR of (a) $V_xO_y/SBA-15$ , (b) $V_xO_y/SBA-15^*$ , (c) $V_xO_y/A300$ and (d) $V_xO_y/A300^*$ . . . . .	79
5.6	Arrhenius plot for calculation of activation energies of (■) $V_xO_y/SBA-15$ , (●) $V_xO_y/SBA-15^*$ , (◆) $V_xO_y/A300$ , (▲) $V_xO_y/A300^*$ . . . . .	82
5.7	Selectivity towards propene at 500 °C of (■) $V_xO_y/SBA-15$ , (●) $V_xO_y/SBA-15^*$ , (◆) $V_xO_y/A300$ , (▲) $V_xO_y/A300^*$ . . . . .	83
5.8	Conversion of propane at 500 °C of (■) $V_xO_y/SBA-15$ , (●) $V_xO_y/SBA-15^*$ , (◆) $V_xO_y/A300$ , (▲) $V_xO_y/A300^*$ . . . . .	83
5.9	Selectivity towards (●) $C_3H_6$ , (■) CO and (▲) $CO_2$ of $V_xO_y/SBA-15$ , $V_xO_y/SBA-15^*$ , $V_xO_y/A300$ and $V_xO_y/A300^*$ at 500 °C . . . . .	84
5.10	UV-vis spectra (a) before and (b) after ODH of propane . . . . .	86
6.1	Raman spectra of (a) blank SBA-15, (b) 3wt% Ti/SBA-15, (c) 5wt% Ti/SBA-15, (d) 10wt% Ti/SBA-15, (e) 20wt% Ti/SBA-15 and (f) $TiO_2$ anatase . . . . .	91
6.2	Raman spectra of (a) blank SBA-15, (b) 3wt% Ti/SBA-15, (c) 5wt% Ti/SBA-15 and (d) 10wt% Ti/SBA-15 . . . . .	91
6.3	DRUV-vis spectra of (a) 3wt% Ti/SBA-15, (b) 5wt% Ti/SBA-15, (c) 10wt% Ti/SBA-15 and (d) 20wt% Ti/SBA-15 . . . . .	92
6.4	Ti2p XP spectra of (a) 3 wt% Ti/SBA-15, (b) 5 wt% Ti/SBA-15, (c) 10 wt% Ti/SBA-15, (d) 20 wt% Ti/SBA-15 and (e) $TiO_2$ anatase . . . . .	94
6.5	O1s XP spectra of (a) 3 wt% Ti/SBA-15, (b) 5 wt% Ti/SBA-15, (c) 10 wt% Ti/SBA-15, (d) 20 wt% Ti/SBA-15 and (e) $TiO_2$ anatase . . . . .	94

6.6	Raman spectra of (a) Ti/SBA-15 ( <i>asis</i> ), (b) V-Ti/SBA-15 ( <i>asis</i> ) and (c) V-Ti/SBA-15 ( <i>pretreated</i> ) . . . . .	96
6.7	DRUV-vis spectra of (a) Ti/SBA-15 and (b) V-Ti/SBA-15 . . . . .	97
6.8	O1sV2p XP spectra of (a) Ti/SBA-15 and (b) V-Ti/SBA-15 . . . . .	97
6.9	Ti2p XP spectra of (a) Ti/SBA-15 and (b) V-Ti/SBA-15 . . . . .	97
6.10	Arrhenius plot for calculation of activation energies of (●) Ti/SBA-15* and (■) V-Ti/SBA-15* . . . . .	99
6.11	Selectivity towards (●) C <sub>3</sub> H <sub>6</sub> , (■) CO and (▲) CO <sub>2</sub> of V <sub>x</sub> O <sub>y</sub> /SBA-15, Ti/SBA-15 and V-Ti/SBA-15 . . . . .	99
6.12	Selectivity towards C <sub>3</sub> H <sub>6</sub> of (●) Ti-V/SBA-15*, (■) V <sub>x</sub> O <sub>y</sub> /SBA-15* . . .	100

# List of Tables

1.1	Selected industrial catalytic processes using vanadium oxides <sup>[100]</sup> . . . . .	3
4.1	BET surface area and pore volume of silica supports used . . . . .	46
4.2	BET surface area and pore volume of blank SBA-15 and $V_xO_y$ /SBA-15 after mechanical treatment . . . . .	51
4.3	BET surface area and pore volume of blank SBA-15 and modified SBA- 15 after thermal treatment . . . . .	61
4.4	BET surface area and pore volume of blank SBA-15 and modified SBA- 15 after hydrothermal treatment . . . . .	63
4.5	XPS: fitted areas of $V2p_{3/2}$ peaks . . . . .	73
5.1	TPR temperature maxima, valences provided by TPR data and activa- tion energies provided by ODH of propane . . . . .	81
6.1	BET surface area and pore volume of Ti/SBA-15 with several loadings	90
6.2	BET surface area and pore volume of Ti/SBA-15 and V-Ti/SBA-15 . .	95
6.3	Activation energies for ODH of propane . . . . .	98



# Bibliography

- [1] *NIST XPS Database*, 2008. <http://srdata.nist.gov/xps/>.
- [2] M. ALBA, Z. LUAN, AND J. KLINOWSKI, *Titanosilicate Mesoporous Molecular Sieve MCM-41: Synthesis and Characterization*, *J. Phys. Chem.*, 100 (1996), p. 2178.
- [3] J. ANDERSON AND K. PRATT, eds., *Introduction to Characterization and Testing of Catalysts*, Academic Press Australia, 1985.
- [4] F. ARENA, F. FRUSTERI, G. MARTRA, S. COLUCCIA, AND A. PARMALIANA, *Surface structures, reduction pattern and oxygen chemisorption of  $V_2O_5/SiO_2$  catalysts*, *J. Chem. Soc., Faraday Trans.*, 93 (1997), p. 3849.
- [5] T. ARMAROLI, G. BUSCA, F. MILELLA, F. BREGANI, G. TOLEDO, A. NAS-TROAND, P. D. LUCA, G. BAGNASCOD, AND M. TURCO, *A Study of ETS-4 Molecular Sieves and of Their Adsorption of Water and Ammonia*, *J. Mater. Chem.*, 10 (2000), p. 1699.
- [6] E. ASTORINO, J. PERI, R. WILLEY, AND G. BUSCA, *Spectroscopic Characterization of Silicalite-1 and Titanium Silicalite-1*, *J. Catal.*, 157 (1995), p. 482.
- [7] V. AVDEEV AND G. ZHIDOMIROV, *Modeling the Active Centers of  $V_2O_5/SiO_2$  and  $V_2O_5/TiO_2$  Supported Catalysts. DFT Theoretical Analysis of Optical Properties*, *J. Struct. Chem.*, 46 (2005), p. 577.

- [8] M. BALTES, K. CASSIERS, P. V. D. VOORT, B. M. WECKHUYSEN, R. SCHOONHEYDT, AND E. VANSANT, *MCM-48-Supported Vanadium Oxide Catalysts, Prepared by the Molecular Designed Dispersion of VO(acac)<sub>2</sub>: A Detailed Study of the Highly Reactive MCM-48 Surface and the Structure and Activity of the Deposited VO<sub>x</sub>*, *J. Catal.*, 197 (2001), p. 160.
- [9] E. BARRETT, L. JOYNER, AND P. HALENDA, *The Determination of Pore Volume and Area Distributions in Porous Substances. I. Computations from Nitrogen Isotherms*, *J. Am. Chem. Soc.*, 73 (1951), p. 373.
- [10] C. BARTHOLOMEW AND R. FARRAUTO, eds., *Fundamentals of Industrial Catalytic Processes*, Wiley, New Jersey, 2005, ch. 2.
- [11] R. BAUMANN, ed., *Absorption Spectroscopy*, Wiley New York, 1962.
- [12] H. BERNDT, A. MARTIN, A. BRUECKNER, E. SCHREIER, D. MUELLER, H. KOSSLICK, G.-U. WOLF, AND B. LUECKE, *Structure and Catalytic Properties of VO<sub>x</sub>/MCM Materials for the Partial Oxidation of Methane to Formaldehyde*, *J. Catal.*, 191 (2000), p. 384.
- [13] A. BIELANSKI AND J. HABER, *Oxygen in catalysis*, Dekker New York, 1991.
- [14] E. BORELLO, C. LAMBERTI, S. BORDIGA, A. ZECCHINA, AND C. O. AREAN, *Quantum-Size Effects in the Titanosilicate Molecular Sieve*, *Appl. Phys. Lett.*, 71 (1997), p. 2319.
- [15] Y. BORODKO, J. AGER, G. MARTI, H. SONG, K. NIESZ, AND G. SOMORJAI, *Structure Sensitivity of Vibrational Spectra of Mesoporous Silica SBA-15 and Pt/SBA-15*, *J. Phys. Chem. B*, 109 (2005), p. 17386.
- [16] D. BRIGGS AND M. SEAH, eds., *Practical Surface Analysis by Auger and X-ray Photoelectron Spectroscopy*, Wiley Chichester, 1983.

- [17] J. BRONKEMA AND A. BELL, *Mechanistic Studies of Methanol Oxidation to Formaldehyde on Isolated Vanadate Sites Supported on MCM-48*, J. Phys. Chem. C, 111 (2007), p. 420.
- [18] S. BRUNAUER, P. EMMET, AND E. TELLER, *Adsorption of Gases in Multimolecular Layers*, J. Am. Chem. Soc., 60 (1938), p. 309.
- [19] G. CALLEJA, R. VAN GRIEKEN, R. GARCIA, J. MELERO, AND J. IGLESIAS, *Preparation of Titanium Molecular Species Supported on Mesoporous Silica by Different Grafting Methods*, J. Mol. Catal. A: Chemical, 182-183 (2002), p. 215.
- [20] K. CASSIERS, T. LINSEN, AND M. MATHIEU, *A Detailed Study of Thermal, Hydrothermal, and Mechanical Stabilities of a Wide Range of Surfactant Assembled Mesoporous Silicas*, Chem. Mater., 14 (2002), p. 2317.
- [21] M. CAVALLERI, K. HERMANN, A. KNOP-GERICKE, M. HÄVECKER, R. HERBERT, C. HESS, A. OESTERREICH, J. DÖBLER, AND R. SCHLÖGL, *Identification of Silica-Supported Vanadia by X-ray Absorption Spectroscopy: Combined Theoretical and Experimental Studies*, submitted to J. Catal., (2008).
- [22] G. CENTI, F. CAVANTI, AND F. TRIFIRO, eds., *Selective Oxidation by Heterogeneous Catalysis*, Kluwer Academic / Plenum Publishers, New York, 2001.
- [23] M. CHAAR, H. KUNG, AND M. KUNG, *Selective oxidative dehydrogenation of butane over V-Mg-O catalysts*, J. Catal., 105 (1987), p. 483.
- [24] M. CHAAR, D. PATEL, AND H. KUNG, *Selective Oxidative Dehydrogenation of Propane over V-Mg-O Catalysts*, J. Catal., 109 (1988), p. 463.
- [25] K. CHEN, A. BELL, AND E. IGLESIA, *The Relationship between the Electronic and Redox Properties of Dispersed Metal Oxides and Their Turnover Rates in Oxidative Dehydrogenation Reactions*, J. Catal., 209 (2002), p. 35.

- [26] S. CHYTIL, L. HAUGLAND, AND E. BLEKKAN, *On the Mechanical Stability of Mesoporous Silica SBA-15*, *Microp. Mesop. Mater.*, 111 (2008), p. 134.
- [27] S. CONTARINI, P. VAN DER HEIDE, A. PRAKASH, AND L. KEVAN, *Titanium Coordination in Microporous and Mesoporous Oxide Materials by Monochromated X-ray Photoelectron Spectroscopy and Auger Electron Spectroscopy*, *J. Elect. Spect. Rel. Phen.*, 125 (2002), p. 25.
- [28] A. CORMA, M. CAMBLOR, P. ESTEVE, A. MATRINEZ, AND J. PEREZ-PARIENTE, *Activity of Ti-Beta Catalyst for Selective Oxidation of Alkenes and Alkanes*, *J. Catal.*, 145 (1994), p. 151.
- [29] N. DAS, H. ECKERT, H. HU, I. WACHS, J. WALZER, AND F. FEHER, *Bonding States of Surface Vanadium( V) Oxide Phases on Silica: Structural Characterization by  $^{51}\text{V}$  NMR and Raman Spectroscopy*, *J. Phys. Chem.*, 97 (1993), p. 8240.
- [30] V. FORNES, C. LOPEZ, H. LOPEZ, AND A. MARTINEZ, *Catalytic Performance of Mesoporous  $\text{VO}_x/\text{SBA-15}$  Catalysts for the Partial Oxidation of Methane to Formaldehyde*, *Appl. Catal. A: General*, 249 (2003), p. 345.
- [31] A. GALARNEAU, D. DESPLANTIER, R. DUTARTRE, AND F. D. RENZO, *Micelle-templated Silicates as a Test Bed for Methods of Mesopore Size Evaluation*, *Microp. Mesop. Mater.*, 27 (1999), p. 297.
- [32] A. GALERNAU, H. CAMBON, F. D. RENZO, AND F. FAJULA, *True Microporosity and Surface Area of Mesoporous SBA-15 Silicas as a Function of Synthesis Temperature*, *Langmuir*, 17 (2001), p. 8328.
- [33] X. GAO, S. BARE, AND I. WACHS, *In Situ Spectroscopic Investigation of Molecular Structures of Highly Dispersed Vanadium Oxide on Silica under Various Conditions*, *J. Phys. Chem. B*, 102 (1998), p. 10842.



- 
- [34] X. GAO, P. RUIZ, Q. XIN, X. GUO, AND B. DELMON, *Effect of Coexistence of Magnesium Vanadate Phases in the Selective Oxidation of Propane to Propene*, J. Catal., 148 (1994), p. 56.
- [35] X. GAO AND I. WACHS, *Titania-Silica as Catalysts: Molecular Structural Characteristics and Physico-Chemical Properties*, Catal. Today, 51 (1999), p. 233.
- [36] F. GEOBALDO, S. BORDIGA, A. ZECCHINA, E. GIAMELLO, G. LEOFANTI, AND G. PETRINI, *DRS UV-Vis and EPR Spectroscopy of Hydroperoxo and Superoxo Complexes in Titanium Silicalite*, Catal. Lett., 16 (1992), p. 109.
- [37] S. GREGG AND K. SING, *Adsorption, Surface Area and Porosity*, Academic Press London, 1982.
- [38] W. GUO, X. LI, AND X. ZHAO, *Understanding the Hydrothermal Stability of Large-Pore Periodic Mesoporous Organosilicas and Pure Silicas*, Microp. Mesop. Mater., 93 (2006), p. 285.
- [39] W. HANKE, R. BIENERT, AND H.-G. JERSCHKEWITZ, *Untersuchungen an katalytisch aktiven Oberflächenverbindungen: I. Herstellung und Untersuchung von Vanadinoxide-Phasen auf SiO<sub>2</sub>*, Z. anorg. allg. Chem., 414 (1975), p. 109.
- [40] D. HARRIS AND M. BERTOLUCCI, *Symmetry and Spectroscopy: An Introduction to Vibrational and Electronic Spectroscopy*, Dover, 1989, p. 94.
- [41] M. HARTMANN AND A. VINU, *Mechanical Stability and Porosity Analysis of Large-Pore SBA-15 Mesoporous Molecular Sieves by Mercury Porosimetry and Organics Adsorption*, Langmuir, 18 (2002), p. 8010.
- [42] C. HESS, *Characterization of the Synthesis and Reactivity Behavior of Nanostructured Vanadia Model Catalysts Using XPS and Vibrational Spectroscopy*, Surf. Sci., 600 (2006), p. 3695.

- [43] —, *Direct Correlation of the Dispersion and Structure in Vanadium Oxide Supported on Silica SBA-15*, *J. Catal.*, 248 (2007), p. 120.
- [44] —, *Synthesis, Characterization and Application of Nanostructured Vanadia Model Catalysts for Partial Oxidation Reaction*, Habilitation an der Humboldt-Universität Berlin, 2008.
- [45] C. HESS, J. HOEFELMEYER, AND T. TILLEY, *Spectroscopic Characterization of Highly Dispersed Vanadia Supported on SBA-15*, *J. Phys. Chem. B*, 108 (2004), p. 9703.
- [46] C. HESS AND R. SCHLÖGL, *The Influence of Water on the Dispersion of Vanadia Supported on Silica SBA-15*, *Chem. Phys. Lett.*, 432 (2006), p. 139.
- [47] C. HESS, G. TZOLOVA-MÜLLER, AND R. HERBERT, *The Influence of Water on the Dispersion of Vanadia Supported on Silica SBA-15: A Combined XPS and Raman Study*, *J. Phys. Chem. C*, 111 (2007), p. 9471.
- [48] C. HESS, U. WILD, AND R. SCHLOEGL, *The Mechanism for the Controlled Synthesis of Highly Dispersed Vanadia Supported on Silica SBA-15*, *Microp. Mesop. Mater.*, 95 (2006), p. 339.
- [49] B. HODNETT, ed., *Heterogeneous Catalytic Oxidation*, John Wiley & Sons, LTD, Chichester, 2000.
- [50] I. HORVATH, ed., *Encyclopedia of Catalysis*, vol. 3, Wiley-Interscience, New Jersey, 2003, pp. 49–79.
- [51] Q. HUO, D. MARGOLESE, U. CIESLA, P. FENG, T. GIER, P. SIEGER, R. LEON, P. PETROFF, F. SCHÜTH, AND G. STUCKY, *Generalized Synthesis of Periodic Surfactant / Inorganic Composite Materials*, *Lett. Nature*, 368 (1994), p. 317.

- 
- [52] R. IHLER, *The Colloid Chemistry of Silica and Silicates*, Cornell University Press, Ithaca, New York, 1955, ch. VI.
- [53] M. IMPEROR-CLERC, P. DAVIDSON, AND A. DAVIDSON, *Existence of a Microporous Corona around the Mesopores of Silica-Based SBA-15 Materials Templated by Triblock Copolymers*, *J. Am. Chem. Soc.*, 122 (2000), p. 11925.
- [54] J. JANSEN, M. STÖCKER, H. KARGE, AND J. WEITKAMP, eds., *Advanced Zeolite Science and Applications*, vol. 85 of *Studies In Surface Science and Catalysis*, Elsevier Amsterdam, 1994, pp. 177–213.
- [55] B. JONSON, B. REBENSTROF, R. LARSSON, AND S. ANDERSSON, *Activity Measurements and Spectroscopic Studies of the Catalytic Oxidation of Toluene over Silica-Supported Vanadium Oxides*, *J. Chem. Soc., Faraday Trans.*, 84 (1988), p. 1897.
- [56] E. KONDRATENKO, M. CHERIAN, AND M. BAERNS, *Oxidative Dehydrogenation of Propane over Differently Structured Vanadia-Based Catalysts in the Presence of  $O_2$  and  $N_2O$* , *Catal. Today*, 112 (2006), p. 60.
- [57] H. KUNG AND M. KUNG, *Oxidative Dehydrogenation of Alkanes over Vanadium-Magnesium-Oxides*, *Appl. Catal. A: General*, 157 (1997), p. 105.
- [58] P. KUSTROWSKI, Y. SEGURA, L. CHMIELARZ, J. SURMAN, R. DZIEMBAJ, P. COOL, AND E. VANSANT,  *$VO_x$  Supported SBA-15 Catalysts for the Oxidative Dehydrogenation of Ethylbenzene to Styrene in the Presence of  $N_2O$* , *Catal. Today*, 114 (2006), p. 307.
- [59] J. KWAK, J. HERRERA, J. HU, Y. WANG, AND C. PEDEN, *A New Class of Highly Dispersed  $VO_x$  Catalysts on Mesoporous Silica: Synthesis, Characterization, and Catalytic Activity in the Partial Oxidation of Ethanol*, *Appl. Catal. A: General*, 300 (2006), p. 109.

- [60] J. LEE AND S. OYAMA, *Oxidative Coupling of Methane to Higher - Hydrocarbons*, Catal. Rev.-Sci. Eng., 30 (1988), p. 249.
- [61] O. LEVENSPIEL, ed., *Chemical Reaction Engineering: An Introduction to The Design of Chemical Reactors*, Wiley New York, 1964.
- [62] X.-K. LI, W.-J. JI, J. ZHAO, Z. ZHANG, AND C.-T. AU, *A Comparison Study on the Partial Oxidation of n-Butane and Propane over VPO Catalysts Supported on SBA-15, MCM-41, and Fumed SiO<sub>2</sub>*, Appl. Catal. A: General, 306 (2006), p. 8.
- [63] M. LIN, *Selective Oxidation of Propane to Acrylic Acid with Molecular Oxygen*, Appl. Catal. A: General, 207 (2001), p. 1.
- [64] Y.-M. LIU, Y. CAO, AND K.-N. FAN, *Vanadium Oxide Supported on Mesoporous SBA-15 as Highly Selective Catalysts in the Oxidative Dehydrogenation of Propane*, J. Catal., 224 (2004), p. 417.
- [65] Y.-M. LIU, W.-L. FENG, T.-C. LI, H.-Y. HE, W.-L. DAI, W. HUANG, Y. CAO, AND K.-N. FAN, *Structure and Catalytic Properties of Vanadium Oxide Supported on Mesocellulose Silica Foams (MCF) for the Oxidative Dehydrogenation of Propane to Propylene*, J. Catal., 239 (2006), p. 125.
- [66] S. LOWELL, J. SHIELDS, AND M.A. THOMAS, eds., *Characterization of Porous Solids and Powders: Surface Area, Pore Size and Density*, Kluwer Academic Publishers, Dordrecht / Boston / London, 2004, ch. 4.
- [67] Z. LUAN, E. M. MAES, P. A. W. VAN DER HEIDE, D. ZHAO, R. S. CZERNUSZEWICZ, AND L. KEVAN, *Incorporation of Titanium into Mesoporous Silica Molecular Sieve SBA-15*, Chem. Mater., 11 (1999), p. 3680.
- [68] Z. LUAN, P. MELONI, R. CZERNUSZEWICZ, AND L. KEVAN, *Raman Spectroscopy of Vanadium Oxide Species Immobilized at Surface Titanium Centers*

- of Mesoporous Titanosilicate TiMCM-41 Molecular Sieves, *J. Phys. Chem. B*, 101 (1997), p. 9046.
- [69] W. LUKENS, J. SCHMIDT-WINKEL, D. ZHAO, J. FENG, AND G. STUCKY, *Evaluating Pore Sizes in Mesoporous Materials: A Simplified Standard Adsorption Method and a Simplified Broekhoff-de Boer Method*, *Langmuir*, 15 (1999), p. 5403.
- [70] N. MAGG, B. IMMARAPORN, J. GIORGI, T. SCHROEDER, M. BAEUMER, J. DOEBLER, Z. WU, E. KONDRATENKO, M. CHERIAN, M. BAERNS, P. STAIR, J. SAUER, AND H.-J. FREUND, *Vibrational Spectra of Alumina- and Silica-Supported Vanadia Revisited: An Experimental and Theoretical Model Catalyst Study*, *J. Catal.*, 226 (2004), p. 88.
- [71] P. MARS AND D. VAN KREVELEN, *Oxidations carried out by means of vanadium oxide catalysts*, *Chem. Eng. Sci.*, 3 (1954), p. 41.
- [72] A. MCNAUGHT AND A. WILKINSON, eds., *IUPAC Compendium of Chemical Terminology*, The Gold Book, Second Edition, Blackwell Science, 1997.
- [73] J. MOULDER, W. STICKLE, P. SOBOL, AND K. BOMBEN, eds., *Handbook of X-ray Photoelectron Spectroscopy*, Perkin-Elmer Corporation, 1992.
- [74] J. NIEMANTSVERDRIET, ed., *Spectroscopy in Catalysis: An Introduction*, Wiley-VCH Weinheim, 2 ed., 2000.
- [75] J. M. L. NIETO, *The Selective Oxidative Activation of Light Alkanes. From Supported Vanadia to Multicomponent Bulk V-Containing Catalysts*, *Top. Catal.*, 41 (2006), p. 3.
- [76] O. OVSITSER, M. CHERIAN, AND E. KONDRATENKO, *In-Situ UV-vis and Transient Isotopic Analysis of the Role of Oxidizing Agent in the Oxidative Dehydrogenation of Propane over Silica-Supported Vanadia Catalysts*, *J. Phys. Chem. C*, 111 (2007), p. 8594.

- [77] S. OYAMA, G. WENT, K. LEWIS, A. BELL, AND G. SOMORJAI, *Oxygen Chemisorption and Laser Raman Spectroscopy of Unsupported and Silica-Supported Vanadium Oxide Catalysts*, J. Phys. Chem., 93 (1989), p. 6786.
- [78] M. PENA, A. DEJOZ, V. FORNES, F. REY, M. VAZQUEZ, AND J. L. NIETO, *V-Containing MCM-41 and MCM-48 catalysts for the selective oxidation of propane in gas phase*, Appl. Catal. A: General, 209 (2001), p. 155.
- [79] P. RAVIKOVITCH, G. HALLER, AND A. NEIMARK, *Density Functional Theory Model for Calculating Pore Size Distributions: Pore Structure of Nanoporous Catalysts*, Adv. Coll. Interf. Sci., 76-77 (1998), p. 203.
- [80] J. ROCHA AND M. ANDERSON, *Microporous Titanosilicates and other Novel Mixed Octahedral-Tetrahedral Framework Oxides*, Eur. J. Inorg. Chem., (2000), p. 801.
- [81] P. ROMAN, A. ARANZABE, AND A. LUQUE, *Preparation and Solid State Characterization of Some Alkylammonium Decavanadates. Crystal Structure of the Hexakis(*n*-Hexylammonium) Decavanadate Dihydrate*, Mater. Res. Bull., 26 (1991), p. 731.
- [82] S. RUTHSTEIN, V. FRYDMAN, S. KABABYA, M. LANDAU, AND D. GOLDFARB, *Study of the Formation of the Mesoporous Material SBA-15 by EPR Spectroscopy*, J. Phys. Chem. B, 107 (2003), p. 1739.
- [83] D. S. H. SAM, V. SOENEN, AND J. VOLTA, *Oxidative Dehydrogenation of Propane over V-Mg-O Catalysts*, J. Catal., 123 (1990), p. 417.
- [84] M. SCHRAML-MARTH, A. WOKAUN, M. POHL, AND H.-L. KRAUSS, *Spectroscopic Investigation of the Structure of Silica-supported Vanadium Oxide Catalysts at Submonolayer Coverages*, J. Chem. Soc., Faraday Trans., 87 (1991), p. 2635.

- 
- [85] Y. SEGURA, L. CHMIELARZ, P. KUSTROWSKI, P. COOL, R. DZIEMBAJ, AND E. VANSANT, *Preparation and Characterization of Vanadium Oxide Deposited on Thermally Stable Mesoporous Titania*, J. Phys. Chem. B, 110 (2006), p. 948.
- [86] Y. SEGURA, P. COOL, P. KUSTROWSKI, L. CHMIELARZ, R. DZIEMBAJ, AND E. VANSANT, *Characterization of Vanadium and Titanium Oxide Supported SBA-15*, J. Phys. Chem. B, 109 (2005), p. 12071.
- [87] I. SHENDEROVICH, G. BUNTKOWSKY, A. SCHREIBE, E. GEDAT, S. SHARIF, J. ALBRECHT, N. GOLUBEV, G. FINDENEGG, AND H.-H. LIMBACH, *Pyridine-15N - A Mobile NMR Sensor for Surface Acidity and Surface Defects of Mesoporous Silica*, J. Phys. Chem. B, 107 (2003), p. 11924.
- [88] V. SOKOLOVSKI, *Principles of Oxidative Catalysis on Solid Oxides*, Catal. Rev.-Sci. Eng., 32 (1990), p. 1.
- [89] C. SONWANE AND P. LUDOVICE, *A Note on Micro- and Mesopores in the Walls of SBA-15 and Hysteresis of Adsorption Isotherms*, J. Mol. Catal. A: Chemical, 238 (2005), p. 135.
- [90] A. SOULT, D. CARTER, H. SCHREIBER, L. VAN DE BURGT, AND A. STIEGMAN, *Spectroscopy of Amorphous and Crystalline Titania-Silica Materials*, J. Phys. Chem. B, 106 (2002), p. 9266.
- [91] M. SPRINGUEL-HUET, J.-L. BONARDET, AND A. GEDEON, *Mechanical Properties of Mesoporous Silicas and Alumina-Silicas MCM-41 and SBA-15 Studied by N<sub>2</sub> Adsorption and <sup>129</sup>Xe NMR*, Microp. Mesop. Mater., 44-45 (2001), p. 775.
- [92] A. TAGUCHI AND F. SCHUETH, *Ordered Mesoporous Materials in Catalysis*, Microp. and Mesop. Mater., 77 (2005), p. 1.
- [93] P. T. TANEV, M. CHIBWE, AND T. J. PINNAVAIA, *Titanium-containing Mesoporous Molecular Sieve for Catalytic Oxidation of Aromatic Compounds*, Nature, 368 (1994), p. 321.

- [94] E. VANSANT, P. VAN DER VOORT, AND K. VRANKEN, *Characterization and Chemical Modification of the Silica Surface*, in *Studies in Surface Science and Catalysis*, B. Delmon and J.T.Yates, eds., vol. 93, Elsevier, 1995, ch. 3.
- [95] J. VEDRINE, G. COUDURIER, AND J. MILLET, *Molecular Design of Active Sites in Partial Oxidation Reactions on Metallic Oxides*, *Catal. Today*, 33 (1997), p. 3.
- [96] J. VEDRINE, J. MILLET, AND J. VOLTA, *Molecular Description of Active Sites in Oxidation Reactions: Acid-base and Redox Properties, and Role of Water*, *Catal. Today*, 32 (1996), p. 115.
- [97] T. VENKOV, C. HESS, AND F. JENTOFT, *Redox Properties of Vanadium Ions in SBA-15-Supported Vanadium Oxide: An FTIR Spectroscopic Study*, *Langmuir*, 23 (2007), p. 1768.
- [98] L. VRADMAN, L. TITELMAN, AND M. HERSKOWITZ, *Size Effect on SBA-15 Microporosity*, *Microp. Mesop. Mater.*, 93 (2006), p. 313.
- [99] A. WALTER, R. HERBERT, C. HESS, AND T. RESSLER, *The Structural Characterization of Vanadium Oxide Catalysts Supported on Nanoporous SiO<sub>2</sub> Using X-ray Absorption Spectroscopy*, in preparation, (2008).
- [100] B. WECKHUYSEN AND D. KELLER, *Chemistry, Spectroscopy and the Role of Supported Vanadium Oxides in Heterogeneous Catalysis*, *Catal. Today*, 78 (2003), p. 25.
- [101] H. WENNERSTROM AND S. LIDIN, *Scientific Background on the Nobel Prize in Chemistry 2007: Chemical Process on Solid Surfaces*, 2007. <http://www.kva.se>.
- [102] C.-M. YANG, B. ZIBROWIUS, W. SCHMIDT, AND F. SCHÜTH, *Consecutive Generation of Mesopores and Micropores in SBA-15*, *Chem. Mater.*, 15 (2003), p. 3739.



- [103] F. ZHANG, Y. YAN, H. YANG, Y. MENG, C. YU, B. TU, AND D. ZHAO, *Understanding Effect of Wall Structure on the Hydrothermal Stability of Mesoporous Silica SBA-15*, J. Phys. Chem. B, 109 (2005), p. 8723.
- [104] D. ZHAO, J. FENG, AND G. STUCKY, *Triblock Copolymer Syntheses of Mesoporous Silica with Periodic 50 to 300 Angstrom Pores*, Science, 279 (1998), p. 548.
- [105] D. ZHAO, Q. HUO, J. FENG, B. CHMELKA, AND G. STUCKY, *Nonionic Triblock and Star Diblock Copolymer and Oligomeric Surfactant Syntheses of Highly Ordered, Hydrothermally Stable, Mesoporous Silica Structures*, J. Am. Chem. Soc., 120 (1998), p. 6024.

## *Bibliography*

---

# A Appendix

## A.1 Curriculum Vitae

Name: Rita Herbert  
Geburtsdatum/-ort: 25.10.1979 in Berlin  
Staatsangehörigkeit: deutsch

### Ausbildung

09/1993 - 06/1999	Friedrich-Dessauer-Gymnasium in Aschaffenburg
10/1999 - 12/2004	Studium der Verfahrenstechnik an der TU Dresden
06/2001 - 04/2005	Stipendiatin der Stiftung der Deutschen Wirtschaft (sdw)
09/2003 - 09/2003	BASF Ferienkurs für Ingenieure
04/2004 - 09/2004	Diplomarbeit an der University of New South Wales, Sydney, Australien gefördert durch die Ernest-Solvay-Stiftung
Seit 01/2005	Promotion am Fritz-Haber-Institut der Max-Planck-Gesellschaft in Berlin

### Nebentätigkeiten, Praktika

12/2001 - 03/2004	Wissenschaftliche Hilfskraft am Zentrum für Granulometrie (Labor für Partikelmesstechnik) der TU Dresden
07/2003 - 08/2003	Wissenschaftliche Hilfskraft am Fraunhofer-Institut für Zerstörungsfreie Prüfverfahren (IZFP) in Dresden
09/2002 - 01/2003	Praktikum in der industriellen Forschung im Laboratoire des Sciences du Genie Chimique (LSGC) in Nancy, Frankreich

## A.2 Publication

### Articles

**The Influence of Water on the Dispersion of Vanadia Supported on Silica SBA-15: A Combined XPS and Raman Study**

C. Hess, G. Tzolova-Müller, R. Herbert; *Journal of Physical Chemistry C*, 111 (2007), 9471-9479

**Identification of Silica-Supported Vanadia by X-ray Absorption Spectroscopy: Combined Theoretical and Experimental Studies**

M. Cavalleri, K. Hermann, A. Knop-Gericke, M. Hävecker, R. Herbert, C. Hess, A. Oesterreich, J. Döbler, R. Schlögl; submitted to *Journal of Catalysis*

**Stabilization of Mesoporous Silica SBA-15 by Surface Functionalization**

R. Herbert, R. Schlögl, C. Hess; *in preparation*

**The Structural Characterization of Vanadium Oxide Catalysts Supported on Nanoporous SiO<sub>2</sub> Using X-ray Absorption Spectroscopy**

A. Walter, R. Herbert, C. Hess, T. Ressler; *in preparation*

**Oxidative Dehydrogenation of Propane over SBA-15 Supported Vanadia Catalysts: A Kinetic Investigation**

A. Dinse, B. Frank, C. Hess, R. Herbert, S. Khenaache, R. Schomäcker; submitted to *Journal of Molecular Catalysis A: Chemical*

**Methodology for the Structural Characterization of VO<sub>x</sub> Species Supported on Silica under Reaction Conditions by Means of In Situ O K-edge X-ray Absorption Spectroscopy**

M. Hävecker<sup>1</sup>, M. Cavalleri, R. Herbert, R. Follath, A. Knop-Gericke, C. Hess, K. Hermann, R. Schlögl; *in preparation*

## Proceedings

### **Nanostrukturierte Vanadiumoxid-Modell-Katalysatoren auf Basis von mesoporösem SBA-15**

R. Herbert, U. Wild, C. Hess, R. Schlögl; Vortrag GVC/Dechema-Jahrestagungen 2006, *Chemie Ingenieur Technik*, 78 (2006), 1263

### **Eine neue Synthesemethode zur Stabilisierung der Nanostruktur mesoporöser Materialien am Beispiel eines geträgerten Vanadiumkatalysators**

R. Herbert, C. Hess, R. Schlögl; Poster ProcessNet-Jahrestagung 2007, *Chemie Ingenieur Technik*, 79 (2007), 1308-1309

## Posters

### **Nanostructured $V_xO_y$ Model Catalysts Supported on Mesoporous SBA-15**

R. Herbert, U. Wild, C. Hess, R. Schlögl; 39. Jahrestreffen Deutscher Katalytiker, March 15-17, 2006, Weimar (Germany)

### **Significant Increase of the Mechanical Stability of Nanostructured $V_xO_y$ -Model Catalysts Based on SBA-15**

R. Herbert, C. Hess, R. Schlögl; 40. Jahrestreffen Deutscher Katalytiker, March 14-16, 2007, Weimar (Germany)

### **A New Procedure to Stabilize Mesoporous Supported Vanadia Catalysts**

R. Herbert, C. Hess, R. Schlögl; *EuropaCat-VIII*, August 26-31, 2007, Turku (Finland)

### **Comparison of Nanostructured Vanadia Model Catalysts: Influence of Synthesis and Silica Support Materials**

R. Herbert, R. Schomäcker, R. Schlögl, C. Hess; 41. Jahrestreffen Deutscher Katalytiker, February 27-29, 2008, Weimar (Germany)

